

Multi-physics framework for fast modeling of gamma-ray burst afterglows

Vsevolod Nedora^{1,2}, Ludovica Crosato Menegazzi¹, Enrico Peretti³, Tim Dietrich^{1,2}, Masaru Shibata^{1,4}

¹Max Planck Institute for Gravitational Physics (Albert Einstein Institute), Am Mühlenberg 1, Potsdam 14476, Germany

²Institute for Physics and Astronomy, University of Potsdam, Potsdam 14476, Germany

³Université Paris Cité, CNRS, Astroparticule et Cosmologie, 10 Rue Alice Domon et Léonie Duquet, 75013 Paris, France

⁴Center for Gravitational Physics and Quantum Information, Yukawa Institute for Theoretical Physics, Kyoto University, Kyoto, 606-8502, Japan

Accepted XXX. Received YYY; in original form ZZZ

ABSTRACT

In this paper, we present `PyBlastAfterglow`, a modular C++ code with a Python interface to model light curves and sky maps of gamma-ray burst afterglows. The code is open-source, modular, and sufficiently fast to perform parameter grid studies. `PyBlastAfterglow` is designed to be easily extendable and used as a testing bed for new physics and methods related to gamma-ray burst afterglows. For the dynamical evolution of relativistic ejecta, a thin-shell approximation is adopted, where both forward and reverse shocks are included self-consistently, as well as lateral structure, lateral spreading, and radiation losses. Several models of the shock microphysics are implemented, including fully numerical model of the downstream electron distribution evolution, synchrotron emission, self-absorption, and synchrotron self-Compton emission under the one-zone approximation. Thus, the code is designed to be able to model complex afterglows that include emission from reverse shock, very high energy emission, structured jets, and off-axis observations.

Key words: neutron star mergers – stars: neutron – equation of state – gravitational waves

1 INTRODUCTION

A gamma-ray burst (GRB) is an intense, transient, cosmological source of electromagnetic radiation characterized by two distinct emission phases. The initial phase, known as prompt emission, typically lasts from a fraction of a second to several minutes. This prompt emission is highly variable; the spectrum usually peaks in keV - MeV range; peak isotropic luminosity typically lies in 10^{49-53} erg s⁻¹ range. This phase is followed by the afterglow during which the emission shows a broad spectrum ranging from gamma-rays to radio waves, and its temporal behavior that can be generally described by a smooth power-law (see Zhang (2018) for a textbook discussion).

GRBs are generally categorized into short and long types based on whether the prompt emission lasts less than or more than 2 seconds¹ and are thought to originate from ultra-relativistic jets. The fluid and energy dynamics within these jets are complex, involving both internal and external dissipation processes via mechanisms like matter shell interactions and magnetic reconnections (Thompson 1994; Rees & Meszaros 1994; Spruit et al. 2001; Rees & Meszaros 1992; Chevalier & Li 1999).

Various models have been proposed to explain the nature and mechanics of GRBs. For instance, long GRBs are often associated with jets forming during collapse of rapidly rotating massive stars whereas short GRBs are thought to be connected to mergers of compact objects at least one of which is a neutron star (Woosley 1993; Paczynski 1998; Abbott et al. 2017a). However, the composition and driving mechanisms within these jets – whether magnetic or kinetic

– are still areas of active research, particularly in how these mechanisms affect the efficiency and nature of prompt radiation (Preece et al. 1998; Lazzati & Ghisellini 1999; Ghisellini et al. 2000; Gianios & Spruit 2005; Fan & Piran 2006; Zhang & Yan 2011; Sironi et al. 2015b; Beniamini et al. 2016; Oganessian et al. 2017, 2018; Ravasio et al. 2018; Lazarian et al. 2019).

The afterglow emission is generally better understood. It encompasses all broad-band radiation from a GRB observed over long periods – from minutes to years – following the initial burst of prompt radiation. Generally it can be described by decaying power-laws (Nousek et al. 2006; Nardini et al. 2006; Zaninoni et al. 2013; Bernardini et al. 2012). This suggests that the afterglow radiation originates at larger radii – beyond 10^{15} cm – and is produced through interactions between the jet and the surrounding circumburst medium. This interaction drives two types of hydrodynamic shocks: a forward shock (FS) that moves into the surrounding medium and a reverse shock (RS) that travels back into the jet (Blandford & McKee 1976; Sari & Piran 1995). The system that includes these shocks and contact discontinuity between them is commonly referred to as a blast wave (BW).

Both FS and RS drive respective collisionless shocks, where interactions between particles are mediated via electromagnetic forces (Sironi et al. 2015a) instead of direct particle collisions. While the microphysics of these shocks is very complex, two main effects can be identified: amplification of random magnetic fields present in the shock upstream and acceleration of the inbound particles as those repeatedly cross the shock. The result of these processes is a non-thermal, synchrotron radiation produced by particles gyrating around magnetic field lines (Meszaros & Rees 1993, 1997; Sari & Piran 1999; Sari et al. 1998; Kobayashi & Sari 2000). Notably, many open questions remain regarding physics conditions at relativistic col-

¹ This categorization may suffer from the uncertainties in measuring burst duration (Moss et al. 2022)

lisionless shocks and GRBs offer a unique opportunity to study them (Vanthieghem et al. 2020; Sironi & Spitkovsky 2011; Sironi et al. 2013).

Most of the observed radiation was shown to come from particles accelerated at the FS. There, environmental conditions – where GRBs occur – and the nature of their progenitors affect electron and radiation spectra in addition to the details of shock microphysics. Notably, jet conditions at the start of the afterglow phase are defined not only by the overall energy budget of the burst but also by the dissipation processes that occurred during the prompt phase (Kumar & Zhang 2014).

While not being the main contributor to the observed emission, the RS was found to be important in interpreting observations of some GRBs (Laskar et al. 2019; Lamb et al. 2019a; Salafia et al. 2022). A RS forms when GRB ejecta collides with external medium. It travels back through the ejected matter, compressing, heating and decelerating it (Blandford & McKee 1976; Ayache et al. 2020). A RS is generally slower than a FS and moves through a significantly more dense medium. Thus, afterglow emission from it peaks at lower frequencies (radio-to-optical) and at early times – before the RS crosses the ejecta. The impact of the RS emission on the total afterglow emission is highly dependent on the initial jet Lorentz factor (LF), density of the circumburst medium, and jet structure and composition – whether it is baryonic or Poynting flux dominated (Zhang & Kobayashi 2005; McMahon et al. 2006; Giannios et al. 2008; Lyutikov 2011; Gao & Mészáros 2015). One prominent example of a RS contribution to afterglow is the GRB 180418A where a bright peak observed between 28 and 90 seconds after the burst in the optical band was attributed to it (Becerra et al. 2019).

Recently it was demonstrated that long GRBs can emit significant fraction of their energy in TeV range during the afterglow phase, (20–50% of the total emitted energy) (Acciari et al. 2019b; Abdalla et al. 2021; Cao et al. 2023). Specifically, in 2019 MAGIC and H.E.S.S. collaborations detected very high energy (VHE) emissions – above 100 GeV – from long GRBs 190114C during the afterglow phase (Abdalla et al. 2019; Acciari et al. 2019a). These observations confirmed the theoretically expected VHE long after the initial burst of gamma rays. The previous lack of such detections is believed to be at least in part attributed to technological limitations of earlier Cherenkov telescopes (Vurm & Beloborodov 2017; Gilmore et al. 2012; Domínguez et al. 2011; Franceschini & Rodighiero 2017). Current theoretical models suggest that VHE emission in the afterglow phase comes primarily from inverse Compton scattering, – a process in which lower energy photons are upscattered to gamma-ray energies through high energy electrons. While the details of the upscattering mechanism are still uncertain, recent observations hinted at synchrotron self-Compton (SSC) as a likely candidate. Notably, it was also noted that single-component synchrotron models might extend into the VHE spectrum under certain conditions (Pilla & Loeb 1998; Dermer et al. 2000; Wang et al. 2001, 2006; Fan et al. 2008a).

GRB170817A, observed in September 2017, is one of the best sampled and closest ($z = 0.0099$) GRBs ever detected (Arcavi et al. 2017; Coulter et al. 2017; Drout et al. 2017; Evans et al. 2017; Hallinan et al. 2017; Kasliwal et al. 2017; Nicholl et al. 2017; Smartt et al. 2017; Soares-Santos et al. 2017; Tanvir et al. 2017; Troja et al. 2017; Mooley et al. 2018b; Ruan et al. 2018; Lyman et al. 2018). It remains the only GRB associated with a burst of gravitational waves and quasi-thermal emission, called kilonova (Metzger et al. 2010; Savchenko et al. 2017; Alexander et al. 2017; Troja et al. 2017; Abbott et al. 2017b; Nynka et al. 2018; Hajela et al. 2019). The leading interpretation of this event is the merger of two neutron stars (Ab-

bott et al. 2017a). A detailed analysis of multi-frequency GRB afterglow data collected over several years suggested a non-trivial lateral structure within the jet (Fong et al. 2017; Troja et al. 2017; Margutti et al. 2018; Lamb & Kobayashi 2017; Lamb et al. 2018; Ryan et al. 2020; Alexander et al. 2018; Mooley et al. 2018b; Ghirlanda et al. 2019), created, at least in part, during jet propagation through dense kilonova ejecta (Lamb et al. 2022). Furthermore, radio and optical imaging of the burst region showed a motion of the image flux centroid (Mooley et al. 2022). It further confirmed the jetted nature of the GRB ejecta and provided additional constraints on jet properties (Mooley et al. 2018b, 2022).

Most observed GRB afterglows can be explained by radiation produced within relativistic shocks formed during ejecta propagation through the circumburst medium. However, there exist GRBs afterglow signatures that cannot be easily explained with this model. For instance, X-ray flares observed in approximately 33% of GRBs, exhibiting a broad range of timings and characteristics hinting towards an ongoing activity from the GRBs central engine (Chincarini et al. 2010; Margutti et al. 2011; Bernardini et al. 2011; Yi et al. 2016, 2017) or an unaccounted geometrical effects (Duque et al. 2022). Additionally, analysis of long GRBs often favor a constant density circumburst environment in contradiction to the expected wind profile, that should be produced by a massive star before it undergoes supernova explosion. Furthermore, degeneracies in model parameters further complicate inferring the conditions at burst and the nature of the progenitor, especially when observational data is limited (Panaitescu & Kumar 2003; Schulze et al. 2011; Li et al. 2015; Gompertz et al. 2018). Furthermore, model parameters associated with shock microphysics that are commonly used to relate the shock conditions to the emission properties in afterglow models have large discrepancies. Specifically, it was found that in order to explain some observations, certain parameter values tend to lay outside of ranges predicted by first-principle microphysics simulations (Kumar & Barniol Duran 2009, 2010; Barniol Duran & Kumar 2011; He et al. 2011).

Overall, extensive examinations of GRB afterglows provide insights into the progenitor and its environment, jet properties and the microphysics of collisionless shocks. It is also worth mentioning that GRBs are used extensively in cosmology (Dainotti et al. 2017; Schady 2017; Bulla et al. 2022). However, GRB jets are complex physical systems with spatial and temporal scales ranging from electron gyroradii to parsecs and from milliseconds to years respectively. Modeling these systems requires relativistic magnetohydrodynamics, plasma and collisionless shocks microphysics and radiation transport. Thus, it is practically impossible to construct a first-principle model of a GRB jet and all its observables. The state-of-the-art in this field is a numerical-relativistic magnetohydrodynamics (MHD) simulation combined with simplified treatment of shock microphysics and radiation transport (Daigne & Mochkovitch 2000; van Eerten et al. 2010; Ayache et al. 2020). These simulations are computationally very expensive and thus are ill-suited for parameter inference from observational data. Thus, in most cases, simplified analytic (Blandford & McKee 1976; Sari et al. 1998; Panaitescu & Kumar 2000; Granot & Sari 2002; Yamasaki & Piran 2022; Fraija et al. 2023) or semi-analytic (Huang et al. 1999; Uhm & Beloborodov 2006; Pe'er 2012; Nava et al. 2013; Zhang 2018; Ryan et al. 2020; Guarini et al. 2022; Miceli & Nava 2022; Wang et al. 2024) GRB afterglow models are employed.

The computational efficiency of this models allows them to be used in multimessenger studies, where a combined “hyper”-model that includes models of individual signatures is applied to diverse set of observational data that include GRB afterglow, su-

pernova/kilonova, gravitational waves and neutrinos (Dietrich et al. 2020; Pang et al. 2023; Kunert et al. 2024; Sarin et al. 2023). The main disadvantage of these models, however, is limited generalization due to limited and simplified physics input and non-trivial extendability that lead to methodological biases and inaccuracies.

In this work we present a GRB² afterglow model that attempts to achieve a balance between the computational efficiency and accuracy of physics input. The model is implemented in the open source numerical code `PyBlastAfterglow` designed to be (i) easily extendable and (ii) sufficiently fast to allow for construction of simulation grids that can in turn be used to train a surrogate model for direct Bayesian inference.

The paper is organized as follows. In Sec. 2, we introduce methods used to model GRB afterglow, starting with BW dynamics (Sec. 2.1), then discussing shock microphysics and comoving radiation (Sec. 2.2) and subsequently showing how the observed radiation is obtained (Sec. 2.4). In Sec. 2, we elaborate on the details of numerical implementation of the aforementioned physics. Then, in Sec. 3, we discuss in detail two GRB afterglow simulations for a unstructured (top-hat) jet and a structured (Gaussian) jet. To validate the code we perform extensive comparisons with existing codes and published resurgings in Sec. 4. After that, in Sec. 5, we illustrate code application to VHE afterglow of GRB 190411C and complex afterglow signatures of GRB 170817A. Finally, in Sec. 6, we summarize the presented work and provide an outlook.

2 METHODS

In this section we discuss the physics that is implemented in `PyBlastAfterglow`. For the sake of completeness and future referencing we discuss some derivation in detail.

2.1 Blastwave dynamics

The interaction between an ejecta shell and an ambient medium can be considered as a relativistic Riemann problem, in which shocks form when required conditions for velocities densities and pressures are met (cf. Rezzolla & Zanotti (2013) for a textbook discussion).

There are several semi-analytic formulations of BW dynamics with a FS and a RS in the literature. They can be broadly divided into pressure balance formulations and mechanical models. Pressure balance formulations assume that the pressure in FS and RS downstreams are equal (Nava et al. 2013; Chen & Liu 2021; Zhang et al. 2022). The mechanical model was proposed by (Beloborodov & Uhm 2006; Uhm & Beloborodov 2006) and later improved by (Ai & Zhang 2021; Ai et al. 2022). It does not rely on the pressure equilibrium and has a better energy conserving property. In `PyBlastAfterglow` we implement the formulation motivated by (Nava et al. 2013) (hereafter N13; see their appendix B).

2.1.1 Evolution equations

Consider the stress-energy tensor for perfect fluid,

$$T^{\mu\nu} = (\rho'c^2 + e' + p')u^\mu u^\nu + p'\eta^{\mu\nu}, \quad (1)$$

where $u^\mu = \Gamma(1, \beta)$ is the fluid four-velocity with Γ being the bulk Lorentz factor (LF) and $\beta = \sqrt{1 - \Gamma^{-2}}$ is the dimensionless velocity (in units of the speed of light, c), $p' = (\hat{\gamma} - 1)e'$ is the pressure, e' is the internal energy density, $\hat{\gamma}$ is the adiabatic index (also called the ratio of specific heats), and $\eta^{\mu\nu}$ is the metric with signature $\{-1, 1, 1, 1\}$. Hereafter, we define prime quantities in the comoving frame.

If the fluid is ultra-relativistic, $\hat{\gamma} = 4/3$, and if it is non-relativistic, $\hat{\gamma} = 5/3$. These limits can be recovered by assuming the following form of the $\hat{\gamma}$ dependency on the fluid LF (e.g. Kumar & Granot 2003)

$$\hat{\gamma} \approx \frac{4 + \Gamma^{-1}}{3}. \quad (2)$$

A more accurate prescription can be inferred from numerical simulations (Mignone et al. 2005).

The $\mu = \nu = 0$ component of the stress-energy tensor Eq. (1), then reads

$$T^{00} = \Gamma^2(\rho'c^2 + e' + p') - p' = \Gamma^2\rho'c^2 + (\hat{\gamma}\Gamma^2 - \hat{\gamma} + 1)e'. \quad (3)$$

Under the thin-shell approximation (e.g., assuming that an ejecta shell is uniform in its properties) the total energy of the shell reads,

$$E_{\text{tot}} = \int T^{00} dV = \Gamma c^2 \rho' V' + \Gamma_{\text{eff}} e' V' = \Gamma c^2 m + \Gamma_{\text{eff}} E'_{\text{int}}, \quad (4)$$

where $\Gamma_{\text{eff}} = (\hat{\gamma}\Gamma^2 - \hat{\gamma} + 1)/\Gamma$ is the effective LF (e.g., see Nava et al. (2013); Zhang (2018); Guarini et al. (2022)), the enclosed mass $m = \rho'V'$ with V' is the comoving volume, and the co-moving internal energy is $E'_{\text{int}} = e'V'$.

As mentioned before, a BW is comprised of FS, RS, and a contact discontinuity between them. Following standard notation, we label the unshocked ejecta (interstellar medium (ISM)) as regions 4 (1) and shocked ejecta (ISM) as regions 3 (2) (see figure B1 in N13). The region to which a quantity belongs to will be indicated with the subscript.

The total energy of the BW with FS propagating into the circumburst medium, contact discontinuity and the RS propagating into the ejecta itself reads (N13),

$$E_{\text{tot}} = \Gamma_0 m_{0;4} c^2 + \Gamma m_{0;3} c^2 + \Gamma_{\text{eff};3} E'_{\text{int};3} + \Gamma_0 m_{0;2} c^2 + \Gamma_{\text{eff};2} E'_{\text{int};2}. \quad (5)$$

Notably, most semi-analytic afterglow models in the literature only consider the FS. This is equivalent to assuming that at the beginning of a simulation, the RS has already crossed ejecta and that the entire ejecta shell moves with the bulk LF Γ . Without this assumption, an ejecta shell is initially not shocked and moves with the LF Γ_0 as the first two terms in Eq. (5) indicate.

As the BW moves through the circumburst medium, it accretes mass, dm , and loses energy due to radiation from both shocked regions, $dE'_{\text{rad};3}$, and, $dE'_{\text{rad};2}$, so that the total change in BW energy is given as,

$$dE_{\text{tot}} = \Gamma dm c^2 + \Gamma_{\text{eff};2} dE'_{\text{rad};2} + \Gamma_{\text{eff};3} dE'_{\text{rad};3}, \quad (6)$$

where $\Gamma_{\text{eff};3} = (\hat{\gamma}_3 \Gamma^2 - \hat{\gamma}_3 + 1)/\Gamma$, $\hat{\gamma}_3$ is given by the equation of state (EOS), Eq. (2), using the relative LF between upstream and downstream, Γ_{43} . Combining the equations and re-arranging the terms, we obtain,

$$dE_{\text{tot}} = (\Gamma_0 dm_{0;4} + d\Gamma m_{0;3} + \Gamma dm_{0;3} + d\Gamma dm + \Gamma dm - dm)c^2 + d\Gamma_{\text{eff};3} E'_{\text{int};3} + \Gamma_{\text{eff};3} (dE'_{\text{int};3} - dE'_{\text{rad};3}) + d\Gamma_{\text{eff};2} E'_{\text{int};2} + \Gamma_{\text{eff};2} (dE'_{\text{int};2} - dE'_{\text{rad};2}) \quad (7)$$

² Source code: <https://github.com/vsevolodnedora/PyBlastAfterglowMag>

Here $dm_{0;3}$ is the amount of mass that crosses the RS over the time period that the FS takes to attain mass dm . The change in mass in the unshocked part of the shell then is $dm_{0;4} = -dm_{0;3}$.

The change in the internal energy behind the FS reads,

$$dE'_{\text{int};2} = dE'_{\text{sh};2} + dE'_{\text{ad};2} + dE'_{\text{rad};2}, \quad (8)$$

where dE'_{sh} is the random kinetic energy produced at the shock due to inelastic collisions (Blandford & McKee 1976) with element dm accreted from circumburst medium, dE'_{ad} is the energy lost to adiabatic expansion, and dE'_{rad} is the energy lost to radiation. The latter we discuss separately in Sec. 2.3.

We further assume that for the FS the upstream medium can be viewed as cold and static. Then in the post-shock frame the average kinetic energy per unit mass is $(\Gamma - 1)c^2$ and is constant across the shock. Thus,

$$dE'_{\text{sh};2} = (\Gamma - 1)c^2 dm. \quad (9)$$

Adiabatic losses, $dE'_{\text{ad};2}$, can be obtain in two main formulations: microscopic and macroscopic. The former relies on integrating the momenta of hadrons and leptons (Dermer & Humi 2001; Miceli & Nava 2022) (see equation B(15) in N13). The latter formulation can be easily derived from the first law of thermodynamics, $dE'_{\text{int};2} = T'dS' - p'_2 dV'_2$, for an adiabatic process, *i.e.*, $T'dS' = 0$. Then,

$$dE'_{\text{ad};2} = -(\hat{\gamma}_2 - 1)E'_{\text{int};2} d \ln V'_2. \quad (10)$$

where we used $p'_2 = (\hat{\gamma} - 1)E'_{\text{int};2}/V'_2$. For a static and cold upstream, the comoving volume is $V' \propto R^3/\Gamma$, so that the derivative $d \ln V'_2$ reads

$$d \ln V'_2 = d \ln m - d \ln \rho - d \ln \Gamma. \quad (11)$$

For the RS the energy change in the downstream reads,

$$dE'_{\text{int};3} = dE'_{\text{sh};3} + dE'_{\text{ad};3} + dE'_{\text{rad};3}. \quad (12)$$

Notably, the upstream with respect to the RS is not static, so that the average kinetic energy per unit mass in the post-shock frame equals to $(\Gamma_{\text{rel}} - 1)c^2$, where $\Gamma_{\text{rel}} = \Gamma_{43}$ is the relative LF between upstream and downstream. Then, the energy generated at the shock is,

$$dE'_{\text{sh};3} = (\Gamma_{43} - 1)c^2 dm_{0;3}, \quad (13)$$

and the adiabatic losses $dE'_{\text{ad};3}$ in macroscopic formulation reads,

$$dE'_{\text{ad};3} = -(\hat{\gamma}_3 - 1)E'_{\text{int};3} d \ln V'_3. \quad (14)$$

As $V' \propto R^3/\Gamma_{43}$, its derivative reads,

$$d \ln V'_3 = d \ln m_{0;3} - d \ln \rho_4 - d \ln \Gamma_{43}, \quad (15)$$

where $d \ln \Gamma_{43} = \Gamma_{43}^{-1} (d\Gamma_{43}/d\Gamma) d\Gamma$.

In Eq. (7), the expression for internal energy for both shocks, $dE'_{\text{int};i} - dE'_{\text{rad};i}$ can be replaced with $dE'_{\text{sh};i} - dE'_{\text{ad};i}$, where $i \in \{2, 3\}$. After doing this and rearranging the terms we arrive at the evolution equation for the BW bulk LF

$$\begin{aligned} d\Gamma &= -\frac{N}{D}, \text{ where} \\ N &= (\Gamma - 1)(\Gamma_{\text{eff};2} + 1)dm \\ &\quad + (\Gamma - \Gamma_0 + \Gamma_{\text{eff};3}(\Gamma_{43} - 1))dm_{0;3} \\ &\quad + \Gamma_{\text{eff};2}(\hat{\gamma}_2 - 1)E'_{\text{int};2}(d \ln m - d \ln \rho) \\ &\quad - \Gamma_{\text{eff};3}(\hat{\gamma}_3 - 1)E'_{\text{int};3}(d \ln m_{0;3} - d \ln \rho_4) \\ D &= (m + m_{0;3}) + E'_{\text{int};2} \frac{d\Gamma_{\text{eff};2}}{d\Gamma} + E'_{\text{int};3} \frac{d\Gamma_{\text{eff};3}}{d\Gamma} \\ &\quad + \frac{\Gamma_{\text{eff};2}}{\Gamma}(\hat{\gamma}_2 - 1)E'_{\text{int};2} + \frac{\Gamma_{\text{eff};3}}{\Gamma_{43}}(\hat{\gamma}_3 - 1)E'_{\text{int};3} \frac{d\Gamma_{43}}{d\Gamma}. \end{aligned} \quad (16)$$

The advantage of choosing the analytical expression for EOS, Eq. (2), is that we can compute the derivatives in Eq. (16) analytically as,

$$\frac{d\Gamma_{\text{eff};2}}{d\Gamma} = \frac{4}{3} + \frac{1}{3\Gamma^2} + \frac{2}{3\Gamma^3} \quad (17)$$

and

$$\begin{aligned} \frac{d\Gamma_{\text{eff};3}}{d\Gamma} &= \frac{d}{d\Gamma} \left[(\hat{\gamma}_3(\Gamma^2 - 1) + 1) \frac{1}{\Gamma} \right] \\ &= \hat{\gamma}_3 \left(1 + \frac{1}{\Gamma^2} \right) + \frac{d\hat{\gamma}_3}{d\Gamma_{43}} \frac{d\Gamma_{43}}{d\Gamma} \Gamma \left(1 - \frac{1}{\Gamma} \right) - \frac{1}{\Gamma^2} \\ &= \hat{\gamma}_3 \left(1 + \frac{1}{\Gamma^2} \right) - \frac{1}{3} \frac{d\Gamma_{43}}{d\Gamma} \frac{1}{\Gamma_{43}^2} \Gamma \left(1 - \frac{1}{\Gamma^2} \right) - \frac{1}{\Gamma^2}. \end{aligned} \quad (18)$$

For numerical reasons it is convenient to express Γ_{43} as

$$\begin{aligned} \Gamma_{43} &= \Gamma\Gamma_0(1 - \beta\beta_0) = \Gamma\Gamma_0 \frac{1 + \beta\beta_0}{1 + \beta\beta_0} (1 - \beta\beta_0) \\ &= \Gamma\Gamma_0 \left(\frac{1}{\Gamma_0^2} + \frac{1}{\Gamma^2} - \frac{1}{\Gamma^2\Gamma_0^2} \right) \frac{1}{(1 + \beta\beta_0)}, \end{aligned} \quad (19)$$

and its derivative, present in Eq. (16) and Eq. (18), as

$$\frac{d\Gamma_{43}}{d\Gamma} = \Gamma_0 + \frac{\Gamma(1 - \Gamma_0^2)}{\sqrt{\Gamma^2\Gamma_0^2 - \Gamma_0^2 - \Gamma^2 + 1}}. \quad (20)$$

As the RS propagates through the ejecta shell, it accretes matter at a rate given by $dm_{0;3}$. Following N13 we write,

$$dm_{0;3} = 2\pi R_{\text{rsh}}^2 (1 - \cos(\omega)) (\beta_{34} + \beta_3) \rho'_4 c dt', \quad (21)$$

where ω is the half-opening angle of the BW, R_{rsh} is the radius of the RS, β_{34} is the dimensionless velocity of the unshocked ejecta relative to the BW, β_3 is the shocked ejecta velocity in its own frame and ρ'_4 is the mass density of the unshocked ejecta measured in the frame of the shocked ejecta. The latter can be related to the ejecta density in the progenitor frame as follows,

$$\rho'_4 = \Gamma_{43} \rho''_4 = \frac{\Gamma_{43}}{\Gamma} \rho_4 = \Gamma(1 - \beta\beta_0) \rho_4, \quad (22)$$

where in the last step we used that $\Gamma_{43} = \Gamma\Gamma_0(1 - \beta\beta_0)$. In Eq. (22), ρ''_4 is the ejecta density measured in its own frame, *i.e.*, the proper density. The quantity β_3 in Eq. (21) can be obtained from shock jump conditions (assuming strong shock and assuming that upstream is cold, *i.e.*, that the energy density is $e_4 = \rho''_4 c^2$ and pressure $p_4 = 0$) as follows,

$$\beta_3 = \frac{\beta_{34}}{3} = \frac{\beta_0 - \beta}{3(1 - \beta\beta_0)}. \quad (23)$$

The distance that a shock travels over the comoving time dt' can be obtained from the shock velocity in the progenitor frame as follows $dR = \beta_{\text{sh}}/(\Gamma(1 - \beta\beta_{\text{sh}}))$. In the case of RS, the $\beta_{\text{sh}} = \beta_3$ and after some algebra we can write $dt' = 3/(4\beta\Gamma c) dR$. Substituting this into Eq. (21), together with Eq. (22), we obtain

$$\frac{dm_{0;3}}{dR} = 2\pi R_{\text{rsh}}^2 (1 - \cos(\omega)) \rho_4 \frac{d\Delta'_4}{dR}, \quad (24)$$

where we introduced the rate of change of the thickness of shocked region behind the RS, $d\Delta'_4$, that reads,

$$\begin{aligned} \frac{d\Delta'_4}{dR} &= \frac{d}{dR} (t_{\text{burst}} \beta_0 c - R_{\text{sh}}) = \frac{\beta_0 - \beta}{\beta} \\ &= \beta_0 \frac{\beta^{-4} - \beta_0^{-4}}{(\beta^{-1} + \beta_0^{-1})(\beta^{-2} + \beta_0^{-2})}, \end{aligned} \quad (25)$$

where in the last stage we expanded it for numerical reasons. Since

we are working within the thin-shell approximation to BW radial structure, we can write $R \sim R_{\text{rsh}} \sim R_{\text{shell}}$.

The initial width of the ejecta shell in the progenitor frame can be taken as $\Delta_0 = ct_{\text{prompt}}\beta_0$, where t_{prompt} is the duration of the mass ejection in the progenitor frame. In our model t_{prompt} is a free parameter. Additionally, we assume that the ejecta density in the observer frame, ρ_4 , scales with its initial value at follows

$$\rho_4 = \frac{M_0}{2\pi(1 - \cos(\omega))R_{\text{rsh}}\Delta_0} \exp\left(-\frac{\Delta_4}{\Delta_0}\right). \quad (26)$$

Its derivative, needed for Eq. (16), reads

$$\frac{d \ln \rho_4}{dR} = -\frac{2}{R} - \frac{1}{\Delta_0} \frac{d\Delta_4}{dR}. \quad (27)$$

Substituting Eq. (26) into Eq. (24), we obtain the equation for the mass accreted by the RS,

$$\frac{dm_{0;3}}{dR} = \frac{M_0}{\Delta_0} \frac{d\Delta_4}{dR} \exp\left(-\frac{\Delta_4}{\Delta_0}\right). \quad (28)$$

It is commonly assumed that at the beginning of the simulation, the RS has already crossed the ejecta. In this can we can rewrite Eq. (16) as following,

$$d\Gamma = \frac{-(1 + \Gamma_{\text{eff};2})(\Gamma - 1) + \Gamma_{\text{eff};2}(\hat{\gamma}_2 - 1)E'_{\text{int};2} \frac{dm}{m}}{(M_0 + m)c^2 + \frac{d\Gamma_{\text{eff};2}}{d\Gamma} E'_{\text{int};2} + \Gamma_{\text{eff};2}(\hat{\gamma}_2 - 1)E'_{\text{int};2} \frac{1}{\Gamma}}. \quad (29)$$

Eq. (29) corresponds to the Eq. 7 in N13 after inserting the adiabatic term term given by Eq. (10).

2.1.2 Lateral spreading

When a GRB jet decelerates and different regions become casually connected with each other, the transverse pressure gradient will lead to motion along the tangent to the surface. Consequently, the jet starts to spread laterally (e.g. van Eerten et al. 2010; Granot & Piran 2012; Duffell et al. 2018).

In most semi-analytic GRB afterglow models that include the jet lateral structure and employ the thin-shell approximation of the BW, lateral spreading cannot be incorporated in a self-consistent way. Recently, however, new models were proposed where GRB ejecta is modeled as a 2D thin-shell including a pressure gradient along its surface. In such models lateral spreading occurs naturally (Lu et al. 2020; Wang et al. 2024).

In a model that approximates ejecta as a set of independent BWs, each of which is evolved under thin-shell approximation, the exact form of the lateral expansion prescription – functional form of BW opening angle evolution – is one of the main free parameters. We consider the following prescription motivated by Huang et al. (2000b) and Ryan et al. (2020). We assume that an expanding fluid element interacts only with matter in its immediate vicinity. There, the lateral and radial components of the velocity are related as $\beta_r/\beta_\omega = \partial\omega/\partial \ln R$ (Huang et al. 2000a). The co-moving sound speed in the shocked region reads $c_s^2 = dp'/de'|_{\text{shock}}$ (Kirk & Duffy 1999) that can be written as,

$$c_s^2 = \frac{\hat{\gamma}p'}{\rho'} \left[\frac{(\hat{\gamma} - 1)\rho'}{(\hat{\gamma} - 1)\rho' + \hat{\gamma}\rho'} \right] c^2 = \frac{\hat{\gamma}(\hat{\gamma} - 1)(\Gamma - 1)}{1 + \hat{\gamma}(\Gamma - 1)} c^2, \quad (30)$$

where we inserted $\hat{\gamma}$ using Eq. (2). Then, assuming that the spreading proceeds at the sound speed, $v_\omega = c_s$, the lateral expansion can be written as (Huang et al. 2000b)

$$\frac{d\omega}{dR} = \frac{c_s}{R\Gamma_{\text{sh}}\beta_{\text{sh}}c}. \quad (31)$$

This formulation has been used in the early semi-analytic GRB afterglow models (e.g. Rossi et al. 2004).

For a structured jet, however, the so-called ‘‘conical’’ spreading model was shown to yield a better agreement with numerical simulations (Ryan et al. 2020). There, all the material that has been swept up in the past affects spreading at a given time. However, in deriving their prescription, Ryan et al. (2020) implicitly assumed the ‘‘TM’’ EOS (Mignone et al. 2005) for transrelativistic fluid. In order to remain consistent with the rest of our model, we, instead, continue to use Eq. (30), while adopting structure-related terms from the aforementioned study to obtain the final form of the prescription as follows,

$$\frac{d\omega}{dR} = \frac{c_s}{R\Gamma_{\text{sh}}\beta_{\text{sh}}c} \times \begin{cases} 0 & \text{if } Q_0\Gamma_{\text{sh}}\beta_{\text{sh}}\omega_c < 1 \\ \frac{Q(1 - Q_0\omega_c\Gamma_{\text{sh}}\beta_{\text{sh}})}{Q - Q_0} & \text{if } Q\Gamma_{\text{sh}}\beta_{\text{sh}}\omega_c > 1 \\ 1 & \text{otherwise} \end{cases}, \quad (32)$$

$$\times \begin{cases} \tan(\omega_0/2)/\tan(\omega_c/2) & \text{if } \omega_0 < \omega_c \\ 1 & \text{otherwise} \end{cases},$$

where $Q = 3\sqrt{2}$, $Q_0 = 2$, ω_0 is the initial half-opening angle of the BW, and ω_c is the half-opening angle of the jet core, given as a free parameter when setting the Gaussian jet structure.

Numerical simulations of jet spreading show that only when a jet has decelerated, the spreading can commence (Xie et al. 2018; van Eerten et al. 2010; Granot & Piran 2012; Duffell et al. 2018). Authors of the aforementioned prescriptions account for this by setting $d\omega/dt = 0$ if $Q_0\Gamma_{\text{sh}}\beta_{\text{sh}}\omega_c \geq 1$ (see first case braces in Eq. (32)).

As the BW laterally spreads, the amount of mass it sweeps increases. Following Granot & Piran (2012), we write the equation for the mass accreted by the BW as follows,

$$dm = 2\pi\rho \left[(1 - \cos(\omega)) + \frac{1}{3} \sin(\omega)Rd\omega \right] R^2. \quad (33)$$

In the comoving frame, the shock downstream densities read

$$\begin{aligned} \rho'_2 &= (\hat{\gamma}_2\Gamma + 1)/(\hat{\gamma}_2 - 1)\rho_{\text{ISM}}, \\ \rho'_3 &= (\hat{\gamma}_3\Gamma + 1)/(\hat{\gamma}_3 - 1)\rho_4, \end{aligned} \quad (34)$$

for the FS and RS respectively.

While we employ the thin-shell approximation to the BW structure, we also need actual thicknesses of shocked regions in order to compute radiation transport. Under the general assumption of a homogeneous shell, but relaxing the assumption of the uniform upstream medium, the shocked region thicknesses in the burster frame read (Johannesson et al. 2006),

$$\begin{aligned} \Delta R_{\text{fsh}} &= \frac{m_2}{2\pi R^2(1 - \cos(\omega))\Gamma\rho'_2}, \\ \Delta R_{\text{rsh}} &= \frac{m_3}{2\pi R^2(1 - \cos(\omega))\Gamma\rho'_3}. \end{aligned} \quad (35)$$

It is worth noting that for the FS, if $1 - \cos(\omega) = 2$ and the swept-up mass $m_2 = 4\pi R^3 n' m_p/3$, we obtain the commonly used Blandford & McKee (BM) shock thickness, $\Delta R' = R/12\Gamma^2$ (e.g. Johannesson et al. 2006; van Eerten et al. 2010).

2.2 Microphysics & Comoving Radiation

As a BW moves through the medium with small but present magnetization, the seed magnetic field becomes amplified through a range of instabilities such as the current-driven instability (Reville et al. 2006), the Kelvin-Helmholtz shear instability (Zhang & Yan 2011),

the Weibel (filamentation) instability (Medvedev & Loeb 1999; Lemoine & Pelletier 2010; Tomita & Ohira 2016), the Čerenkov resonant instability (Lemoine & Pelletier 2010), the Rayleigh-Taylor instability (Duffell & MacFadyen 2013), the magneto-rotational instability (Cerdá-Durán et al. 2011), or the pile-up effect (Rocha da Silva et al. 2015).

Inbound charged particles gain energy, reflecting off and scattering on MHD instabilities, and acquire a spectrum, a certain distribution in energy. In order to model this process, particle-in-cell (PIC) simulations are commonly employed to study particle dynamics at electron's gyro-radius scale (e.g. Sironi et al. 2015a). However, even sophisticated MHD-PIC simulations used to model larger spatiotemporal scales are still limited to a few 10^3 of proton gyro-scales and few milliseconds (Bai et al. 2015; Mignone et al. 2018). These first-principles studies showed that the main process responsible for electron acceleration at collisionless shocks is the first-order Fermi acceleration (Spitkovsky 2008; Sironi & Spitkovsky 2009, 2011; Park et al. 2015).

As mentioned in the introduction, the shock microphysics is practically impossible to model on spatial and temporal scales relevant for GRB afterglows. It is thus common to make simplifying assumptions regarding shock microphysics and employ approximate models or prescriptions. These can be generally divided into two groups, depending on whether the electron (and photon) distributions are evolved self-consistently or assumed to be fixed and given. The example of the latter is a very common model proposed by Sari et al. (1998) and further extended by Granot & Sari (2002). The underlying assumption of this model is that the instantaneous electron spectrum can always be approximated with a broken power law (BPL) separated by critical electron LF. Then, the synchrotron spectrum, computed as an integral over the electron distribution, is also a BPL. Moreover, it is possible to include synchrotron self-absorption (SSA) and high-energy SSC spectrum analytically as well (Nakar et al. 2009; Joshi & Razzaque 2021; Yamasaki & Piran 2022; Pellouin & Daigne 2024). However, by construction, these formulations, while allowing for very computationally efficient afterglow models (e.g., `afterglowpy` and `jetsimpy`), are not flexible or generalizable.

Another approach to modeling microphysics is to evolve electron distribution explicitly accounting for heating and cooling and obtain instantaneous emission spectra numerically by convolving emission kernels with current electron distribution (Dermer & Humi 2001; Petropoulou & Mastichiadis 2009; Miceli & Nava 2022; Huang 2022; Zhang et al. 2023). In these models, only the injection electron spectrum – the electron distribution that emerges after the acceleration processes at collisionless shock – is usually fixed, while the electron distribution in the shock downstream is allowed to evolve. This approach is also quite common in modeling quasi-stationary systems, such as active galactic nuclei jets (Kino et al. 2002; Jamil, O. and Böttcher, M. 2012) and it allows for larger flexibility, e.g., employing more physically-motivated injection spectra (Warren et al. 2022; Gao et al. 2023), different heating (Warren et al. 2015) and cooling processes and non-trivial interactions between photons and electrons (Wang & Mészáros 2006; He et al. 2009).

Notably, in both approaches, the microphysics of particle acceleration and magnetic field amplification is hidden behind free parameters. Specifically, it is common to assume that a certain fraction of downstream shock energy goes into particle acceleration, ϵ_e , and magnetic field amplification, ϵ_b . Together with the slope of the injection electron spectrum (assuming it is a single power-law) p , they form a set of free parameters that most afterglow models consider.

Since shock microphysics is the same for FS and RS and depends

on the properties of these shocks' downstream, we omit here subscripts 2 and 3 that were used in the previous section for clarity. For the same reason we omit apostrophe, $'$, for the electron LFs since we only work with the comoving electron spectrum here.

Recall that comoving energy density in shock downstream reads $e' = E'_{\text{int}}/V'$ where the comoving volume $V' = m/\rho'$, m is the shocked region mass and ρ' is the comoving mass density. Then, the magnetic field strength in the shock downstream reads

$$B' = \sqrt{8\pi\epsilon_b e'} \quad (36)$$

Notably, e' can also be evaluated directly as $e' = 4\Gamma(\Gamma - 1)n_{\text{ISM}}m_p c^2$ in the relativistic regime. Then, the magnetic field strength can simply be expressed as $B' = \sqrt{32\pi\epsilon_b m_p c^2 n_{\text{ISM}}(\Gamma - 1)\Gamma}$.

Consider a power-law electron spectrum in injected electrons, $dN_e/d\gamma_e \propto \gamma_e^{-p}$ for $\gamma_e \in (\gamma_{e;\text{m}}, \gamma_{e;\text{M}})$, where γ_e is the electron LF, p is the spectral index and $\gamma_{e;\text{m}}$ and $\gamma_{e;\text{M}}$ are minimum and maximum LFs (Dermer & Chiang 1998; Sari et al. 1998).

The maximum LF can be obtained by balancing the acceleration timescales with the minimum cooling timescale for an electron. For electrons, the dynamical timescale, $t'_{\text{dyn}} \simeq R/c\Gamma$, would generally be significantly larger than the radiation cooling timescale that reads,

$$t'_{\text{cool}} = \frac{6\pi m_e c}{\gamma_e \sigma_T B'^2 (1 + \tilde{Y})}, \quad (37)$$

where \tilde{Y} stands for the corrections due to inverse Compton (IC) scattering. Thus, for an electron with $\gamma_e = 10^3$ in magnetic field $B' = 100$ G, $t'_{\text{cool}} \simeq 77$ sec., assuming $\tilde{Y} = 1$.

From Eq. (37) it is possible to derive the characteristic cooling LF above which injected electrons rapidly cool,

$$\gamma_{e;c} = \frac{6\pi m_e c}{\sigma_T t' B'^2 (1 + \tilde{Y})}. \quad (38)$$

Equation (38) is written in the comoving frame. Commonly, in the literature $\gamma_{e;c}$ is evaluated in the observer frame, then, an additional factor $1/\Gamma$ is added.

The comoving acceleration time for an electron can be written as,

$$t'_{\text{acc}} \simeq \zeta \frac{r_B}{c} = \zeta \frac{\gamma_e m_e c}{q_e B'}, \quad (39)$$

where $r_B = \gamma_e m_e c^2 / (q_e B')$ is the guration radius and $\zeta \simeq 1$ is a free parameter that depends on the acceleration mechanism. Equating Eq. (37) and Eq. (39), we obtain,

$$\gamma_{e;\text{M}} = \sqrt{\frac{6\pi q_e}{\sigma_T B' \zeta (1 + \tilde{Y})}}. \quad (40)$$

It is important to note that $\gamma_{e;\text{M}}$ may depend on the non-uniformity in the shock downstream magnetic field. If B' is not constant, but decays with distance from the shock front, electrons will lose most of their energy further downstream, where the Larmor radius, r_B , is larger (Kumar et al. 2012). To account for this, the weakest magnetic field, B'_w , should be used in Eq. (40) instead of B' (Miceli & Nava 2022).

The lower limit of the electron injection spectrum $\gamma_{e;\text{m}}$, can be obtained from the following considerations. Within an assumed power-law distribution, $N_e \propto \gamma_e^{-p}$, the average electron LF reads,

$$\langle \gamma_e \rangle = \frac{\int_{\gamma_{e;\text{m}}}^{\gamma_{e;\text{M}}} \gamma_e N_e d\gamma_e}{\int_{\gamma_{e;\text{m}}}^{\gamma_{e;\text{M}}} N_e d\gamma_e} = \frac{\int_{\gamma_{e;\text{m}}}^{\gamma_{e;\text{M}}} \gamma_e^{-p+1} d\gamma_e}{\int_{\gamma_{e;\text{m}}}^{\gamma_{e;\text{M}}} \gamma_e^{-p} d\gamma_e}. \quad (41)$$

This integral can be solved analytically. If $p \neq 1$ and $p \neq 2$, we can write,

$$\langle \gamma_e \rangle = \left(\frac{p-1}{p-2} \right) \left(\frac{\gamma_{e;M}^{-p+2} - \gamma_{e;m}^{-p+2}}{\gamma_{e;M}^{-p+1} - \gamma_{e;m}^{-p+1}} \right). \quad (42)$$

Otherwise, the solution is (Zhang 2018),

$$\langle \gamma_e \rangle = \begin{cases} \frac{\ln(\gamma_{e;M}) - \ln(\gamma_{e;m})}{-\gamma_{e;M} + \gamma_{e;m}} & \text{if } p = 2, \\ \frac{\gamma_{e;M} - \gamma_{e;m}}{\ln(\gamma_{e;M}) - \ln(\gamma_{e;m})} & \text{if } p = 1. \end{cases} \quad (43)$$

On the other hand, under the assumption that only a fraction of shock downstream energy is used in electron acceleration, we can write the following expression for the average electron LF,

$$\langle \gamma_e \rangle = \epsilon_e \frac{e'}{\rho'} \frac{m_p}{m_e c^2}, \quad (44)$$

where m_e and m_p are the electron and proton mass, respectively.

Notably, in the presence of electron-positron pairs, the ratio of proton to electron densities has to be included in aforementioned equations (Beloborodov 2005; Nava et al. 2013). Here we implicitly assume that the shock downstream is not pair-rich.

Eq. (42) and Eq. (44) can be solved analytically for $\gamma_{e;m}$ assuming that $p > 2$ and $\gamma_{e;M} \gg \gamma_{e;m}$, to obtain $\gamma_{e;m} = ((p-2)/(p-1))e'm_p/(\rho'm_e c^2)$. These limits are usually respected in the context of GRB afterglows, (e.g. Kumar & Zhang 2014). Also, the theory of particle acceleration at relativistic shocks predicts $p \gtrsim 2$ (Sironi et al. 2015a; Marcowith et al. 2020).

In Eq. (44) we chose not to include explicitly a quantity that represents a fraction of the shocked electrons that participate in the acceleration process. This parameter, usually denoted as ξ_e in GRB afterglow literature, is degenerated with ϵ_e (Eichler & Waxman 2005). As such, we implicitly assume that $\xi_e = 1$, i.e., all inbound electrons are accelerated, and only ϵ_e regulates with what efficiency.

As a shock decelerates and $\gamma_{e;m} \rightarrow 1$, electron acceleration enters the so-called deep-Newtonian regime (Sironi & Giannios 2013), that starts when $\beta_{sh} \lesssim 8\sqrt{m_p/m_e \bar{\epsilon}_e}$, where $\bar{\epsilon}_e = 4\epsilon_e(p-2)/(p-1)$ (Margalit & Piran 2020). Notably, synchrotron emission from electrons accelerated at lower shock velocity is dominated by electrons with LF $\simeq 2$, instead of those with $\gamma_{e;m}$. Thus, when $\gamma_{e;m}$ gets close to 1, additional adjustments to our model are needed. Specifically, we set that only a fraction of injected electrons, ξ_{DN} , can contribute to the observed emission. The ξ_{DN} is computed according as follows (Sironi & Giannios 2013),

$$\xi_{DN} = \frac{p-2}{p-1} \epsilon_e \frac{e'}{\rho'} \frac{m_p}{m_e c^2}. \quad (45)$$

The inclusion of ξ_{DN} was shown to yield improved fits for late-time GRB170817A data (Ryan et al. 2023; Wang et al. 2024).

2.2.1 Electron distribution evolution

In order to calculate the time-dependent synchrotron and SSC radiation, we self-consistently evolve the electron LF distribution solving numerically the 1D continuity – Fokker-Plank-type – equation (Chandrasekhar 1943; Zhang 2018),

$$\frac{\partial N_e(\gamma_e, t')}{\partial t'} = - \frac{\partial}{\partial \gamma_e} \left[\dot{\gamma} N_e(\gamma_e, t') \right] + Q(\gamma_e, t') + Q_{pp}(\gamma_e, t'), \quad (46)$$

where $N_e(\gamma_e, t')$ is the number of electrons in the energy interval $[\gamma_e, \gamma_e + d\gamma_e]$ at time t' , $\dot{\gamma}$ is the rate at which electrons with LF γ_e

gain (if > 0) or lose (if < 0) energy, $Q(\gamma_e, t')$ is the injection term due to acceleration at a shock, and $Q_{pp}(\gamma_e, t')$ is the injection term due to pair production (PP).

For deriving Eq. (46) several approximations were made. We neglect the diffusion in energy space that would otherwise give a term $\partial/\partial \gamma_e [D_e(\gamma_e) \partial N_e / \partial \gamma_e]$; we neglect the electron escape term $-N_e(\gamma_e, t')/t_{e;esc}$, where $t_{e;esc}$ is the typical escape time scale of an electron with LF γ_e .

The source term, $Q(\gamma_e, t')$ in Eq. (46) describes the distribution with which electrons are injected into the system, which in our case is the power-law, $Q(\gamma_e, t') = Q_0 \gamma_e^{-p}$, where Q_0 is the normalization coefficient, that can be obtained by integrating the injection electron distribution from $\gamma_{e;m}$ to $\gamma_{e;M}$ as follows,

$$\begin{aligned} N_{e;inj}(t') &= \int_{\gamma_{e;m}}^{\gamma_{e;M}} Q(\gamma_e, t') d\gamma_e = \int_{\gamma_{e;m}}^{\gamma_{e;M}} Q_0 \gamma_e^{-p} d\gamma_e \\ &= Q_0 \frac{\gamma_{e;M}^{-p+1} - \gamma_{e;m}^{-p+1}}{1-p}. \end{aligned} \quad (47)$$

Since the total number of injected electrons is equal to the number of protons crossing the shock front, i.e., m/m_p , the final form of the source term reads

$$Q(\gamma_e, t') = \frac{m}{m_p} \left(\frac{1-p}{\gamma_{e;M}^{-p+1} - \gamma_{e;m}^{-p+1}} \right) \gamma_e^{-p} \quad (48)$$

for $\gamma_e \in (\gamma_{e;m}, \gamma_{e;M})$ and 0 otherwise.

The $\dot{\gamma}_e$ term in Eq. (46) describes heating and cooling processes that take place in system. Here, we consider the following contributions to this term,

$$\dot{\gamma} = \dot{\gamma}_{syn} + \dot{\gamma}_{adi} + \dot{\gamma}_{SSC}, \quad (49)$$

as described in detail below.

As BW evolves, the shocked region volume, $V' = m/\rho'$ increases, and electrons lose their energy to adiabatic expansion. Recalling that Eq. (10) can be written as $d(\gamma_e - 1)/dR = -(\dot{\gamma} - 1)(\gamma_e - 1)d \ln(V')/dR$, we can write the adiabatic cooling term for electrons as

$$\dot{\gamma}_{adi} = \frac{\gamma_e}{3} \left(\frac{\gamma_e^2 - 1}{\gamma_e} \right) d \ln(V'). \quad (50)$$

In the context of GRB afterglows, the shock magnetic fields are expected to be randomized. Then, the synchrotron emission power of a single electron is $P'_\gamma = (4/3)\sigma_T c \gamma_e^2 \beta_e^2 u_B'$, where β_e is the dimensionless velocity of an electron, obtained by averaging over the pitch angles (Rybicki & Lightman 1986). The synchrotron cooling rate, $\dot{\gamma}_{syn}$, of an electron then reads

$$\dot{\gamma}_{syn} = - \left(\frac{\sigma_T B'^2}{6\pi m_e c} \right) \gamma_e^2. \quad (51)$$

Before considering the last term in Eq. (49), it is worth noting that generally, only synchrotron cooling is considered in most GRB afterglow models, i.e., $\dot{\gamma}_e = \dot{\gamma}_{syn}$ in Eq. (49). In this case, and if the injection function is a power-law, $Q(\gamma_e, t') \propto \gamma_e^{-p}$, there exists an analytic solution to Eq. (46) (see, e.g., Sari et al. 1998). In fact, there exist two solutions, depending on the order of $\gamma_{e;m}$ (Eq. (42), Eq. (44)) and $\gamma_{e;c}$ (Eq. (38)). If the $\gamma_{e;m} < \gamma_{e;c}$, the resulting spectrum is generally referred to as being in a “slow cooling” regime, while the case of $\gamma_{e;m} > \gamma_{e;c}$ corresponds to the “fast cooling”

regime. The analytic spectra for both regimes is

$$N_e(\gamma_e) = K_f \begin{cases} \gamma_{e;M}^{1-p} \gamma_e^{-2} & \text{when } \gamma_{e;C} < \gamma_e < \gamma_{e;M}, \\ \gamma_e^{-p-1} & \text{when } \gamma_{e;M} < \gamma_e < \gamma_{e;M}, \end{cases} \quad (52)$$

$$K_f = \frac{m}{m_p} \left(\frac{\gamma_{e;C}^{-1} - \gamma_{e;M}^{-1}}{\gamma_{e;M}^{p-1}} + \frac{\gamma_{e;M}^{-p} - \gamma_{e;M}^{-p}}{p} \right)^{-1},$$

for the fast cooling and

$$N_e(\gamma_e) = K_s \begin{cases} \gamma_e^{-p} & \text{when } \gamma_{e;M} < \gamma_e < \gamma_{e;C}, \\ \gamma_{e;C} \gamma_e^{-p-1} & \text{when } \gamma_{e;C} < \gamma_e < \gamma_{e;M}, \end{cases} \quad (53)$$

$$K_s = \frac{m}{m_p} \left(\frac{\gamma_{e;C}^{1-p} - \gamma_{e;M}^{1-p}}{1-p} - \frac{\gamma_{e;C}(\gamma_{e;M}^{-p} - \gamma_{e;C}^{-p})}{p} \right)^{-1}.$$

for the slow cooling.

Normalization factors K_f and K_s in Eq. (52) and Eq. (53) are derived from the electron spectrum by first dividing the spectra (for both regimes) into two segments for both regimes as,

$$dN_e(\gamma_e) = \begin{cases} K_{f,1} \gamma_e^{-2} & \text{when } \gamma_{e;C} < \gamma_e < \gamma_{e;M}, \\ K_{f,2} \gamma_e^{-p-1} & \text{when } \gamma_{e;M} < \gamma_e < \gamma_{e;M}. \end{cases} \quad (54)$$

for the fast cooling

$$dN_e(\gamma_e) = \begin{cases} K_{s,1} \gamma_e^{-p} & \text{when } \gamma_{e;M} < \gamma_e < \gamma_{e;C}, \\ K_{s,2} \gamma_e^{-p-1} & \text{when } \gamma_{e;C} < \gamma_e < \gamma_{e;M}. \end{cases} \quad (55)$$

for the slow cooling, and then integrating the resulting BPLs as,

$$N_e = \int_{\gamma_{e;C}}^{\gamma_{e;M}} K_{f,1} \gamma_e^{1-p} \gamma_e^{-2} d\gamma_e + \int_{\gamma_{e;M}}^{\gamma_{e;M}} K_{f,2} \gamma_e^{-p-1}, \quad (56)$$

in the fast cooling regime, and

$$N_e = \int_{\gamma_{e;M}}^{\gamma_{e;C}} K_{s,1} \gamma_e^{-p} d\gamma_e + \int_{\gamma_{e;C}}^{\gamma_{e;M}} K_{s,2} \gamma_e^{-p-1}, \quad (57)$$

in the slow cooling regime. The final result is then obtained by combining the normalization factors of these BPL segments as,

$$K_{f,2} = \frac{N_e}{\gamma_{e;M}^{1-p} (\gamma_{e;C}^{-1} - \gamma_{e;M}^{-1}) - p^{-1} (\gamma_{e;M}^{-p} - \gamma_{e;M}^{-p})} \quad (58)$$

$$K_{f,1} = K_{f,2} \gamma_{e;M}^{1-p},$$

for the fast cooling regime and

$$K_{s,1} = \frac{N_e}{(1-p)^{-1} (\gamma_{e;C}^{1-p} - \gamma_{e;M}^{1-p}) - \gamma_{e;C} p^{-1} (\gamma_{e;M}^{-p} - \gamma_{e;C}^{-p})} \quad (59)$$

$$K_{s,2} = K_{s,1} \gamma_{e;C},$$

for the slow cooling regime. Substituting coefficients from Eqs. (58) (59) into Eq. (56) and (57) we obtained Eqs. (52) and (53).

This analytic solution is a foundation of most analytic synchrotron emission prescriptions commonly used in afterglow modeling. We implement it in `PyBlastAfterglow` for comparison with full numerical method.

Synchrotron photons produced by a population of electrons may also scatter on the same electrons. This is an SSC process (Rybicki & Lightman 1986). Notably, photons that have already been upscattered can interact with electrons again. However, this high orders scatterings are hampered by the Klein-Nishina effect, *i.e.*, the linear decrease of the scattering cross-section with the incident electron LF (Rybicki & Lightman 1986). Moreover, computing higher order scatterings is numerically expensive. Thus, we limit the implementation to only the first-order IC component. In order to obtain the energy loss rate due to SSC scatterings we need to convolve the scattering kernel with the seed photon spectrum, $n_{\tilde{\nu}'}$, estimation of which

we discuss later as it requires computing comoving emissivities first. The SSC cooling rate that includes Klein-Nishina correction is given by (Blumenthal & Gould 1970; Fan et al. 2008b; Geng et al. 2018),

$$\dot{\gamma}_{\text{SSC}} = \frac{3}{4} \frac{h\sigma_T}{m_e c \gamma_e^2} \int_{\tilde{\nu}'_0}^{\tilde{\nu}'_1} \frac{n_{\tilde{\nu}'}}{\tilde{\nu}'} \left[\int_{\nu'_0}^{\nu'_1} h\nu' K(\tilde{\nu}', \gamma_e, \nu') d\nu' \right] d\tilde{\nu}', \quad (60)$$

where $K(\dots)$ is the scattering kernel defined below, $\tilde{\nu}$ is the frequency of seed photons (before scattering) and ν is the photon frequency after the scattering, *i.e.*, the SSC photons.

The SSC kernel can be expressed as a function of normalized energy of incoming photons $\varepsilon = h\nu/(m_e c^2)$, energy of the electron, $\tilde{\varepsilon} = h\tilde{\nu}/m_e c^2$ and electron LF as follows (Jones 1968; Miceli & Nava 2022),

$$K(\tilde{\varepsilon}', \gamma_e, \varepsilon') = \frac{\varepsilon'}{\tilde{\varepsilon}} - \frac{1}{4\gamma_e} \text{ for } \frac{\varepsilon}{4\gamma_e} < \varepsilon < \tilde{\varepsilon} \quad (61)$$

and

$$K(\tilde{\varepsilon}', \gamma_e, \varepsilon) = 2q \ln(q) + (1+2q)(1-q) + 0.5(1-q) \frac{(4\gamma_e \tilde{\varepsilon} q)^2}{(1+4\gamma_e \tilde{\varepsilon})}, \quad (62)$$

$$\text{for } \tilde{\varepsilon} < \varepsilon < \frac{4\gamma_e^2 \tilde{\varepsilon}}{1+4\gamma_e \tilde{\varepsilon}},$$

where $q = \varepsilon/(4\gamma_e \varepsilon)/(\gamma_e - \varepsilon)$. Eq. (61) represents the down-scattering on an incoming photon and Eq. (62) stands for the up-scattering.

When low energy electrons re-absorb newly produced synchrotron photons in free-free transitions, they can gain energy. This process can be quantified with an SSA cross section (Ghisellini & Svensson 1991), and is referred to as SSA heating. At present, we do not consider this process for the sake of simplicity. However, it can be added as an additional heating $\dot{\gamma}_{\text{SSA}}^+$ term in Eq. (49) computed following (Gao et al. 2013). SSA becomes important when its characteristic frequency is larger than the cooling frequency, associated with $\gamma_{e;C}$. In this regime, called strong absorption regime, electrons may pile up at a $\gamma_{e; \text{pile-up}}$, that can be derived by balancing the cooling rate due to SSC losses and heating due to SSA. In the context of GRB afterglows, this regime was shown to occur in a RS when ejecta is moving through a dense wind medium (Kobayashi & Zhang 2003; Gao et al. 2013).

2.2.2 Comoving synchrotron spectrum

While in most cases of interest FS remains relativistic and $\langle \gamma_e \rangle \gg 1$, RS becomes relativistic only under certain conditions and generally $\Gamma_{43} \sim 1$ (Uhm et al. 2012). Thus, in computing synchrotron emissivity from an electron population we need to account for small electron LFs. This can be achieved by adding cyclo-synchrotron emissivity. An example of such an approach is given in Petrosian (1981). For the sake of computational efficiency we adopt here the following phenomenological expression for the comoving synchrotron emissivity from a single electron LF, $j'_{\text{syn}}(\nu', \gamma_e)$ (Ghisellini et al. 1998),

$$j'_{\text{syn}}(\nu', \gamma_e) = \frac{3q_e^3 B'}{m_e c^2} \frac{2p^2}{1+3p^2} \exp\left(\frac{2(1-x)}{1+3p^2}\right), \quad (63)$$

where $\gamma_e \leq 2$ and $p = \gamma_e^2 - 1$ is the electron dimensionless momentum, $x = \nu'/\nu'_L$ with ν'_L is the Larmor frequency, $\nu'_L = q_e B'/(2\pi m_e c)$.

Eq. (63) was shown to have the correct cooling rate (*i.e.*, Eq. (51)) when integrated over frequency; the correct frequency dependence,

$\propto \exp(-2x)$, at large harmonics ($x \gg 1$ in both non-relativistic and ultrarelativistic regimes). It was also shown to have better than 40% agreement with exact expressions at $\gamma_e = 2$ (Ghisellini et al. 1988).

For electrons with $\gamma_e > 2$ we can consider the standard synchrotron radiation formula averaged over isotopically distributed pitch angles (Aharonian et al. 2010),

$$j'_{\text{syn}}(\nu', \gamma_e) = \frac{3q_e^3 B'}{m_e c^2} 2y^2 \left(K_{4/3}(y) K_{1/3}(y) - \frac{3}{5} y (K_{4/3}^2(y) - K_{1/3}^2(y)) \right), \quad (64)$$

where $K_z(y)$ is the modified Bessel function of the order z , and $y = \nu' / \nu'_{\text{crit}}$ with

$$\nu'_{\text{crit}} = \frac{3 q_e B'}{4 \pi m_e c} \quad (65)$$

being the critical frequency.

However, it is numerically expensive to evaluate modified Bessel functions for all evolution time steps, all electron LFs and all frequencies, which would be required to compute the comoving spectra with Eq. (64). Thus, we follow Crusius & Schlickeiser (1986), who derived an exact expression for Eq. (64) in terms of Whittaker's function and Zirakashvili & Aharonian (2007) and Aharonian et al. (2010) who presented a simple analytical form that does not contain special functions. The synchrotron emissivity at a given frequency and electron LF then can be evaluated as,

$$j'_{\text{syn}}(\nu', \gamma_e) = \frac{3q_e^3 B'}{m_e c^2} \frac{1.808 y^{1/3}}{\sqrt{1 + 3.4 y^{2/3}}} \times \frac{1 + 2.21 x^{2/3} + 0.347 y^{4/3}}{1 + 1.353 y^{2/3} + 0.217 y^{4/3}} e^{-y}, \quad (66)$$

which was shown to agree with Eq. (64) within 0.2% accuracy.

The comoving synchrotron emissivity from a population of electrons at a given comoving time t' is evaluated by convolving the emissivity of one electron, $j'_{\text{syn}}(\nu', \gamma_e)$, with the electron distribution, $N_e(\gamma_e, t')$, as

$$j'_{\text{syn}}(\nu') = \int_{\gamma_{e;0}}^{\gamma_{e;1}} N_e(\gamma_e) j'_{\text{syn}}(\nu', \gamma_e) d\gamma_e, \quad (67)$$

where $\gamma_{e;0}$ and $\gamma_{e;1}$ are the lower and upper limits of the electron LF grid.

While we do not compute the SSA heating that affects primarily the electron distribution, we do account for SSA effects on the synchrotron radiation. The classical treatment for the SSA for the power-law electron distribution in the context of GRB afterglows was derived, *e.g.*, by Sari et al. (1998) and Granot et al. (1999). For an electron distribution that does not have a simple analytical form but under the one-zone approximation to the radiation isotropy assumption we can compute the SSA coefficient at a given radiation frequency as follows (Rybicki & Lightman 1986),

$$\alpha'_{\text{syn}}(\nu') = -\frac{1}{8\pi m_e \nu'^2} \times \int_{\gamma_{e;0}}^{\gamma_{e;1}} j'_{\text{syn}}(\nu', \gamma_e) \gamma_e^2 \frac{\partial}{\partial \gamma_e} \left[\frac{N_e(\gamma_e)}{\gamma_e^2} \right] d\gamma_e. \quad (68)$$

2.2.3 Comoving SSC spectrum

To compute the SSC radiation spectrum we follow Jones (1968); Blumenthal & Gould (1970); Miceli & Nava (2022). The comoving

emissivity at a given frequency and electron LF is,

$$j'_{\text{SSC}}(\nu', \gamma_e) = \frac{3}{4} h \sigma_T c \frac{\nu'}{\gamma_e^2} \int_{\nu'_0}^{\nu'_1} \frac{n_{\tilde{\nu}'}}{\tilde{\nu}'} F(\tilde{\varepsilon}', \gamma_e, \varepsilon') d\tilde{\nu}', \quad (69)$$

where $n_{\tilde{\nu}'}$ is the seed photon spectrum. It is evaluated as,

$$n_{\tilde{\nu}'} = n_{\tilde{\nu}'; \text{syn}} + n_{\tilde{\nu}'; \text{SSC}} = \left(\frac{j'_{\text{syn}}(\tilde{\nu}')}{h \tilde{\nu}'} + \frac{j'_{\text{SSC}}(\tilde{\nu}')}{h \tilde{\nu}'} \right) \frac{\Delta t'}{V'}, \quad (70)$$

where $\Delta t' = \Delta R / c = \Delta R \Gamma_{\text{sh}} / c$ is the comoving time that photons stay within the shocked region (Granot et al. 1999; Huang 2022), and ΔR is the shock thickness in the burster frame obtained with Eq. (35).

As stated before, we limit the number of scatterings to 1, *i.e.*, we compute Eq. (69) and Eq. (70) only once.

The SSC emissivity from a population of electrons is obtained as,

$$j'_{\text{SSC}}(\nu') = \int_{\gamma_{e;0}}^{\gamma_{e;1}} N_e(\gamma_e) j'_{\text{SSC}}(\nu', \gamma_e) d\gamma_e. \quad (71)$$

2.2.4 Pair-Production

High-energy photons may interact with other photons inside the source, producing an electron-positron pair before they are able to escape. This pair production (PP) process can be characterized with a cross section (Vernetto & Lipari 2016; Murase et al. 2011),

$$\sigma_{\gamma\gamma}(\beta') = \frac{3}{16} \sigma_T (1 - \beta_{\text{cm}}^2) \times \left[(3 - \beta_{\text{cm}}^4) \ln \left(\frac{1 + \beta'_{\text{cm}}}{1 - \beta'_{\text{cm}}} \right) - 2\beta'_{\text{cm}} (2 - \beta_{\text{cm}}^2) \right], \quad (72)$$

where β_{cm} is the center-of-mass speed of an electron produced in this process, that can be expressed as (Coppi & Blandford 1990),

$$\beta'_{\text{cm}} = \sqrt{1 - \frac{2}{\tilde{\varepsilon}' \varepsilon' (1 - \mu_{\gamma\gamma})}}, \quad (73)$$

where $\tilde{\varepsilon} = h\tilde{\nu}' / (m_e c^2)$ is the normalized energy of the target photon, $\varepsilon = h\nu / (m_e c^2)$ is the normalized energy of the incoming energetic photon, and $\mu_{\gamma\gamma} = \cos(\theta_{\gamma\gamma})$ is the angle between the directions of motion of two photons. *i.e.*, the scattering angle.

The annihilation rate then reads,

$$\mathcal{R}(\tilde{\varepsilon}, \varepsilon) = \frac{c}{2} \int_{-1}^{\mu_{\gamma\gamma; \text{max}}} \sigma_{\gamma\gamma}(\tilde{\varepsilon}, \varepsilon, \mu_{\gamma\gamma}) (1 - \mu_{\gamma\gamma}) d\mu_{\gamma\gamma}. \quad (74)$$

It was shown that Eq. (74) can be approximated with a simplified formula that is significantly cheaper to compute (Coppi & Blandford 1990),

$$\mathcal{R}(x) \approx 0.652 c \sigma_T \frac{x^2 - 1}{x^3} \ln(x) \Theta(x - 1), \quad (75)$$

where Θ is the Heaviside function and $x = \tilde{\varepsilon} \varepsilon$. This approximation was shown to agree with the exact formula within 7% accuracy (Miceli & Nava 2022).

The effect of the PP is twofold. A fraction of photons is lost, and a certain number of electrons is produced. Additional source of electrons enters Eq. (46) as an extra source term on the right-hand-side, $Q_{\text{PP}}(\gamma_e, t')$, that following Miceli & Nava (2022) we can write as,

$$Q_{\text{PP}}(\gamma_e, t') = 4 \frac{m_e c^2}{h} n_{\tilde{\nu}'_1} \int_{\nu'_0}^{\nu'_1} d\tilde{\nu}' n_{\tilde{\nu}'_1} \mathcal{R}(\tilde{\nu}'_1), \quad (76)$$

where $\tilde{\nu}'_\gamma$ is the frequency that corresponds to the electron with LF γ_e and is computed as $\tilde{\nu}'_\gamma = 2\gamma_e m_e c^2 / h$.

The PP effect on the photon spectrum is difficult to estimate since we do not evolve the comoving photon spectrum in the same way we evolve electron distribution. Thus, we resort to a common approximation where an attenuation of the spectrum that leaves the emitting region can be computed using optical depth (Huang et al. 2021),

$$\tau_{\gamma\gamma} = \frac{\Delta R'}{c} \int_{\nu'_1}^{\nu'_2} \mathcal{R}(\tilde{\nu}', \nu') n_{\tilde{\nu}'} d\tilde{\nu}'. \quad (77)$$

Then, the attenuation can be included by multiplying the total emissivity by $(1 - \exp(-\tau_{\gamma\gamma})) / \tau_{\gamma\gamma}$.

2.3 Radiative BW evolution

Deriving the BW evolution equations in Sec. 2.1, we introduced dE'_{rad} term – energy lost to radiation. Furthermore, in Sec. 2.2 we assumed that a fraction ϵ_e of shock downstream energy is used to accelerating electrons. These electrons can radiate a fraction ϵ_{rad} of their internal energy, affecting the underlying dynamics of the system (Piran 1999; Huang et al. 1999; Chiang & Dermer 1999; Dermer & Chiang 1998; Dermer & Humi 2001).

Given an electron distribution N_e and the corresponding comoving synchrotron spectrum j'_{syn} , the total energy loss rate reads, $u'_{\text{syn}; \text{tot}} = \int j'_{\text{syn}} d\nu'$. If the size of the emitting region is $\Delta R'$, then the photons escape time is $dt'_{\text{esc}} = \Delta R' / c$, and the total energy lost from the system is $dE'_{\text{rad}} = dt'_{\text{esc}} u'_{\text{syn}; \text{tot}}$.

Since we evolve the downstream electron distribution numerically we can in principle omit the commonly used assumption that electrons emit all their energy instantaneously. However, numerically it is to compute $u'_{\text{syn}; \text{tot}}$ at each sub-step of the adaptive step-size ODE solver when computing the BW dynamics.

A more efficient formulation of radiative losses can be derived by assuming an analytic BPL synchrotron spectrum that can be integrated analytically. Specifically, we employ classical fast and slow cooling spectra from Sari et al. (1998) (see their Eqs. (7) and (8)) and analytically integrate them from $\nu_0 = 10^6$ Hz to ν_M . The result reads,

$$\begin{aligned} u'_{\text{syn}; \text{tot}} &= \frac{3}{4} \left(\frac{1}{\nu_m} \right)^{\frac{1}{3}} \left(\nu_m^{\frac{4}{3}} - \nu_0^{\frac{4}{3}} \right) \\ &\quad - \frac{1}{3-p} \left(2 \left(\frac{1}{\nu_m} \right)^{\frac{1}{2}-\frac{p}{2}} \right) \left(\nu_m^{\frac{3}{2}-\frac{p}{2}} - \nu_c^{\frac{3}{2}-\frac{p}{2}} \right) \\ &\quad + \left(\frac{\nu_c}{\nu_m} \right)^{-\frac{p-1}{2}} \frac{2}{p-2} \left(\nu_c \nu_M^{\frac{p}{2}} - \nu_M \nu_c^{\frac{p}{2}} \right) \nu_M^{-\frac{p}{2}} \end{aligned} \quad (78)$$

if $\nu_m < \nu_c$ and

$$\begin{aligned} u'_{\text{syn}; \text{tot}} &= \frac{3}{4} \left(\frac{1}{\nu_c} \right)^{\frac{1}{3}} \left(\nu_c^{\frac{4}{3}} - \nu_0^{\frac{4}{3}} \right) \\ &\quad - \frac{2}{\sqrt{\nu_c^{-1}}} (\sqrt{\nu_c} - \sqrt{\nu_m}) \\ &\quad + \sqrt{\frac{\nu_c}{\nu_m}} \frac{2}{p-2} \left(\nu_m \nu_M^{\frac{p}{2}} - \nu_M \nu_m^{\frac{p}{2}} \right) \nu_M^{-\frac{p}{2}}, \end{aligned} \quad (79)$$

otherwise. In Eq. (78) and Eq. (79) all frequencies are in the comoving frame but the hyphen ' is omitted for clarity.

Characteristic frequencies, ν'_m , ν'_c , and ν'_M , are obtained from corresponding characteristic LFs, $\gamma_{e; i}$, as follows (Johannesson et al.

2006),

$$\nu'_i = \gamma_{e; i} \nu'_{\text{crit}} \begin{cases} 0.06 + 0.28p & \text{if } \gamma_{e; c} < \gamma_{e; m} \\ 0.455 + 0.08p & \text{if } \gamma_{e; m} < \gamma_{e; c}, \end{cases} \quad (80)$$

where ν'_{crit} is defined in Eq. (65). We compare this analytical approximant to the full numerical calculation of dE'_{rad} in Sec. 3.

More generally, the energy lost due to radiation can be expressed as $dE'_{\text{rad}} = -\epsilon_{\text{rad}} \epsilon_e dE'_{\text{sh}}$, where dE'_{sh} is the energy generated at the FS or RS (see Eq. (9) and Eq. (13)). If $\epsilon_{\text{rad}} \ll 1$ BW evolution is referred to as adiabatic, while if $\epsilon_e \epsilon_{\text{rad}} \simeq 1$ it is called radiative.

2.4 Emitting Region in Observer Frame

After the comoving emissivities and absorption coefficients are computed, we evaluate the observed radiation via equal time arrival surface (EATS) integration (e.g., Granot et al. 1999, 2008; Gill & Granot 2018; van Eerten et al. 2010).

In order to properly account for the light aberration, we compute the radiation transport through the thin shell that represents the emitting region in the observer frame. The conversions of comoving emissivity and absorption coefficients into the observer frame are (van Eerten et al. 2010), $j_\nu = j'_\nu / (\Gamma(1 - \beta\mu))^2$, $\alpha_\nu = \alpha'_\nu (\Gamma(1 - \beta\mu))$, where $\mu = \cos(\theta_{ij, \text{LOS}})$ is the angle between the BW angle (defined in the next section) and the line of sight (LOS). The transformation for the frequency reads $\nu' = \nu(1+Z)\Gamma(1 - \beta\mu)$, where Z is the source redshift.

For the uniform plane-parallel emitting region the radiation transport equation has an analytic solution,

$$I_\nu = \frac{j_\nu}{\alpha_\nu} (1 - e^{-\tau_\nu}) \cong j_\nu \times \begin{cases} -(e^{-\tau_\nu} - 1) / \tau & \text{if } \tau_\nu > 0 \\ (e^{-\tau_\nu} - 1) / \tau_\nu & \text{otherwise} \end{cases} \quad (81)$$

where I_ν is the intensity, the two cases correspond to the forward facing and back facing sides of a shock (Ryan et al. 2020) and $\tau_\nu \cong -\alpha_\nu \Delta R / \mu'$ is the optical depth in the observer frame with

$$\mu' = \frac{\mu - \beta}{1 - \beta\mu} \quad (82)$$

being the parameter relating the angle of emission in local frame to that in the observer frame (Granot et al. 1999). This parameter accounts for cases when light rays cross the ejecta shell along directions different from radial. The shock thickness in the observer frame is $\Delta R = \Delta R' / (1 - \mu\beta_{\text{sh}})$.

The observed flux density from a shock is then estimated by integrating over EATS using a spherical coordinate system that we discuss in Sec. 2.5, as

$$F_\nu = \frac{1+Z}{2\pi d_L^2} \int \int I_\nu(\theta, \phi) d\theta d\phi, \quad (83)$$

where d_L is the luminosity distance to the source.

High-energy photons propagating through the ISM may be absorbed by extragalactic background light (EBL). This effect can be accounted for by introducing additional optical depth following Franceschini & Rodighiero (2017). The authors compute a table of photon-photon optical depths, τ_{EBL} as a function of photon energy and redshift, Z . We use an updated table given in (Franceschini & Rodighiero 2017) and attenuate the observed flux as $F_\nu = F_\nu \exp(-\tau_{\text{EBL}})$.

2.5 Numerical Implementation

In this section, we detail numerical methods and techniques implemented in `PyBlastAfterglow` to solve the equations described in the previous subsections.

2.5.1 BW dynamics

After the initial conditions and settings are specified, the first stage of a simulation is the dynamical evolution of the BWs. Depending on the jet structure, the number of BWs can vary from 1 for a top-hat jet (*i.e.*, no lateral structure) to N for a structured (*e.g.*, Gaussian jet), specified by a user. For each BW, a set of ODEs is assembled. If the RS option is selected, the following equations are used: Eq. (16), Eq. (33), Eq. (24), Eq. (25), Eq. (8), Eq. (12), and Eq. (32). Otherwise, for a simulation with FS only the following equations are used: Eq. (29), Eq. (33), Eq. (8), and Eq. (32).

Sets of ODEs are combined for all BWs and solved simultaneously for a specified grid of time steps. Notably, when the RS is included ODE system can become stiff at the onset of the RS and the end of RS crossing the ejecta. We do not employ a special solver for stiff ODEs. Instead we implement an adaptive step-size explicit Runge-Kutta method of order 8(5,3) (Prince & Dormand 1981; Hairer et al. 1993; Suresh & Huynh 1997)³. Generally, we limit the number of time steps to 1000.

Note, if radiation losses are included, microphysics parameters, *i.e.*, ϵ_e ; fs, ϵ_b ; fs, p_{fs} ϵ_e ; rs, ϵ_b ; rs, p_{rs} are used to compute $dE'_{rad;2}$ and $dE'_{rad;3}$.

2.5.2 Comoving spectra

After BWs are evolved and the downstream properties for all shocks at all time steps are obtained, electron distribution is evolved, as well as comoving radiation spectra. For this purpose, we determine the injection electron spectrum by solving the system of equations given by Eqs. (42)-(44) using the bisection method. This allows us to compute the source term, Eq. (48), in the evolution equation. At the initial time step, we assume an analytic electron spectrum, given by Eq. (52) and Eq. (53). The seed photon spectrum is initialized with zeroes and is populated during the subsequent evolution step.

The electron distribution is evolved by solving the kinetic equation, Eq. (46). For this, we employ an unconditionally stable and particle number preserving fully implicit scheme (Chang & Cooper 1970; Chiaberge & Ghisellini 1999), which is a fully implicit difference scheme recently used in similar context (Huang 2022). Electron LF grid is initialized using equal logarithmic resolution from 1 to 10^8 . The grid intervals are $\Delta\gamma_{e;j} = \gamma_{j+1/2} - \gamma_{j-1/2}$, where quantities with the subscript $j \pm 1/2$ are calculated at half-grid points. In order to discretize the continuity equation, we define the number of electrons per grid cell at a given time step as

$$N_j^i = N(\gamma_{e,j}, i \times \Delta t), \quad (84)$$

where Δt is the time step that we will be discuss later. The particle flux between the grid cells is,

$$F_{j\pm 1/2}^{i+1} = \dot{\gamma}_{j\pm 1/2}^i N_{j\pm 1/2}^{i+1}. \quad (85)$$

The discretized form of Eq. (46) is given by

$$\frac{N_j^{i+1} - N_j^i}{\Delta t} = \frac{\dot{\gamma}_{e,j+1/2}^i N_{j+1/2}^{i+1} - \dot{\gamma}_{e,j-1/2}^i N_{j-1/2}^{i+1}}{\Delta\gamma_e} + Q_j^i, \quad (86)$$

³ For the numerical implementation of coefficients we followed <https://www.unige.ch/~hairer/software.html>

where $\dot{\gamma}_e$ is the total cooling rate specified in Eq. (49). The discretized form of continuity equation, Eq. (86), then becomes (Chang & Cooper 1970),

$$V3_j N_{j+1}^{i+1} + V2_j N_j^{i+1} + V1_j N_{j-1}^{i+1} = S_j^i, \quad (87)$$

where the V coefficients are:

$$\begin{aligned} V1_j &= 0, \\ V2_j &= 1 + \frac{\Delta t \dot{\gamma}_{e,j-1/2}}{\Delta\gamma_{e,j}}, \\ V3_j &= -\frac{\Delta t \dot{\gamma}_{e,j+1/2}}{\Delta\gamma_{e,j}}, \end{aligned} \quad (88)$$

and the source term is,

$$S_j^i = N_j^i + Q_j^i \Delta t. \quad (89)$$

Equation (87) forms a tridiagonal matrix equation that is solved via standard backwards substitution method.

Notably, the time step for the evolution has to allow electrons to cool, *i.e.*, it has to respect synchrotron cooling timescale,

$$\Delta t'_{syn} = \frac{\sigma_T \gamma_{e;M} B'^2}{6\pi m_e c}, \quad (90)$$

and adiabatic cooling timescale (due to the expansion of the emitting region),

$$\Delta t'_{adi} = \frac{\gamma_{e;M}^2 - 1}{3\gamma_{e;M}} \frac{1}{V'} dV', \quad (91)$$

where V' is the comoving volume. The maximum allowed time step, $\Delta t'$, then is determined by the Courant-Friedrichs-Lewy (CFL) condition as $\Delta t' = \Delta \ln(\gamma_e) / (\Delta t'_{syn} + \Delta t'_{adi})$. Notably, this $\Delta t'$ is not equal to the time step used for the BW evolution. If it is smaller, we perform a sub-stepping procedure between the main, BW evolution time steps. During sub-steps we fix the shock downstream properties and do not update radiation field for the sake of computational efficiency.

After the next evolution step is reached, we compute the comoving synchrotron emissivity (Eq. (67)) and the SSA coefficient (Eq. (68) with the derivative obtained via 1st order finite-differencing) as well as the SSC emissivity (Eq. (71)) using the photon field, n'_ν , from the previous time step. Then, we update the photon field (Eq. (70)) that is used later in computing SSC cooling (Eq. (60)) as well as the pair-production source term (Eq. (76)) during the next step. Notably, the innermost integral in Eq. (60) depends only on values that are known at the beginning of a simulation, – parameters of comoving electron LF and radiation frequency grids: ν' , $\tilde{\nu}'$ and γ_e . Thus, we compute it once at the beginning of the simulation. The updated photon field is also used to compute the absorption due to the PP (Eq. (77)).

Thus, for each BW evolution time step we build comoving emissivity and absorption spectra.

2.5.3 Jet Discretization and Observed Spectrum

Emission that an observer sees from a system of BWs, which represents a GRB jet, depends on the geometry of the system. We employ a spherical coordinate system (r, θ, ϕ) where r is the distance from the coordinate origin, and θ and ϕ are the latitudinal and azimuthal angles respectively. The central engine (post-merger remnant) is located at the coordinate origin, and the system's symmetry axis (z -axis) lies along $\theta = 0$. The observer is located in the $\phi = \pi/2$ plane and θ_{obs} is the angle between the LOS and the

z -axis. Thus, the unit vector of the observer is given by $\vec{n}_{\text{obs}} = (0, \sin(\theta_{\text{obs}})\vec{y}, \cos(\theta_{\text{obs}})\vec{z})$.

To construct a structured jet model we follow the approach suggested by Ryan et al. (2020), namely, we divide the into a set of independent BWs, each of which has a progressively larger initial half-opening angle. At the same time each hemisphere is discretized uniformly in terms of θ into rings assigned to each of the BWs, so that hemisphere is split into $k = \{0, 1, 2, \dots, n-1\}$ rings centered on the symmetry axis with boundaries $\theta_{i;1}$ and $\theta_{i;h}$, and with the ring center located at $\theta_{i;c} = (\theta_{i;h} - \theta_{i;1})/2$.

Observed radiation is obtained by summing contributions from each BW, using Eq. (83), that in turn is computed by integrating intensity over a given ring segment as,

$$F_\nu = \frac{1 + Z}{2\pi d_L^2} \sum_i^{\text{layers}} \int_{\theta_{i;1}}^{\theta_{i;h}} \int_{\phi_0=0}^{\phi_1=\pi/2} I_{i,\nu}(\theta, \phi) d\theta d\phi. \quad (92)$$

Afterwards, we account for the EBL absorption as discussed before.

2.5.4 Sky map calculation

A sky map is an intensity distribution projected onto a plane orthogonal to the line of sight (LOS). To compute it, we further discretize each ring (associated with the BW) into $S \in 1, 2, 3, \dots$ θ -subrings using an additional θ -grid uniform in $\cos\theta$. Then, we split each subring along the ϕ -axis into a set of Ω -cells in such a way that the resulted Ω -cells have the same solid angle. For example, the i -th subring is comprised of $2i + 1$ Ω -cells. Then, each ring has $\sum_{i=0}^{S-1} (2i + 1)$ cells in total.

For each cell that lies within the visible part of the ring at a given observer time and frequency, we compute the intensity $I_{i,\nu}(\theta, \phi)$. Numerically, we also make sure that at least 3 subrings fall between $\theta_{i;1}$ and $\theta_{i;h}$ and that each of those subrings has at least 3 non-zero Ω -cells. This is accomplished via an iterative algorithm that re-discretizes each ring into progressively more sub-rings and cells until the required conditions are met.

After the discretization, the coordinate vector of the i -cell in both is given by $\vec{v}_i = r_i (\sin(\theta_i) \cos(\phi_i)\vec{x}, \sin(\theta_i) \cos(\phi_i)\vec{y}, \cos(\theta_i)\vec{z})$. The cosine of the angle between the LOS and \vec{v}_i reads,

$$\mu_i = \sin(\theta_i) \sin(\phi_i) \sin(\theta_{\text{obs}}) + \cos(\theta_i) \cos(\theta_{\text{obs}}). \quad (93)$$

A sky map is computed by projecting the specific intensity on the x - z plane that is perpendicular to the LOS. We chose the basis with which the principal jet moves in the positive \tilde{x} -direction. The basis vectors of the plane then read,

$$\begin{aligned} \tilde{x}_i &= \sin(\theta_{\text{obs}})\vec{z}_i - \cos(\theta_{\text{obs}})\vec{x}_i, \\ \tilde{z}_i &= \vec{x}_i, \end{aligned} \quad (94)$$

and the coordinates of the ij cell on the image plane (for the principal jet) are given by

$$\begin{aligned} \tilde{x}_i &= -r_i [\cos(\theta_{\text{obs}}) \sin(\theta_i) \sin(\phi_i) + \sin(\theta_{\text{obs}}) \cos(\theta_i)], \\ \tilde{z}_i &= r_i \sin(\theta_i) \cos(\phi_i). \end{aligned} \quad (95)$$

In the following, we omit the use of tildes for simplicity.

In order to characterize sky maps we consider the surface brightness-weighted center of a sky map, also called image or a flux centroid, defined as

$$x_c = \frac{1}{\int I_\nu dx dz} \int x I_\nu dx dz, \quad (96)$$

and the x and z -averaged brightness distributions,

$$\begin{aligned} I_{\nu;m}(x) &= \frac{1}{\Delta z} \int I_\nu(x, z) dz, \\ I_{\nu;m}(z) &= \frac{1}{\Delta x} \int I_\nu(x, z) dx. \end{aligned} \quad (97)$$

2.5.5 Sky Map calculation

From the `PyBlastAfterglow` simulations we obtain the intensity distribution on the projection plane separately from each BW. These large unstructured arrays require post-processing to generate physically interpretable sky maps. We implement the following pipeline in a separate python code that is included in a python package that is released alongside the main code. First, ‘‘raw’’ sky maps are interpolated using the Delaunay triangulation for each BW onto a grid uniform in x and z . This is done separately for principle and counter jets for numerical reasons. Then, interpolated sky maps are used to integrate them along a given axes to compute the x - and z -averaged brightness distributions, that in turn allow us to compute the sky map size as a full width at half maximum (FWHM) of the distributions. In order to obtain a sky maps for plotting, we consider a 2D histogram with edges given by the same uniform grid in x and z . Then we bin ‘‘raw’’ sky maps with this histogram to obtain final intensity distribution $I(x, z)$. This procedure mimics how an observing instrument would collect photons from an extended source and is also used in other GRB afterglow models (e.g., Fernández et al. (2021)).

3 SIMULATION EXAMPLES

In this section we provide a comprehensive overview of several GRB afterglow simulations performed with `PyBlastAfterglow`. We focus on two main geometries of the jet: top-hat, where the jet is comprised of a singular BW, and commonly considered Gaussian jet, where distributions of BWs’ initial energy and LF follow a Gaussian. For both structures we perform two simulations: with FS only and with FS-RS system. We label these simulations as ‘‘top-hat-FS’’ and ‘‘top-hat-FS-RS’’ for the top-hat structure and similarly for the Gaussian one.

3.1 Top-hat-FS simulation

In this subsection we discuss the simulation with top-hat jet structure with initial isotropic equivalent energy of the burst being, $E_{\text{iso};c} = 10^{53}$ ergs, initial jet LF given as, $\Gamma_{0;c} = 400$, and the initial jet half-opening angle being, $\theta_w = \theta_c = 0.1$ rad, where the half-angle of the jet wings θ_w is the same as of the jet core, θ_c . The jet is expanding into the constant density ISM with $n_{\text{ISM}} = 1 \text{ cm}^{-3}$. Since the simulation is performed including FS, we implicitly assume that at the beginning of the simulation the RS has already crossed the ejecta. In this case, the region behind contact continuity is fully shocked and moves with LF Γ from the beginning. Microphysics parameters for FS are set as $\epsilon_{e;fs} = 0.1$, $\epsilon_{b;fs} = 0.001$, $p_{fs} = 2.2$, Unless stated otherwise, these parameters remain fixed for the discussion.

From given jet properties, the initial conditions for the BW evolution are,

$$\begin{aligned} E_0 &= E_{\text{iso};c} \sin^2(\omega_0/2), \\ \Gamma_0 &= \Gamma_{0;c}, \\ M_0 &= \frac{E_{\text{iso};c}}{(\Gamma_0 - 1)c^2} \sin^2(\omega_0/2), \end{aligned} \quad (98)$$

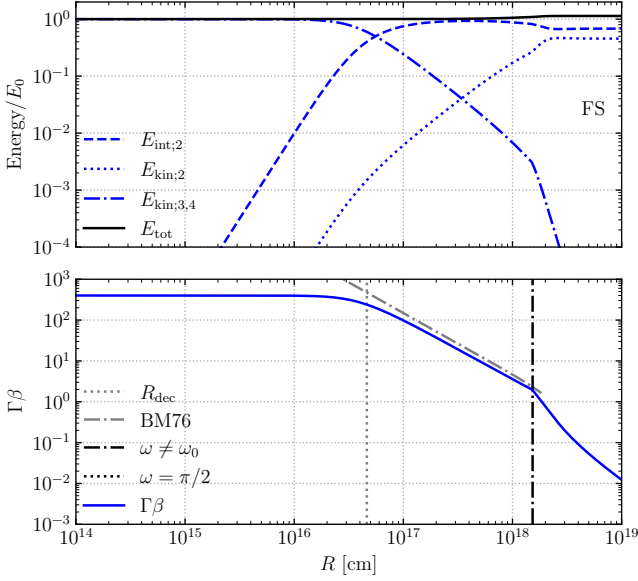


Figure 1. Energy (*top panel*) and momentum (*bottom panel*) for the BW from top-hat-FS simulation as a function of the BW radius R , computed as $R = \int t_{\text{burst}} \beta c$, where β is the BW dimensionless velocity. Here R_{dec} is the deceleration radius, $\omega \neq \omega_0$ indicates the onset of the lateral spreading; $\omega = \pi/2$ marks the end of spreading; BM76 indicates the analytic BM solution.

where Γ_0 , ω_0 , E_0 and M_0 are initial LF, half-opening angle, energy and mass, respectively.

3.1.1 BW dynamics and energy conservation

In Fig. 1 we show the example of the BW evolution. The evolution begins with the free-coasting phase, where BW momentum, $\Gamma\beta = \text{const}$. It continues until the amount of matter swept-up from the ISM becomes comparable to the BW mass at $R_d = (3E_{\text{iso},c}/(4\pi c^2 m_p n_{\text{ISM}} \Gamma^2))^{1/3}$. After that the kinetic energy of the shocked ejecta, $E_{\text{kin},3,4} = (\Gamma - 1)M_0 c^2$ starts to decrease as the energy is converted into internal energy of the shock downstream, $E_{\text{int},2} = \Gamma_{\text{eff},2} E'_{f,2}$. Kinetic energy in this stage, $E_{\text{kin},2} = (\Gamma - 1)mc^2$, also increases following the growing amount of mass swept up from the ISM.

During the deceleration phase, the BW LF asymptotically follows the BM solution, given as $\Gamma_{\text{BM}} = \sqrt{17E_{\text{iso},c}/(16\pi c^2 R^3)}$. We note that generally, a model based on a homogeneous shell does not fully agree with the BW solution for adiabatic evolution which is obtained by integrating the energy density of the shocked fluid over the extended (not a thin) shell. A possible solution is to add a normalization factor (N13). Here we omit it for simplicity.

Summing all the energy components we obtain total energy of the BW, $E_{\text{tot}} = E_{\text{kin},4} + E_{\text{kin},2} + E_{\text{int},2}$. Its evolution is shown with black line in Fig. 1. For most of the evolution the energy is conserved within $\sim 1\%$. However, when BW decelerates to $\Gamma\beta \sim 1$, the energy conservation violation reaches $\sim 10\%$, due to the limitations of our simple EOS (Eq. (2)), and the treatment of adiabatic losses. Notably, we find that the energy conservation at late times is improved if more accurate EOS for transrelativistic fluid is used, e.g., one presented in Pe'er (2012).

Once the conditions for the lateral spreading are satisfied (see

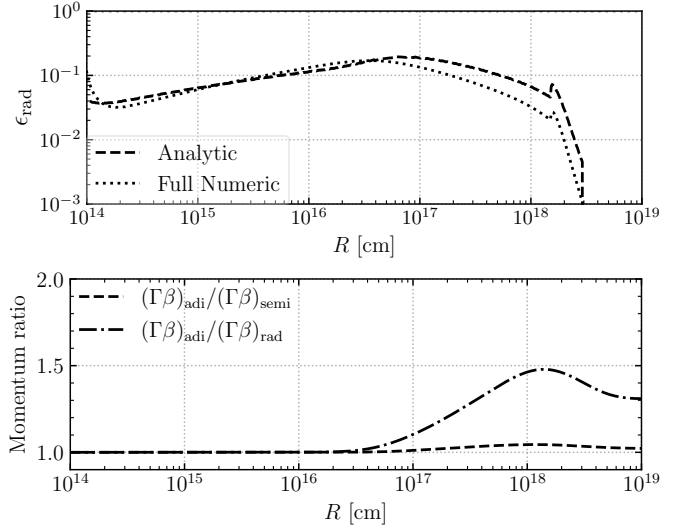


Figure 2. Effect of the radiative losses on the BW evolution in the top-hat-FS simulation. *Top panel* shows the evolution of the fraction of the shocked energy ($E'_{\text{rad},2}/E'_{\text{sh},2}$) lost to synchrotron radiation, i.e., ϵ_{rad} . The dotted line corresponds to this quantity computed using the synchrotron spectrum from self-consistently evolved electron distribution. The dashed line corresponds to ϵ_{rad} computed using an analytic integral over BPL approximation of synchrotron emission (Eq. (78) and Eq. (79)). *Bottom panel* shows the effect of radiative losses on the BW momenta, $\Gamma\beta$, evolution. For the sake of clarity, ratio of momenta is plotted. Dashed line corresponds to the case where adiabatic evolution is compared with semi-radiative evolution. Dash-dotted line corresponds to comparison of adiabatic evolution with fully radiative evolution, $\epsilon_{\text{rad}} = 1$.

Sec. 2.1.2) and $d\omega/dR$ becomes non-zero, the BW evolution starts to deviate from BM solution as $dm/dR \propto \omega$ in a non-linear way (see Eq. (32) and Eq. (33)). This behavior is expected and agrees with simplified numerical hydrodynamic solution (Granot & Piran 2012). Furthermore, we compare our dynamics during lateral spreading with a more sophisticated, 2D thin-shell hydrodynamics (HD) code in Sec. 4. After the BW half-opening angle reaches $\pi/2$, and when $\Gamma \sim 1$ the BW evolution enters the Taylor-von Neumann-Sedov (ST) regime and the following evolution proceeds with $\Gamma \propto R^{-3/2}$.

The effect of radiative losses term, $dE'_{\text{rad},2}$, in Eq. (8) on the BW evolution is shown in Fig. 2. When a fraction of the BW internal energy is lost to radiation, the BW decelerates faster. The strongest effect thus is achieved when all energy generated at the shock is lost to radiation, i.e., $\epsilon_{\text{rad}} = 1$, the so-called, fully radiative evolution. In the figure it is shown with dot-dashed line on the bottom subplot of the figure.

In semi-radiative regime, where ϵ_{rad} is obtained by integrating the synchrotron spectrum (Eq. (78) and Eq. (79)) the effect is the strongest when $\epsilon_e \rightarrow 1$ and $\epsilon_b \rightarrow 1$. For the values chosen for this simulation, however, $\epsilon_{\text{rad}} \simeq 0.1$, which implies that $E'_{\text{rad}}/E'_{\text{sh}} = \epsilon_e \epsilon_{\text{rad}} \simeq 0.01$, and BW evolves almost adiabatically as the bottom subplot of the figure shows.

In the top subplot of the figure we compare the analytic approximation to radiative losses (Eq. (78) and Eq. (79)) to the full numerical integration of the synchrotron spectrum (using Eq. (67)). While there is a small difference at late times, we do not find this difference to be noticeable in the BW evolution. Thus, we set the analytic method as a default option for the sake of computational speed.

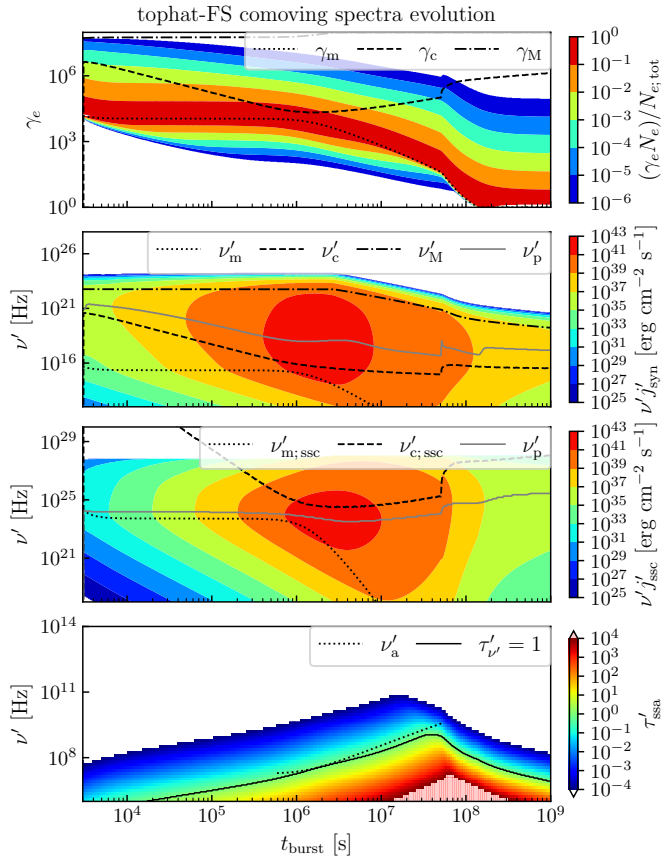


Figure 3. Comoving spectra evolution for the top-hat-FS simulation (without PP effects). *The top panel* corresponds to the electron spectrum. There, black dotted, dashed and dash-dotted lines indicate critical LF, $\gamma_{e,m}$ (Eq. (42)-(44)), $\gamma_{e,c}$ (Eq. (38)) and $\gamma_{e,M}$ (Eq. (40)) respectively. *The second panel* corresponds to the synchrotron spectrum (Eq. (67)) with black dotted, dashed and dash-dotted lines indicating critical LF, ν_m , ν_c , ν_M respectively, computed using Eq. (65) and Eq. (80). The solid gray line traces the frequency of the spectrum maximum. *Third panel* corresponds to the SSC spectrum (Eq. (71)), with black and gray lines computed as above but for the SSC process. *Fourth panel* corresponds to the SSA spectrum (Eq. (68)) shown in terms of the optical depth, τ'_{ν} , computed using comoving thickness of the shocked region. The black line marking there marks the location of $\tau'_{\nu} = 1$, where the spectrum transition from optically thin to optically thick. Dotted line corresponds to the analytic estimate, Eq. (99).

3.1.2 FS comoving spectra evolution

In Fig. 3, the evolution of comoving spectra is shown. The electron spectrum evolution is shown in the top panel of the figure alongside the characteristic LF. The spectrum is normalized such that at every time step the electron distribution N_e is divided by the total number of electrons obtained as $N_{e,tot} = \int N_e d\gamma_e$ and multiplied by electron LF, γ_e . This allows for an overall clarity but sacrifices some detail, e.g., the cooling LF $\gamma_{e,c}$ does not visibly follow contours of the plot. The same procedure is employed in, e.g., Bosnjak et al. (2009).

The subplot shows that at the beginning of the simulation the electron spectrum is confined between $\gamma_{e,m}$ and $\gamma_{e,M}$ following the analytical initial conditions for slow cooling regime (Eq. (53)) since $\gamma_{e,c} > \gamma_{e,m}$. During the evolution, a population of cooled electrons with $\gamma_e < \gamma_{e,m}$ grows. This is one of the key differences between an analytical and numerical electron spectra, shown

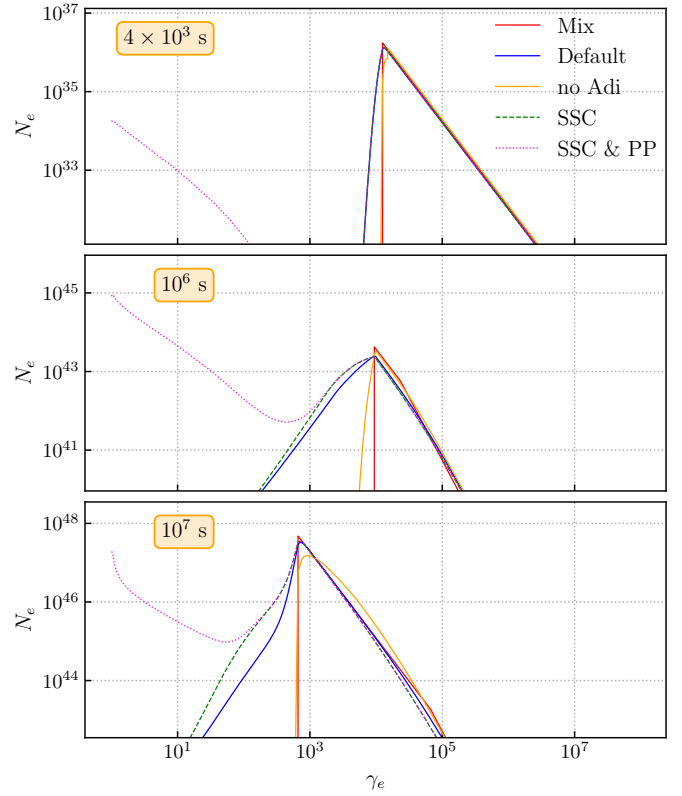


Figure 4. Electron distribution at three different time steps (one per panel) for three runs with different physics setups all related to the top-hat-FS simulations. “SSC & PP” run includes both SSC and PP processes; the “SSC” run accounts only for SSC process; the “Default” run does not include any of the above; and the “Mix” run corresponds to the simulation where electron distribution is not evolved (analytic BPL is assumed at each time step).

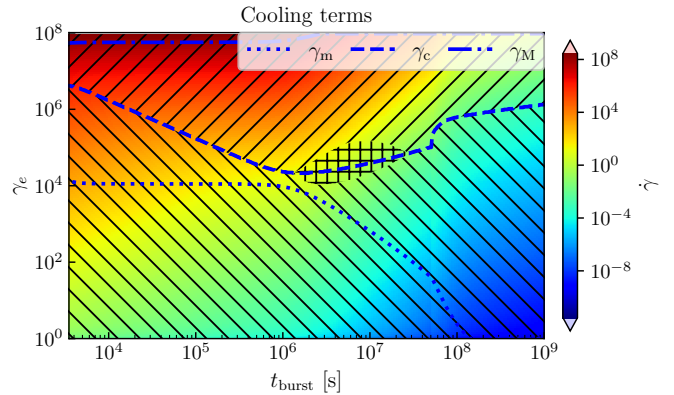


Figure 5. The total electron cooling rate (Eq. (49)) for the top-hat-FS simulation. Hatching indicates which cooling term dominates, where // hatches are used when $\dot{\gamma}_{syn} > \max(\dot{\gamma}_{adi}, \dot{\gamma}_{ssc})$, \\\ hatches are used when $\dot{\gamma}_{adi} > \max(\dot{\gamma}_{syn}, \dot{\gamma}_{ssc})$, and + hatches are used when $\dot{\gamma}_{ssc} > \max(\dot{\gamma}_{syn}, \dot{\gamma}_{adi})$. Also, characteristic LF computed with analytic expressions are shown with blue lines same as in the top panel of Fig. 3.

also in Fig. (4) at three time steps. Thus, at any given time, the electron distribution is comprised of the freshly injected electrons with $\gamma_e > \min(\gamma_{e,m}, \gamma_{e,c})$ and old, cooled electrons that occupy $\gamma_e < \min(\gamma_{e,m}, \gamma_{e,c})$.

To illustrate the effect of adiabatic cooling, *i.e.*, the $\dot{\gamma}_{\text{adi}}$ term in Eq. (49), on the electron distribution evolution we perform the same simulation setting $\dot{\gamma}_{\text{adi}} = 0$ and label it “no Adi”. The comparison with a simulations that includes adiabatic cooling (labeled as “Default”) is shown in Fig. 4. The figure highlights the importance of this term in developing low- γ_e part of the spectrum (see, *e.g.*, Geng et al. (2018) for similar analysis). Figure also shows the effects of SSC term (Eq. (60)) and the PP source term (Eq. (76)) on the electron spectrum. Both contribute to the formation of more extended low-energy tail of the spectrum.

A more detailed analysis of various contributors to the overall electron cooling throughout the BW evolution is shown in Fig. 5. The figure is divided into three areas marked by distinct hatching styles depending on which $\dot{\gamma}_e$ term is the largest. Additionally, analytically computed characteristic LFs are also shown for comparison. As expected synchrotron cooling dominates the overall cooling rate for $\gamma_e > \gamma_{e,c}$, at almost all times except for when $\gamma_{e,c}$ approaches $\gamma_{e,m}$ and SSC scattering becomes a dominate cooling process for electrons with $\gamma_e \simeq \gamma_{e,c}$, which is computed using Eq. (38) without the \tilde{Y} term. Electrons with $\gamma_e < \gamma_{e,c}$ cool primarily via adiabatic losses. Overall, the cooling rate, $\dot{\gamma}$, decreases with time and with electron LF as the color-coding in this figure indicates. Thus, at late times, when the injection LF is $\gamma_{e,m} \sim 1$, the electron spectrum becomes quasi-stationary. This can also be seen in Fig. 3, at the end of the BW evolution. Notably, since we evolve electron distribution in terms of electron LF, our implementation becomes increasingly accurate as $\gamma_e \rightarrow 1$.

The comoving synchrotron emissivity spectrum is shown in the second panel of Fig. 3. At the beginning of the simulation, the peak of the spectrum, ν'_p , coincides with the ν'_m . During the evolution, however, ν'_p shifts to higher frequencies as a fraction of electrons with $\gamma_e \lesssim \min(\gamma_{e,m}, \gamma_{e,c})$ grows. This can also be seen in Fig. 6, where comoving intensity spectrum, $\nu' I'_{\text{total}}$, is shown for three time steps for several physics setups. In particular, the figure shows that the synchrotron spectrum computed using an analytic electron spectrum (Eq. (52) and Eq. (53)) has lower ν'_p than the spectra computed with numerically evolved electron spectrum. Both the smoothness of the latter spectra and additional electron population with γ_e close to the lower boundary of the injection electron spectrum contribute to this outcome.

As the BW freely coasts, comoving magnetic field strength and injection spectrum do not evolve, but the number of particles radiating at every time step increases and so does the maximum synchrotron emissivity. It reaches its peak at the onset of BW deceleration. Throughout the entire BW evolution, the spectrum remains in the slow-cooling regime.

The last panel in Fig. 3 shows the SSA spectrum evolution in terms of the comoving optical depth, $\tau'_{\text{ssa}}(\nu') = \alpha'_{\text{syn}}(\nu') \Delta R'$. As the amount of matter swept-up by the FS increases so does the SSA optical depth. The frequency at which $\tau'_{\text{ssa}}(\nu') = 1$, *i.e.*, ν'_a , can be used to separate the optically thin (< 1) from optically thick (> 1) parts of the synchrotron spectrum. It is commonly referred to as SSA frequency, *e.g.*, Granot et al. (1999). The SSA frequency can be derived analytically, by additionally assuming that the BW follows the BM solution (Warren et al. 2018),

$$\nu'_a = 3.41 \times 10^9 \left(\frac{p+2}{3p+2} \right)^{3/5} \frac{(p-1)^{8/5}}{p-2}. \quad (99)$$

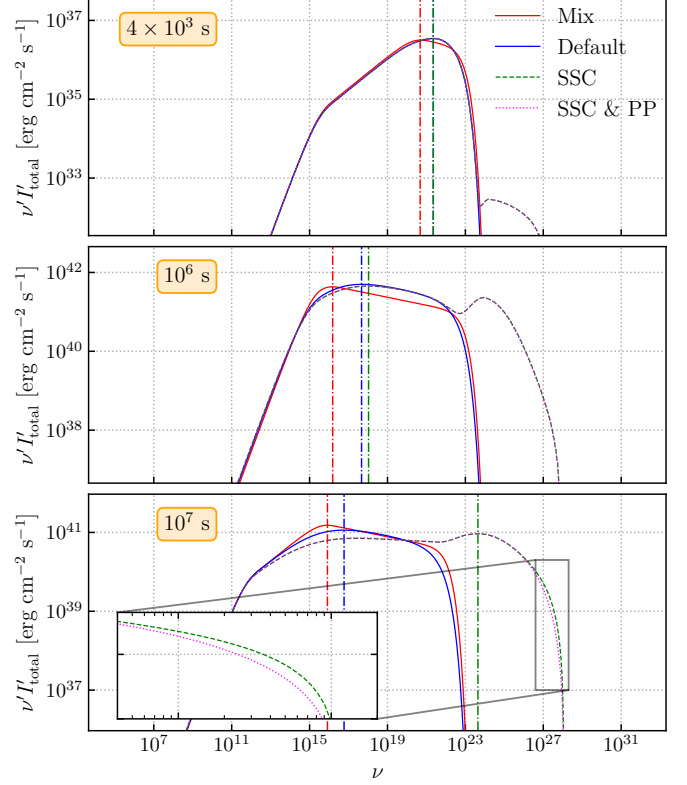


Figure 6. Total comoving intensity at three different time steps (one per panel) for three runs with different physics setup of the top-hat-FS simulations. The “SSC & PP” run includes SSC and PP; the “SSC” run includes only SSC, and the “Default” run does not include any of these two processes, and in the “Mix” run electron distribution is not evolved (analytic BPL is assumed at each time step). The enlarged subplot on the bottom panel shows the effect of the PP attenuation term (Eq. (77)) on the intensity. Here EBL absorption effect is included.

Equation (99) shows that ν'_a increases continuously with time during this stage of evolution. In the last panel of Fig. 3 we compare Eq. (99) with full numerical calculation of the ν'_a . Overall, the difference does not exceed a factor of 2 until BW starts to spread laterally and deviate from BM solution.

The third panel in Fig. 3 shows the evolution of SSC emissivity spectrum, j_{ssc} . The SSC emissivity corresponding to a given electron LF depends on the seed photon distribution (Eq. (69)). Thus, the integrated SSC spectrum (Eq. (71)), has a complex dependency on BW properties, comoving electron, and radiation spectra.

Characteristic frequencies of the spectrum are computed as

$$\nu'_{i;\text{ssc}} = \frac{4\sqrt{2}}{3} \nu'_{i;\text{syn}} \nu'_{e,i} \gamma_{e,i}^2, \quad (100)$$

where $\nu'_{i;\text{syn}} \in \{\nu'_m, \nu'_c\}$ and $\gamma_{e,i} \in \{\gamma_m, \gamma_c\}$, respectively.

It can be shown that the number of electrons that contribute to the SSC process around the peak is proportional to the number of electrons in the system, $j_{\text{ssc};\text{max}} \propto N_e$. This is reflected in the figure, where the maximum of the SSC qualitatively follows the evolution of the maximum of the synchrotron spectrum.

Notably, the Thomson optical depth for electron scattering, *i.e.*, the optical depth of electrons seen by a photon, defined as (Zhang 2018),

$$\tau_{\text{es}} = \sigma_T \frac{m}{m_p V'} \Delta R' \quad (101)$$

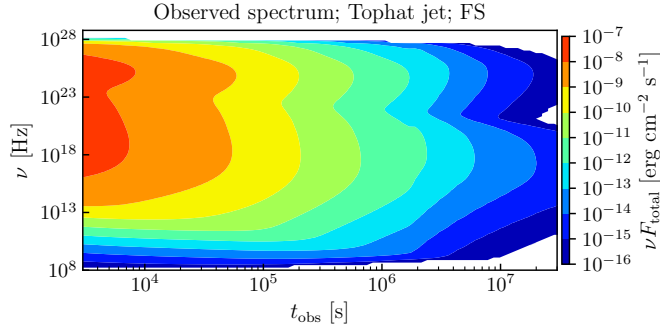


Figure 7. Time evolution of the observer spectrum from the top-hat-FS-RS simulation with SSC, PP SSA and EBL absorption turned on.

remains always $\ll 1$. Thus, when computing the SSC process, it is indeed sufficient to consider only one scattering process.

The effect of the SSC cooling term, Eq. (60), on the synchrotron spectrum is shown in Fig. 6 as a slight shift of the ν'_p to higher frequencies when SSC is included in the simulation.

The effect of the PP attenuation (Eq. (77)) is shown in the bottom panel of Fig. 6, in the enlarged subplot. As expected, SSC emissivity is reduced at highest frequencies. However, the effect is weak for a GRB jet settings chosen for the analysis.

3.1.3 Observed spectrum

In Fig. 7 the observed spectrum evolution computed via EATS integration from the simulation is shown. The spectrum has a distinct double-peak shape at all times with the high (low) energy peak corresponding to SSC (synchrotron) emission. At a given time, the SSC emission decreases sharply towards the highest frequencies primarily due to the EBL absorption.

3.2 Top-hat-FS-RS simulation

In this section, we review the top-hat-FS-RS simulation. This simulation is performed using the extended set of ordinary differential equations (ODEs) for BW dynamics based on Eq. (16) (see Sec. 2.5). Microphysics parameters for the RS are set as follows, $\epsilon_{e,rs} = 0.1$, $\epsilon_{b,rs} = 0.001$, $p_{rs} = 2.2$ (i.e., the same as those for the FS: see §3.1), while the burst duration that defines initial ejecta shell width is $t_{\text{prmp}} = 10^3$ s.

As before, we first discuss the BW dynamics and then the electron and radiation spectra. However, as we are going to show, the presence of the RS alters the dynamics of the FS. However, for the sake of brevity, we focus only on the RS itself in this section.

3.2.1 BW dynamics and energy conservation

Fig. 8 shows the evolution of different energy components of the BW (upper panel) as well as its bulk LF (lower panel). The RS shock starts with non-relativistic $\Gamma_{43} \sim 1$ and accelerates as it moves through the ejecta. Then its kinetic energy, defined as $E_{\text{kin};3} = (\Gamma - 1)m_3c^2$, increases. As the mass of the shocked material grows, the internal energy, $E_{\text{int};3} = \Gamma_{\text{eff};3}E'_{\text{int};3}$ also rises while the bulk LF of the BW steadily falls. Shortly before the RS crosses the ejecta, it becomes relativistic with $\Gamma_{43} \gg 1$ and total energy $E_{\text{kin};3} + E_{\text{int};3}$ reaches $\sim 10\%$ of the total BW energy.

As in the case with the simulation where only FS is included, we

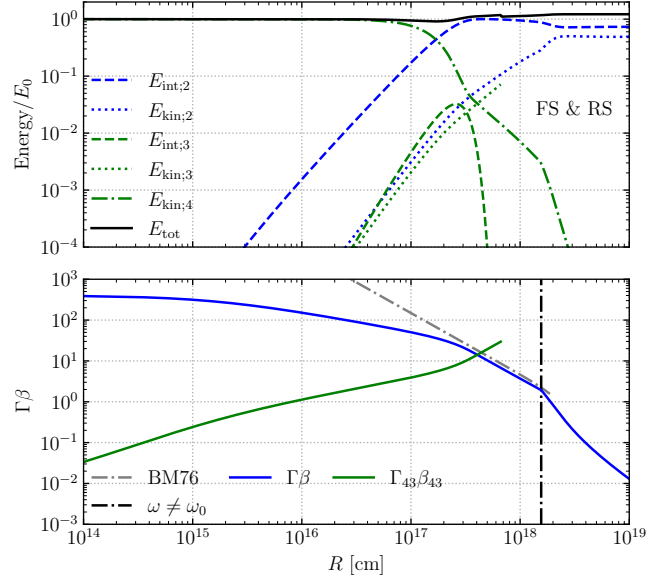


Figure 8. Energy (top panel) and momentum (bottom panel) for top-hat-FS-RS simulation. As in Fig. 1, $\omega \neq \omega_0$ indicates the onset of the lateral spreading $\omega = \pi/2$ marks the end of spreading; BM76 is the analytic BM solution. When the RS crosses the ejecta, its evolution terminates. This is indicated in the evolution of $E_{\text{kin};3}$ on the top panel and $\Gamma_{34}\beta_{34}$ in the bottom one.

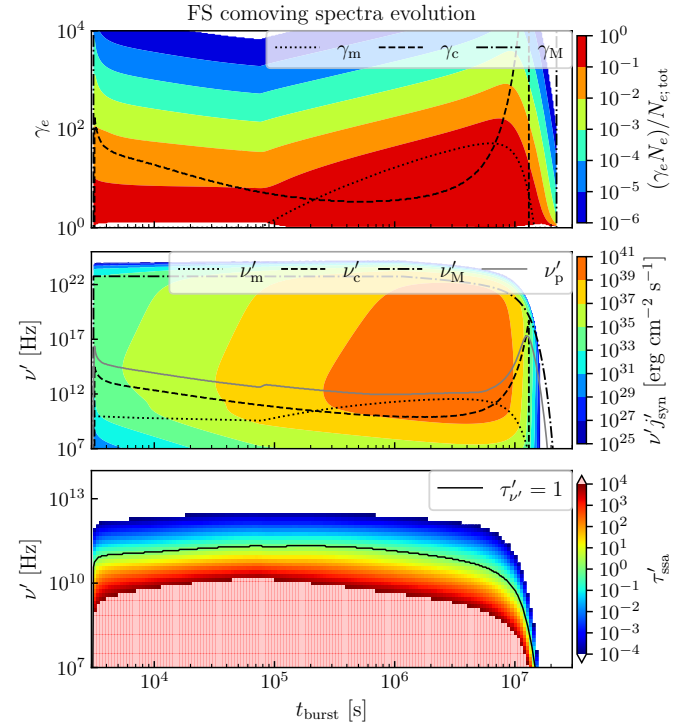


Figure 9. Same as Fig. 3 but for the RS. Top, middle and bottom panels correspond to the electron, synchrotron and SSA spectra respectively.

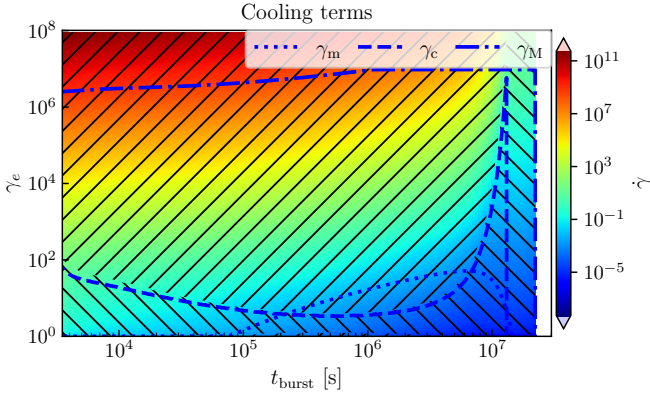


Figure 10. Same as Fig. 5 but for the RS.

find that the total energy is conserved within $\sim 1\%$ during the early evolution stages. However, when the RS becomes relativistic, the total energy conservation violation reaches $\sim 20\%$. This is due to our simplified treatment of ejecta profile in the upstream and EOS.

While in the top-hat-FS simulation a large part of the BW evolution – after the onset of deceleration and before lateral spreading – can be described with the BM solution, in the top-hat-FS-RS simulation, only after the RS crossing time does the BW follow the self-similar solution.

3.2.2 Comoving spectra evolution

Comoving spectra from the RS are shown in Fig. 9. Conditions at the RS differ significantly from those at FS. Most importantly, while FS starts highly relativistic and remains so (freely coasts) until the deceleration at late times, eventually reaching $\Gamma_{\text{fsh}} \simeq 1$ at very late times, the RS starts with $\Gamma_{\text{rsh}} \simeq 1$ and then accelerates gaining maximum momentum shortly before it traverses the entire ejecta shell. Thus, at the beginning, the electron distribution in the RS downstream is confined to $\gamma_e \lesssim 10$ as shown in the top panel of Fig. 9. Notably, only a fraction of particles crossing the shock is being injected, *i.e.*, $\xi_{\text{DN}} < 1$ (see Eq. (45)).

When $\gamma_{e;m}$ increases above 1 the fraction ξ_{DN} becomes 1 and the electron spectrum displays a sharp change as shown in the figure. This feature is largely a numerical artifact as electrons cannot have $\gamma_e < 1$ and thus only when $\gamma_{e;m} > 1$ can electrons cool to $\gamma_e < \gamma_{e;m}$. As RS accelerates, $\gamma_{e;m}$ grows rapidly while $\gamma_{e;c}$, computed using Eq. (38), decreases and spectrum enters the fast cooling regime. The spectral regime changes again only at the end, when the upstream density for the RS starts to decline exponentially (Eq. (26)). At this point internal energy density behind the RS starts to decrease rapidly and so does $\gamma_{e;m}$. As Fig. 10 shows, throughout most of the evolution, synchrotron cooling remains the dominant cooling process.

The synchrotron emissivity spectrum is shown on the second panel of Fig. 9. The spectral peak does not evolve as significantly. It remains between optical and radio bands till the shock crosses the ejecta.

As the upstream density for the RS is significantly larger than the ISM density and the shock itself is slower than the FS. Thus, the SSA plays a more significant role here. Specifically, radio emission at $\nu' < 10^{11}$ Hz is self-absorbed. This is reflected in the bottom panel of Fig. 9. The self-absorbed radio spectrum from the RS in

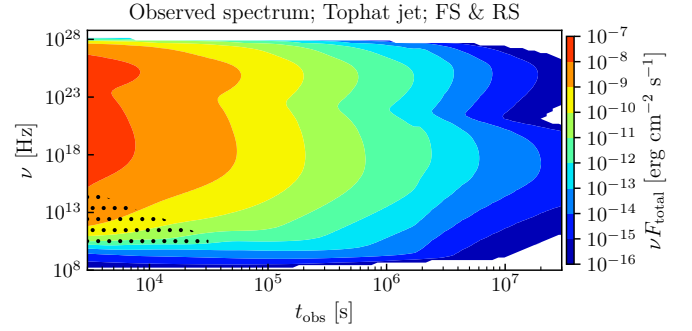


Figure 11. Time evolution of the observer spectrum from the top-hat-FS-RS simulation with SSC, PP and EBL absorption turned on for the FS emission and SSA for both shocks. The area where RS emission is brighter than the FS one is indicated with \cdots hatches.

GRBs is indeed expected theoretically (Gao & Mészáros 2015) and there is observational support for it as well (Laskar et al. 2019).

3.2.3 Observed spectrum

In Fig. 11 the observed spectrum evolution, computed via EATS integration from the simulation is shown. Comparing this figure with Fig. 7 we note that the RS emission contributes primarily at the lower end of the spectrum. At the lowest frequencies, the SSA process becomes important and the spectrum shows a steep decline.

3.2.4 Sky map

Sky maps for the top-hat-FS-RS simulation are shown in Fig. 12 for several observer times and separately for the FS and for the RS (second and third panels, respectively). There we set $\nu_{\text{obs}} = 1$ GHz and set $\theta_{\text{obs}} = \pi/4$ rad. The figure shows that as the RS is significantly slower than the FS its emission is less subjected to the Doppler beaming and thus the counter jet overtakes the principle jet in brightness much earlier in this case. The total sky map, however, is dominated by the emission from the RS at very early times, when the FS emission is beamed away from the LOS. As the Doppler beaming decreases, the contributions from two shocks to the principle jet sky map becomes comparable. This transition is shown in the second column of panels in the figure. This is also the point where the position of the total sky map flux centroid is most affected by the emission from the RS.

3.3 Gaussian-FS-RS simulation

In this subsection we discuss properties of the Gaussian-FS-RS simulation. The simulation parameters are set as follows: $E_{\text{iso;c}} = 10^{53}$ ergs, $\Gamma_{0;c} = 400$, $\theta_c = 0.1$ rad. $\theta_w = 0.3$ rad. As before, we assume ISM with constant density, $n_{\text{ISM}} = 1 \text{ cm}^{-3}$. Microphysics parameters are set as follows: $\epsilon_{e;fs} = 0.1$, $\epsilon_{b;fs} = 0.001$, $p_{fs} = 2.2$, $\epsilon_{e;rs} = 0.1$, $\epsilon_{b;rs} = 0.001$, $p_{rs} = 2.2$. For the RS, we also set $t_{\text{prompt}} = 10^3$ sec. The jet is discretized into 21 layers, each of which is represented by a BW, (see Sec. 2.5).

The Gaussian jet structure implies that BW initial conditions follow the Gaussian distribution, where BW initial energy, LF and mass

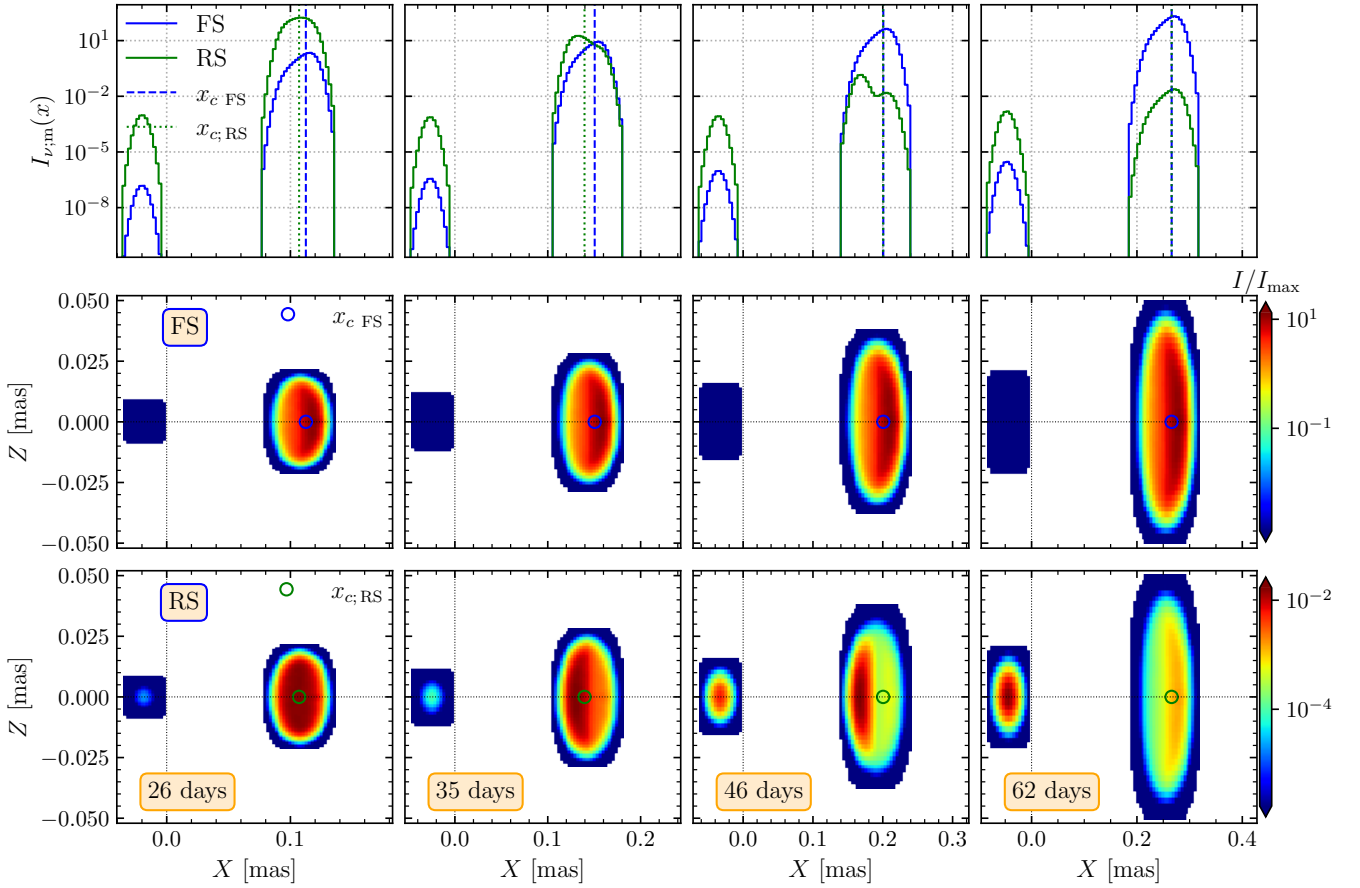


Figure 12. Radio sky maps of the top-hat-FS-RS simulation observed at $\theta_{\text{obs}} = \pi/4$ rad. at different times (panel columns) as indicated by the text at the bottom left of the last panel in a column. The top row of panels shows intensity integrated along the z axis, $I_{\nu; m}(x)$. There the green (blue) line corresponds to the sky map of associated with the RS (FS) emission only. Second and third rows of panels show sky maps compute from FS and RS emission respectively. Moreover, each sky map is composed of the image associated with the principle and counter jets that lie on the right and left sides with respect to the origin, $X = 0$, respectively. Circular markers indicate the location of the flux centroid, x_c . Location of the flux centroid for both sky maps is also shown in the top row of panels with dashed and dotted vertical lines.

are given as,

$$\begin{aligned}
 E_{0; i} &= E_{\text{iso}; c} \sin^2 \left(\frac{\theta_{i; h}}{2} \right) \exp \left(- \frac{1}{2} \frac{\theta_{i; c}^2}{\theta_c^2} \right), \\
 \Gamma_{0; i} &= 1 + (\Gamma_{0; c} - 1) \frac{E_{0; i}}{\sin^2 \left(\theta_{i; h} / 2 \right) E_{\text{iso}; c}}, \\
 M_{0; i} &= \frac{E_{0; i}}{(\Gamma_{0; i} - 1) c^2},
 \end{aligned} \tag{102}$$

where $\theta_{i; c}$ is the center of a ring corresponding to a given BW and $\theta_{i; h}$ is the outer boundary of the ring (see Sec. 2.5.3).

Dynamics of different BWs is shown in Fig. 13. Each BW goes through standard evolution stages: free-coasting, deceleration due to RS crossing, BM-like deceleration, lateral spreading enhanced deceleration and finally, ST-like deceleration. The RS is weaker in slower BWs and thus does not significantly affect the BW evolution, *i.e.*, the free-coasting phase continues until the classical deceleration radius R_d . Importantly, during the evolution of all BWs the total energy is reasonably well conserved.

Evolution of the observed spectra is shown in Fig. 14, where spectra from two layers and the total spectrum from the entire jet are displayed in separate panels. As the observer angle is set to $\theta_{\text{obs}} = 0$ rad, the LOS passes through only one layer, layer=0 in the core of the jet. Other layers are seen off-axes and thus are vis-

ible only after BW deceleration reduces the Doppler beaming. This is reflected in the spectra of individual layers reaching their respective maxima at later times depending on their position within the jet structure.

At all times the spectra show two peaks corresponding to the synchrotron and the SSC emissions. The RS emission contribution is seen for longer and for more off-axis layers as Doppler beaming reduces the contribution from the FS there. The SSA plays an important role there and cuts off spectrum at early times and for slower BWs.

The sky maps for this simulation, observed at an angle of $\theta_{\text{obs}} = \pi/4$ rad are shown in Fig. 15. The RS emission affects primarily part of the sky map that corresponds to the core of the jet as the RS is stronger and faster in corresponding BWs (see Fig. 13). However, because the jet energy is now distribution among fast and slow BWs, RS stops significantly contributing to the total emission much earlier than in top-hat-FS-RS simulation.

4 COMPARISON

In this section we compare `PyBlastAfterglow` with two publicly available afterglow codes: `afterglowpy` (Ryan et al. 2020,

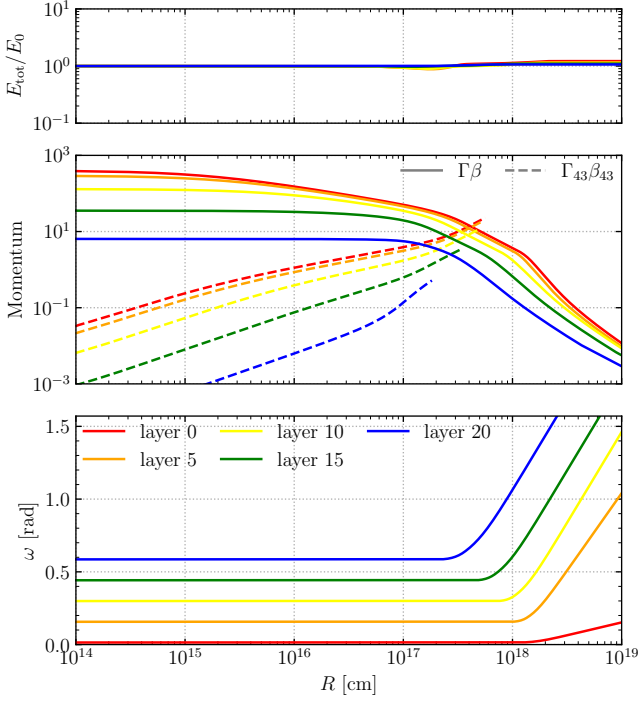


Figure 13. Dynamics of several BWs (layers) of a structured, Gaussian jet, where layer=0 BW corresponds to the core of the jet (and thus it has the smallest initial half-opening angle and the largest initial momentum). *Top panel* shows the total energy of each BW divided by its initial energy. If energy is conserved during the evolution $E_{\text{tot}}/E_0 = 1$. *Second panel* shows the evolution of the BW momentum $\Gamma\beta$ alongside the evolution of the momentum corresponding to the RS ($\Gamma_{43}\beta_{43}$). *Third panel* shows the evolution of the BW half-opening angle, ω , offset by half-opening angle assigned to the BW within a structured jet, $\omega_{0,l}$ (see Sec. 2.5.3).

2023) and jetsimpy (Wang et al. 2024). Both codes can generate light curves and sky maps of GRB afterglows. At the time of writing they only include synchrotron emission from the FS from a top-hat or a structured jet. Both codes assume similar EOSs for the transrelativistic ideal fluid and the same analytical prescription for computing the synchrotron emissivity, *i.e.*, BPL spectrum (Sari et al. 1998).

In these codes the observed radiation is computed through the EATS integration, where the synchrotron emissivity in the observer frame is computed from the interpolated BW properties. In other words, at each observer time and frequency, the radiation is evaluated from an interpolated state of the BW. This is more computationally efficient than evaluating entire comoving spectra at each BW evolution time step and then interpolating those spectra for a given observer time and frequency. However, by construction this approach does not allow for the continuous evolution of electron and photon spectra and thus has limited flexibility.

While the two codes chosen for the comparison share a lot in common, there are significant differences between them. *afterglowpy* discretizes a BW into a set of overlapping (in terms of angular extend) BWs with progressively larger initial half-opening angle each of which is evolved independently from each other under the standard 1D thin-shell formulation. This is similar to what we employ in *PyBlastAfterglow*, especially to the setup when only FS is evolved (see Sec. 2.5). The code assumes that each BW starts in the BM deceleration phase. It is worth noting, how-

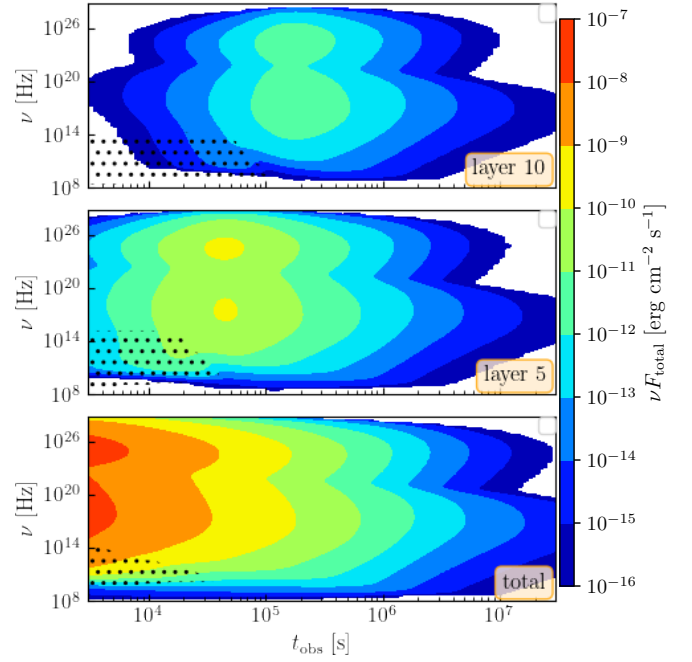


Figure 14. Observed spectrum evolution for Gaussian-FS-RS simulation. First two panels show spectra from individual BW within the jet, while the last panel shows the total, summed spectrum. Dotted hatched regions in each panel indicate where flux density from RS exceeds that from the FS as in Fig. 11.

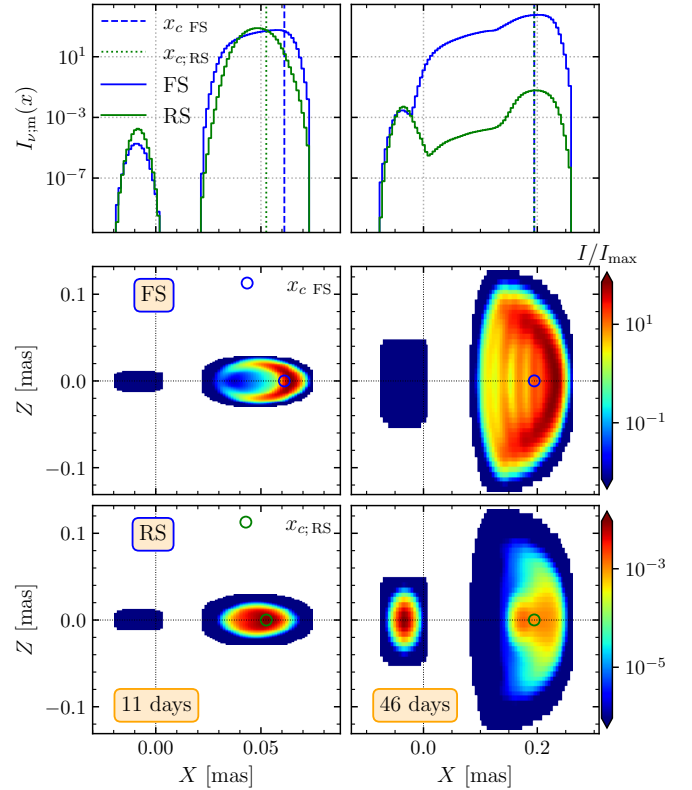


Figure 15. Same as Fig. 12 but for the Gaussian-FS-RS simulation, where the jet is observed at $\theta_{\text{obs}} = \pi/4$ rad.

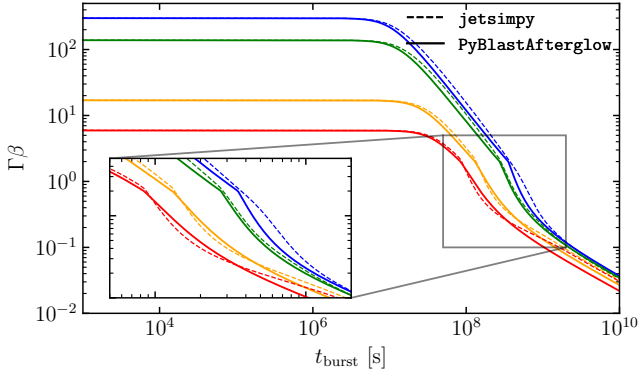


Figure 16. Comparison with *jetsimpy* in terms of time evolution of the BW momentum for several layers. Simulation is performed with a Gaussian lateral structure (Eq. (102)) and with FS only and the following model parameters: $n_{\text{ism}} = 0.00031 \text{ cm}^{-3}$, $E_{\text{iso}} = 10^{52} \text{ ergs}$, $\Gamma_0 = 300$, $\theta_c = 0.085 \text{ rad}$ and $\theta_w = 0.2618 \text{ rad}$. Each color corresponds to one of the BWs that *PyBlastAfterglow* evolves. *jetsimpy* values are taken by extracting $\Gamma\beta$ at the times, t_{burst} , and half-opening angle ω (see text).

ever, that the free-coasting phase can be enabled in *afterglowpy* source code. *jetsimpy* approximates a jet as a 2D infinitesimally thin sheet of matter. In this formulation, internal pressure that drives the lateral expansion is included self-consistently. Thus, the code approximates the hydrodynamics of a laterally spreading jet more accurately. The code is further calibrated to hydrodynamic self-similar solutions wherever and includes the early free-coasting phase of the BW evolution. This, in turn, allows for more accurate modeling of early afterglow phase (see figure 6 in Wang et al. (2024)).

We expect *PyBlastAfterglow* to agree with *jetsimpy* before the onset of lateral expansion, as the free-coasting phase is included in both codes, and with *afterglowpy* at late times due to similar treatment of lateral spreading. However, large differences in microphysics and radiation methods would make the comparison difficult. In order to have an intermediate point of comparison, we implemented an analytical synchrotron radiation prescription following Sari et al. (1998); Wijers & Galama (1999). This configuration of our code is labeled as *PyBlastAfterglow** in figures.

4.1 Dynamics

Since *PyBlastAfterglow* evolves separate BWs for different jet angular layers, while *jetsimpy* considers a single 2D BW, one-to-one comparison of the BW dynamics is not trivial. We interpolate the *jetsimpy* BW properties for each time, t_{burst} , and half-opening angle, ω , that a *PyBlastAfterglow* BW attains during its evolution. We do this for several BWs of our code. The result is shown in Fig. 16.

Predictably, the largest deviation in BW dynamics with respect to occurs near the onset of lateral spreading, at late stages of BW deceleration. At this point different elements of the laterally structured jet come into casual contact with each other and non-linear effects become important. An analytical prescription for the lateral spreading implemented in *PyBlastAfterglow*, e.g., Eq. (32), cannot fully capture this effect. In part this can be mitigated by including a lateral spreading prescription that is “aware” of the jet structure at all times and naturally mimics the effects found in 2D simulations. Notably, since in *PyBlastAfterglow* all BWs are evolved si-

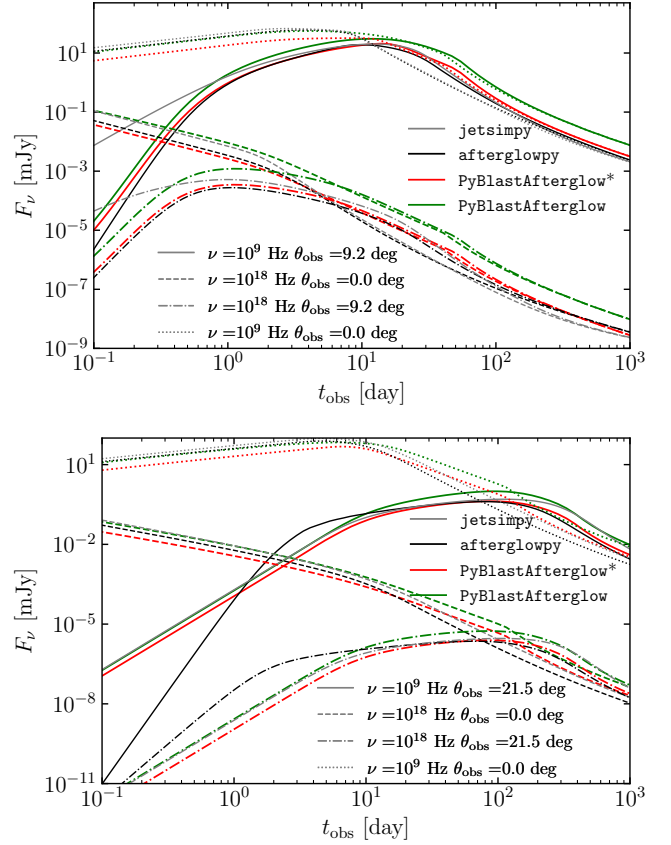


Figure 17. Comparison between *PyBlastAfterglow* (red and grid lines), *afterglowpy* (black lines), and *jetsimpy* (gray lines) in terms of light curves. The top panel shows comparison for the jet with top-hat lateral structure (Eq. (98)) and the following parameters: $d_L = 3.09 \times 10^{26} \text{ cm}$, $Z = 0.028$, $n_{\text{ism}} = 10^{-2} \text{ cm}^{-3}$, $E_{\text{iso}} = 10^{52} \text{ ergs}$, $\Gamma_0 = 350$, $\theta_c = \theta_w = 0.1 \text{ rad.}$, $\epsilon_e = 0.1$, $\epsilon_b = 0.1$ and $p = 2.2$. The bottom panel corresponds to the jet with the Gaussian lateral structure (Eq. (102)), with the following parameters: $d_L = 1.27 \times 10^{26} \text{ cm}$, $Z = 0.0099$, $n_{\text{ism}} = 0.00031 \text{ cm}^{-3}$, $E_{\text{iso}} = 10^{52} \text{ ergs}$, $\Gamma_0 = 300$, $\theta_c = 0.085 \text{ rad.}$ and $\theta_w = 0.2618 \text{ rad.}$, $\epsilon_e = 0.0708$, $\epsilon_b = 0.0052$ and $p = 2.16$. In both cases only FS is considered. Different line styles indicate various observer angles and observer frequencies. *PyBlastAfterglow** runs, depicted with red lines, were performed using analytic synchrotron spectrum and not evolving electron distribution.

multaneously (see Sec. 2.5) such prescription can indeed be implemented. However, we leave this to a future work. Meanwhile, we find that two codes agree the most when comparing dynamics of the inner layers of the jet (far from the core or the edge of the jet).

4.2 Light curves and sky maps

Light curve comparison is shown in Fig. 17 for the top-hat jet (top panel) and the Gaussian jet (bottom panel), where parameters for the latter are chosen to be similar to those inferred for GRB170817A (Fernández et al. 2021; Hajela et al. 2019).

For the top-hat jet, we observe a very good agreement between our, *PyBlastAfterglow** generated light curves and those produced by *afterglowpy* at early and late times for both on-axis and off-axis observers. This is expected as we employ similar jet discretization and EATS integrators. The remaining degree of differ-

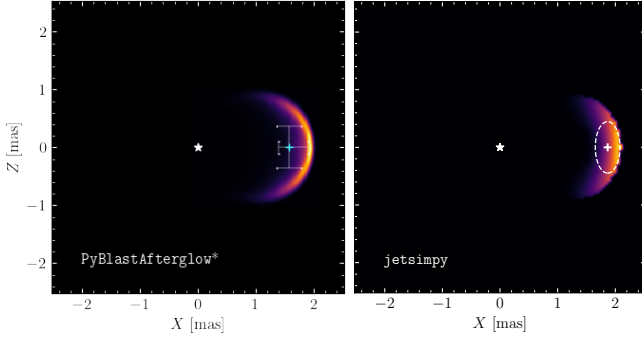


Figure 18. Comparison between the sky maps computed with `PyBlastAfterglow*` (left), `jetsimpy` (right) for the jet with Gaussian lateral structure, (same as in lower panel of Fig. 17), but observed at an angle $\theta_{\text{obs}} = 0.38$ rad., $t_{\text{obs}} = 75$ days. at the frequency, $\nu_{\text{obs}} = 10^9$ Hz. In both cases the specific intensity is shown in range 0.01 – 1 of the maximum. Cyan or white “+” marker indicate the location of the image flux centroid, while white error bars or white oval indicate the image size.

ence, especially at $\nu_{\text{obs}} = 10^9$ Hz, stems from the different treatment of γ_m and synchrotron critical frequencies. At earlier times the disagreement between our light curves observed off-axis and those produced by `jetsimpy` arises from different treatments of the jet edge. In `PyBlastAfterglow` and in `afterglowpy`, a jet has a sharp edge determined by θ_w . Meanwhile, in `jetsimpy`, shallow wings start to emerge shortly after the beginning of deceleration (see Fig. 3 in Wang et al. (2024)).

For the Gaussian jet the agreement between `jetsimpy` and `PyBlastAfterglow*` light curves is significantly better. However, the absence of the coasting phase in `afterglowpy` makes the light curve produced with that code qualitatively different from others.

In addition to light curves, we also compare sky maps computed with our code and with `jetsimpy`. The simulation for comparison is performed using Gaussian structure and the result is shown in Fig. 18. In both cases, additional Gaussian smoothing was applied to the sky map produced by afterglow codes. The figure shows that there is a small difference in sky map topography as well as in the position of the flux centroid. Notably, the latter is still small enough to be within the sky map image size, and thus may not affect inferences from a spatially unresolved source. These differences stem primarily from very different modeling of structured ejecta, – 2D BW versus a set of independent 1D BWs – and are thus expected.

Overall, we conclude that while there are differences between all three GRB afterglow codes considered here, arguably, they lie within expected ranges taking into account different physics input and numerical implementation of key physics inputs in these codes.

4.3 VHE spectrum comparison

As neither of the aforementioned codes includes SSC, we turn to the literature for comparison of VHE emission. Specifically, we consider a simplified spherically-symmetric, 1-zone afterglow model developed and tested by Menegazzi et al. (in prep.), as well as analytical BPLs spectra derived by Sari et al. (1998); Sari & Esin (2001). The result of the comparison, for the top-hat jet spectrum computed at 10^4 s. is shown in Fig. 19. The figure is made to be similar to

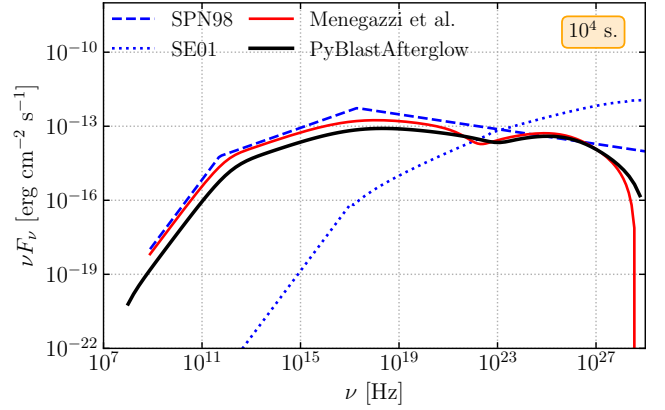


Figure 19. Comparison between spectrum produced by `PyBlastAfterglow` (black line) spectrum produced by a simplified reference code (red line) and analytic spectrum (blue lines). The comparison is performed for a top-hat jet with the following model parameters: $d_L = 2.10^{28}$ cm, $Z = 1$, $n_{\text{ism}} = 1$ cm⁻³, $E_{\text{iso}} = 2 \times 10^{52}$ ergs, $\Gamma_0 = 400$, $\theta_c = \theta_w = \pi/2$ rad., $\epsilon_e = 0.05$, $\epsilon_b = 5 \times 10^{-4}$ and $p = 2.3$. The spectrum is computed for $\theta_{\text{obs}} = 0$ rad. and $t_{\text{obs}} = 10^4$ s.

Fig. 5 from Miceli & Nava (2022) where the authors verified their SSC model.

Menegazzi et al. (in prep.) code employs a simplified analytic formulation of the spherical BW dynamics – a smoothly-connected BPL for the BW LF. Timesteps for the evolution are set according to Courant-Friedrichs-Lewy condition and thus are used directly in the implicit scheme for electron distribution evolution (Chang & Cooper 1970; Ghisellini et al. 2000). Note, in `PyBlastAfterglow`, by default, a sub-stepping procedure is used to increase computational efficiency (see Sec. 2.5). Numerically, the scheme implemented Synchrotron emission is computed using original formulation with Bessel functions, Eq. (64), while the SSC emission is computed following Miceli & Nava (2022). The code computes afterglow light curves and spectra without the EATS integrator.

As Fig. 19 shows, there is an overall good agreement between our spectra and the one computed by Menegazzi et al. (in prep.). The difference in the synchrotron spectrum stems from the different treatments of synchrotron emissivity, BW dynamics, and the calculation of the observed emission. Meanwhile, we observe a good agreement between our models in terms of high-energy SSC emission as we use the same formulation for SSC comoving emissivity. The large deviation between our SSC spectra and SE01 is due to the Klein-Nishina effect suppressing SSC emission at high energies.

5 APPLICATION TO OBSERVED GRBs

In this work we opt not to perform any parameter inference studies and leave them to dedicated future works employing surrogate models that will make Bayesian inference feasible. However, for completeness, we provide examples on how the code can be applied to observed GRBs.

In Table 1 model parameters required for modeling GRB afterglows with FS are shown. Overall, there are 11 free parameters, 3 for microphysics, 4 environmental and 4 that describe GRB jet structure. If the RS is included, the number of microphysics parameters doubles, as each parameter for the FS has a counterpart in RS. In

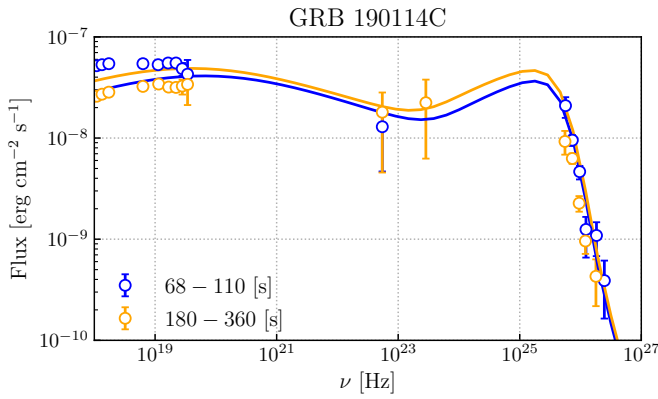


Figure 20. GRB 190114C SED from soft X-rays to 1 TeV in two different time intervals. Solid lines correspond to the model from the pre-computed grid that fits the data best (lowest mean-squared-error; see text). Observational data is adopted from (Acciari et al. 2019b).

Parameter	description
Microphysics	
$\epsilon_e; fs$	fraction of internal energy deposited in electrons
$\epsilon_b; fs$	fraction of internal energy deposited in magnetic fields
p_{fs}	electron distribution slope
Environment	
n_{ISM}	ISM number density
θ_{obs}	observer angle
d_L	luminosity distance to the source
Z	source redshift
Structure	
$E_{iso; c}$	“isotropic equivalent” kinetic energy
$\Gamma_{0; c}$	LF
θ_w	wings half-opening angle
θ_c	core half-opening angle

Table 1. List of parameters used in the paper and corresponding descriptions.

addition, t_{prompt} needs to be set that describes the duration of the GRB shell ejection.

In this section we focus on the GRB afterglows considering FS only. Observational data for GRBs with signatures of the RS is more complex and requires a dedicated study.

Furthermore, for simplicity, we focus on two jet structures: top-hat and the Gaussian, even though `PyBlastAfterglow` can be used with an arbitrary GRB ejecta structure. Notably, for the top-hat jet, $\theta_w = \theta_c$, as there are no wings in the top-hat jet, and thus, the number of free parameters is reduced to 10.

5.1 VHE of GRB 190114C

One of the key motivations behind developing `PyBlastAfterglow` is studying the VHE part of observed GRB spectra. GRB 190114C is a natural choice for us to apply our model to. VHE emission from this GRB was observed by MAGIC (Acciari et al. 2019a). Their figure 3 shows two time integrated spectra for 68 – 110 s and 110 – 180 s, covering the range from X-ray to gamma-rays. VHE from this burst is generally attributed to SSC emission generated during the afterglow phase (Nava 2021).

As we are interested in approximate modeling of this afterglow,

Parameter	Values for the grid search	Result
Microphysics		
$\epsilon_e; fs$	[0.1, 0.01, 0.001]	0.01
$\epsilon_b; fs$	[0.01, 0.001, 10^{-4} , 10^{-5}]	10^{-5}
p_{fs}	[2.2, 2.4, 2.6, 2.8]	2.6
Environment		
n_{ISM}	[1, 0.5, 0.1, 0.05, 10^{-2} , 10^{-3}] cm^{-3}	$0.5 cm^{-3}$
θ_{obs}	0 deg.	
d_L	$2.3 \times 10^9 pc$	
Z	0.4245	
Structure		
$E_{iso; c}$	[10^{51} , 10^{52} , 10^{53} , 10^{54} , 10^{55}] erg,	10^{55} erg
$\Gamma_{0; c}$	[100, 300, 600, 1000]	600
θ_c	[5, 10, 15, 20] deg.	15 deg.

Table 2. Values for the model parameters for the GRB 190114C grid search.

we employ a grid search approach, where we perform a large number of GRB afterglow simulations and then select the one that fits the observational data the best. Values for the parameter grid are reported in Table 2. For simplicity, in this case, we fixed the observational angle and the distance to the source using values from Melandri et al. (2022).

In total, we performed 23040 runs using 1344 CPU hours. For each simulation, we compute time-integrated spectra for 68 – 110 s and 110 – 180 s time windows and compare them with the observations using root-mean-square deviation as an error measure. In Fig 20, we show the spectra from the run with the lowest error. Parameter values are reported in the last column in Table 2. Notably, they are broadly consistent with what was previously inferred for this GRB (Wang et al. 2019; Asano et al. 2020; Joshi & Razzaque 2021; Derishev & Piran 2021; Miceli & Nava 2022). For more details regarding different parameter inferences for this GRB, see (Derishev & Piran 2021) and refs20240925 therein.

As expected, a low $\epsilon_b; fs$ is required to get sufficiently bright SSC emission to explain MAGIC observations. Other parameters, however, are subjected to degeneracies and in order to get a more precise fit, a larger parameter grid or a Markov chain Monte Carlo simulation for Bayesian inference is required. We leave this to future works.

5.2 Structured jet of GRB170817A

Another GRB that we consider is GRB170817A. The unusually shallow slope of its afterglow’s light curve (LC) prior to the peak is generally believed to be due to jet lateral structure and observational angle lying outside the code of the jet (*e.g.* Hajela et al. 2019).

GRB170817A has the largest amount of observational data collected for it including high cadence broad-band spectra and multi-epoch sky maps (Hajela et al. 2020; Mooley et al. 2022). Such a large amount of observational data should, in principle, allow for tight constraints on model parameters. However, a model of a structured jet observed off-axis has a large number of free parameters and significant degeneracies between them (Ryan et al. 2020). Specifically, modeling the afterglow of such a jet with `PyBlastAfterglow` requires setting all the Table 1 as free. At the same time, each simulation becomes significantly more computationally expensive as jet structure is modeled by discretizing the jet into a set (~ 20) BWs each of which represents a top-hat jet that needs to be evolved. Moreover, computing multi-frequency LCs and sky maps adds to the simulation cost. With the present configura-

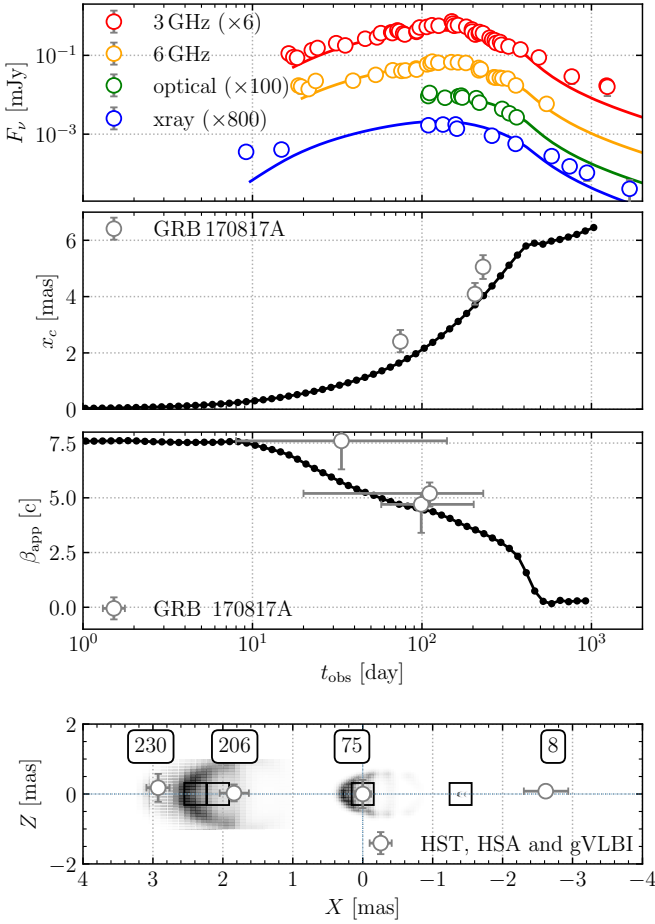


Figure 21. GRB170817A afterglow LCs (*top panel*) and sky map properties (*last three panels*) (see text for the details on the data used). *The second panel* shows the position of the apparent proper motion of GRB170817A flux centroid, x_c , and the evolution of the x_c from simulation with black line. *The third panel* shows the apparent velocity, β_{app} for three time-intervals for GRB170817A and the evolution of β_{app} from the simulation. *The last panel* shows the positions of the flux centroid at 4 epochs labeled by the number of days since burst and the sky maps computed at these epochs as well x_c (displayed with square markers). Positions are normalized using 75 days observation as a reference (having offset of 0). The PyBlastAfterglow simulation parameters are: $n_{\text{ISM}} = 0.025 \text{ cm}^{-3}$, $E_{\text{iso};c} = 1.26 \times 10^{54} \text{ erg}$, $\Gamma_{0;c} = 300$, $\theta_c = 3.5 \text{ deg.}$, $\theta_w = 25 \text{ deg.}$, $p_{\text{fs}} = 2.1$, $\epsilon_{e;fs} = 3.8 \times 10^{-3}$, $\epsilon_{b;fs} = 9.5 \times 10^{-5}$, $\theta_{\text{obs}} = 20.8 \text{ deg.}$

tion of PyBlastAfterglow each run requires approximately 1 CPU/hour. In light of this, as we aim to demonstrate the code applicability instead of performing parameter inference, we opt for a different strategy here. Instead of performing a grid parameter search, we start with parameter values derived by in a successful parameter inference run in Ryan et al. (2020) and then refine the values with a small number of fine-tuning runs. The result is shown in Fig. 21.

We use the following observational data to compare our model with. Radio band data was obtained by Karl G. Jansky Very Large Array Very Large Array (VLA) (Hallinan et al. 2017; Alexander et al. 2018; Margutti et al. 2017; Mooley et al. 2018a), Australia Telescope Compact Array (Hallinan et al. 2017; Dobie et al. 2018; Mooley et al. 2018c,b; Makhathini et al. 2021), the Giant Metrewave Radio Telescope (Resmi et al. 2018; Mooley et al. 2018b), the enhanced Multi Element Remotely Linked Interferometer Net-

work (Makhathini et al. 2021), Very Long Baseline Array (Ghirlanda et al. 2019), and the MeerKAT telescope (Mooley et al. 2018b; Makhathini et al. 2021). The optical data is from Hubble Space Telescope (Lyman et al. 2018; Fong et al. 2019; Lamb et al. 2019b). The X-ray band data is from XMM-Newton (D’Avanzo et al. 2018; Piro et al. 2019) and Chandra (Troja et al. 2017, 2018; Hajela et al. 2019; Troja et al. 2020, 2022; O’Connor & Troja 2022).

For the sky map data we employ Very-long-baseline interferometry (VLBI) observations at 8, 75, 206 and 230 days after the burst (Mooley et al. 2022) comparing the positions of the flux centroid and the apparent proper motion (second and third panels in the figure, respectively). The latter is computed as $\beta_{\text{app}} = \Delta x_c / \Delta t_{\text{obs}} / c$ for three time intervals, 8 – 75, 8 – 206, and 8 – 230 days. In the last panel of the figure, the position at 8 days is plotted relative to the radio VLBI positions at 75 and 230 days measured with the High Sensitivity Array (HSA) and 206 days measurement made with 32-telescope global VLBI (gVLBI) array. with 75 days VLBI measurement used with offsets 0 (Mooley et al. 2018b). In the last panel of the figure we also display actual sky maps from our simulation using gray-scale colormap.

Fig. 21 shows that PyBlastAfterglow is capable of reproducing the main features of GRB170817A including the shallow slope of the LC before the peak, with overall good quantitative and qualitative agreements between the observations and the data with log-root-means-squared-error of 1.41 that is given primarily due to our model underestimating fluxes in X-ray at early and late times. This can be improved by performing a dedicated parameter inference study. Similarly, sky map properties show qualitative and a reasonable quantitative agreement with observations when comparing apparent proper motion and apparent velocity. Slight underestimation in both that results in root-mean-squared-error of 0.77 and 1.19 respectively can be improved by consider a more narrow jet that is observed further off-axis. The last panel in the figure corroborates this observation.

6 DISCUSSION AND CONCLUSION

GRBs are ubiquitous in nature. They originate from the most energetic and the most complex events in the Universe: supernovae and mergers of compact object. Their understanding shapes our comprehension of cosmology, jet and plasma physics, properties of matter at extreme densities and gravity in the strong field regime.

While prompt emission in GRBs is not yet sufficiently well understood to be employed in parameter inference studies, the afterglow phase is. There are numerous theoretical frameworks and numerical models that provide a connection between underlying physics and observables. Key physical processes include relativistic MHD, shock microphysics, non-thermal radiation processes and radiation transport, while the observables include light curves, spectra and sky maps – images of the brightest parts of the jet on the phrase plane of the sky (tangent to the celestial sphere).

From numerous GRB afterglow studies it is deduced that this non-thermal, predominately synchrotron emission originates at collisionless shocks that form when relativistic ejecta collides with the surrounding matter, *e.g.*, the ISM. The success and relative simplicity of this picture has led to the development of a several analytical, semi-analytical and, to a lesser extend, numerical afterglow models capable of reproducing the key observables.

Notably, due to a large number of observables (*e.g.*, multi-epoch, spectra and sky maps), large number of free model parameters and unavoidable degeneracies between them analytical or semi-

analytical models became the standard due to their relative simplicity and computational efficiency. Such models allow for Bayesian inference studies and parameter grid searches. Notably, certain physics components like RS and SSC emission are notoriously difficult to implement analytically and thus are rarely included in parameter inference studies.

Meanwhile, extending existing models to account for the missing physics is highly non-trivial and generally requires re-derivation of the underlying theoretical framework and re-implementation of the numerics. On the other hand, models that are constructed from the ground up to include as much physics as possible, *e.g.*, hydrodynamic or MHD jet models with particle distribution evolution and radiation transport are prohibitively computationally expensive.

In this work we present a GRB afterglow model `PyBlastAfterglow` that attempts to have a balance between the two approaches. The dynamics of the jet is treated under the piece-wise, thin-shell approximation where a jet is divided into non-interacting angular segments each of which is represented by a singular layer of matter – a fluid element, a BW – that includes forward and reverse shocks and a contact discontinuity between them. Jet lateral spreading is accounted for with an analytical prescription based on local sound speed. This is conceptually similar to existing semi-analytical models such as `afterglowpy`. However, contrary to most models, electron distribution evolution is treated numerically by solving continuity equation that includes injection of freshly shocked particles and cooling via synchrotron, adiabatic and SSC processes. Radiation emission and absorption processes include synchrotron, SSC, SSA, PP and EBL absorption. Observables are computed via numerical EATS integration from each angular layer and combining the result.

Notably, such models have been presented in the literature before. However, to the best of our knowledge, there is no open-sourced or well-documented model. At present the code allows for GRB and kilonova (kN) afterglow modeling, with the latter discussed in Nedora et al. (2022, 2023) and Nedora et al. (2024, in prep.). `PyBlastAfterglow`, is designed to be modular and easily extendable. For instance, BW dynamics can be modified to include effects of (i) non-uniform or pre-accelerated ambient medium (Beloborodov 2005; Nava et al. 2013), (ii) late-time energy injection from a magnetar (Metzger et al. 2011; Gompertz et al. 2014; Ren et al. 2019); spectrum of injected electrons can be further augmented to include more realistic profiles, motivated by PIC simulations (Vurm & Metzger 2021; Warren et al. 2022); proton distribution evolution (Zhang et al. 2023), diffusion and escape terms can also be added to produce a spectrum of cosmic rays (Das & Razaque 2023; Biehl et al. 2018); additional seed photons (*e.g.*, from a kilonova or a supernova) can be included in IC spectrum computation (Linial & Sari 2019; Zhang et al. 2020).

Notably, the code is not fast enough to perform direct Bayesian inference runs, especially for laterally structured jets with FS-RS BWs numerical electron, synchrotron and SSC spectra evolution. However, it is still possible to perform large set of simulation for a grid of values of model parameters and then train a surrogate model for fast inference. Modern machine learning techniques, such as conditional variational auto-encoders and generative adversarial neural networks can be trained on even marginally coarse grids of data due to their generative nature. Such surrogate models would allow for parameter inference runs that are significantly faster than any existing semi-analytic GRB afterglow models and would have physics lacking in those. We aim to explore this possibility in future works.

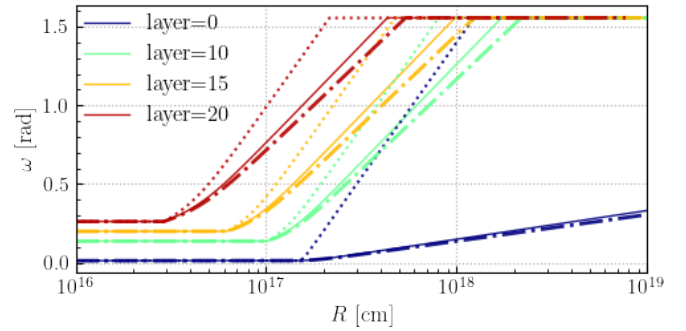


Figure A1. Comparison between different lateral spreading prescriptions for several layers of a Gaussian jet. Solid line corresponds to Eq. (32) implemented in `PyBlastAfterglow` as a default option. Dashed-dotted line corresponds to the prescription where “TM” EOS is assumed, and dotted line corresponds to the prescription without structure-related terms (see text).

ACKNOWLEDGEMENTS

We thank Kohta Murase for providing us with comments regarding the manuscript. This work was partially funded by the European Union (ERC, SMARt, 101076369). Views and opinions expressed are those of the authors only and do not necessarily reflect those of the European Union or the European Research Council. Neither the European Union nor the granting authority can be held responsible for them. The simulations were performed on the national supercomputer HPE Apollo Hawk at the High Performance Computing (HPC) Center Stuttgart (HLRS) under the grant number GWanalysis/44189 and on the GCS Supercomputer SuperMUC at Leibniz Supercomputing Centre (LRZ) [project pn29ba].

We thank Professor Kohta Murase for his useful comments on the manuscript.

Software: We are grateful to the countless developers contributing to open-source projects that was used in the analysis of the simulation results of this work: NumPy (Harris et al. 2020), Matplotlib (Hunter 2007), and SciPy (Virtanen et al. 2020).

DATA AVAILABILITY:

The code presented and employed in this work is open source and can be found at <https://github.com/vsevolodnedora/PyBlastAfterglowMag>. The datasets generated during and/or analyzed during the current study are available from the corresponding author on reasonable request.

APPENDIX A: LATERAL SPREADING PRESCRIPTIONS

In this section we briefly compare BW dynamics with different lateral spreading prescription. All simulations are performed using the structure and parameters of the Gaussian jet as discussed in the main text in Sec. 3.3. The result of the comparison is shown in Fig. A1.

Besides the prescription described in Sec. 2.1, (Eq. (32)) we also consider here the original formulation of (Ryan et al. 2020) where “TM” EOS from (Mignone et al. 2005) was used. In this case velocity perpendicular to the norm of the shock surface reads,

$$v_{\perp} = \frac{1}{2} \frac{\beta_{\text{sh}}}{\Gamma} \sqrt{\frac{2(\Gamma\beta)^2 + 3}{4(\Gamma\beta)^2 + 3}}, \quad (\text{A1})$$

where the shock velocity, $\beta_{\text{sh}} = 4\Gamma^2\beta/(4(\Gamma\beta)^2 + 3)$. The lateral spreading equation then becomes,

$$\frac{d\omega}{dR} = \frac{1}{2R\Gamma} \sqrt{\frac{2(\Gamma\beta)^2 + 3}{4(\Gamma\beta)^2 + 3}} \times \begin{cases} 0 & \text{if } Q_0\Gamma_{\text{sh}}\beta_{\text{sh}}\omega_c < 1 \\ \frac{Q(1-Q_0\omega_c\Gamma_{\text{sh}}\beta_{\text{sh}})}{Q-Q_0} & \text{if } Q\Gamma_{\text{sh}}\beta_{\text{sh}}\omega_c > 1 \\ 1 & \text{otherwise} \end{cases}, \quad (\text{A2})$$

$$\times \begin{cases} \tan(\omega_0/2)/\tan(\omega_c/2) & \text{if } \omega_0 < \omega_c \\ 1 & \text{otherwise} \end{cases}$$

where Q , Q_0 and ω_c are set as before (see Eq. (32)).

The BW dynamics computed with this equation is shown with dashed-dotted line in the figure. It deviates from the dynamics obtained with the default prescription only slightly and for BWs with $\Gamma_0 \ll 100$. This degree of mismatch is expected as we employ different EOSs.

Finally, we also compute spreading with a much simpler model, where the tangential velocity is still approximated with the sound speed but no additional constraints are applied (e.g., geometry and momentum constraints in Eq. (32)). The simplified equation then reads,

$$\frac{d\omega}{dR} = \frac{c_s}{R\Gamma\beta c}. \quad (\text{A3})$$

The BW dynamics computed using Eq. (A3) corresponds to dotted line in the figure. As expected, the rate of lateral expansion for all layers of the jet, irrespective of their position with the jet, are similar as we fix the minimum $\Gamma\beta$ at which spreading can begin (see main text). This results in a large overestimation of the spreading rate for the core of the jet (layer=0). Overall this example highlights the importance of structure-aware lateral spreading prescriptions in semi-analytical modeling of jet dynamics.

APPENDIX B: SKY MAP COMPARISON

In (Nedora et al. 2022) we presented a different method to compute GRB afterglow properties. The main difference between that method and the one discussed in the main text is the jet discretization. While in the main text we discussed the model that approximates a jet as a series of overlapping BWs with progressively increasing half-opening angles (see Sec. 2.5.3) in the aforementioned study we discretized a jet into a set of non-overlapping $(\theta-\phi)$ -cells of equal solid angle, each of which had a BW assigned to it. In that method, each hemisphere is split into $k = \{1, 2, \dots, n-1\}$ rings centered on the symmetry axis plus the single central spherical cap, $k = 0$ with the opening angle $\theta_{l=1}$ (Beckers & Beckers 2012). In order to achieve equal solid angle size per cell, each hemisphere was discretized uniformly in $\cos(\theta_l)$ so that angle between two concentric circles on the sphere was $\theta_{l=i} = 2\sin^{-1}(\sqrt{k/n}\sin(\theta_w/2))$, where θ_w is the initial opening angle of the jet. Each layer consisted of $2i+1$ $(\theta-\phi)$ -cells bounded by $\phi_{ij} = 2\pi j/(2i+1)$ where $j = \{0, 1, 2, \dots, i\}$. In total the jet was discretized into $\sum_{i=0}^{n-1} (2i+1)$ cells, for each of which an independent BW was evolved. We label this jet discretization method as PW while the method discussed in the main text we label as A. Since both of them are incorporated in PyBlastAfterglow it is natural to perform a comparison.

Here we perform two afterglow simulations for top-hat jet and two for the Gaussian jet with the same structure and microphysics properties as discussed in Sec. 3, but setting observer angle as

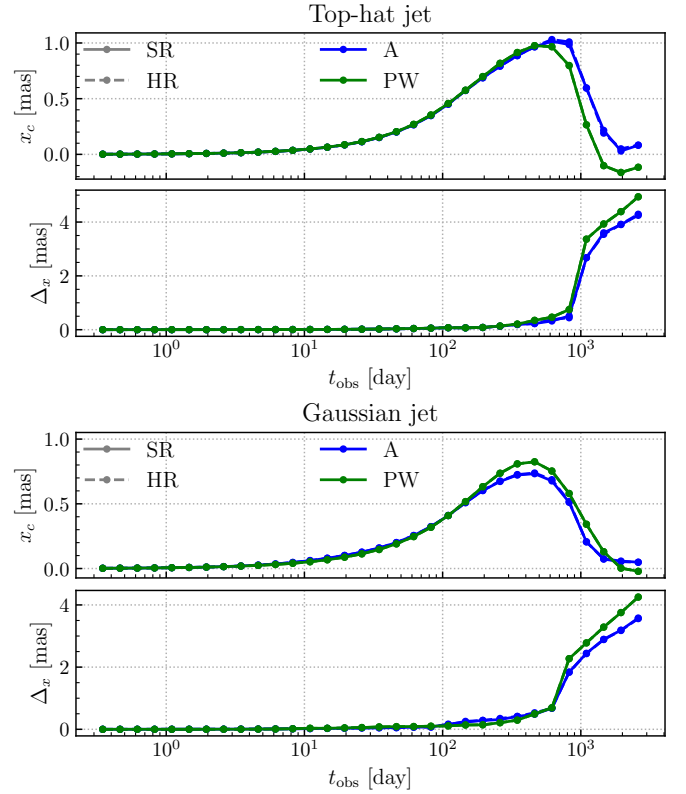


Figure B1. Comparison of sky-map properties evolution for top-hat jet *top pair of panels* and Gaussian jet *bottom pair of panels*. For both cases the evolution of sky map flux centroid position x_c (*top sub-panel*) and image size, Δ_x (*bottom sub-panel*) are shown. PW and A stand for different jet discretization (see text).

$\theta_{\text{obs}} = \pi/4$ rad. Only FS is considered here and synchrotron emission is computed analytically (i.e. using PyBlastAfterglow* configuration of the code discussed in Sec. 4).

In A method, a top-hat jet is approximated with a single BW that has initial half-opening angle equal to that of the jet. In PW method, however, $n \gg 1$ BWs are required so that the jet angular extend is properly covered with $(\theta-\phi)$ -cells. Importantly, in A method we also need to have to discretized the hemisphere into cells to calculate sky map, but this is done after BW evolution. There we adaptively resize the spherical grid until the required resolution is reached (See Sec. 2.5.5) and the grid resolution enters as a free parameter. In the case of a Gaussian jet, a certain number of angular layers (i.e., BWs) needs to be set for both methods, and thus, it is a natural parameter describing resolution.

In Fig. B1 we show a comparison of evolution of sky map properties computed with A method (blue color) and PW method (green color). We consider two resolution options labeled SR and HR, where SR stands for the resolution used in the main text and HR is two times higher resolution. Overall we observe a very good agreement in sky map flux centroid position x_c and its size Δ_x between two simulations at early time. At the point where x_c reaches maximum, emission from the counter-jet becomes comparable to that from the principle jet (see Sec. 3). Around this point, the BW lateral spreading plays a key role in determining sky map properties. BWs in the simulation with PW method are less energetic and lateral spreading there starts much earlier (for the top-hat jet) and proceeds faster. In the case of the Gaussian jet, there are slow BW in both

cases, A and P_W and the x_c reaches maximum at the same time. Image size Δ_x grows faster and to larger values in the simulation with P_W method as lateral spreading is enhanced. Overall, however, we highlight that sky map properties evolution is qualitatively the same in simulations with different discretization methods and quantitative agreement is good.

REFERENCES

- Abbott B. P., et al., 2017a, *Phys. Rev. Lett.*, 119, 161101
 Abbott B. P., et al., 2017b, *Astrophys. J. Lett.*, 848, L13
 Abdalla H., et al., 2019, *Nature*, 575, 464
 Abdalla H., et al., 2021, *Science*, 372, 1081
 Acciari V. A., et al., 2019a, *Nature*, 575, 455
 Acciari V. A., et al., 2019b, *Nature*, 575, 459
 Aharonian F. A., Kelner S. R., Prosekin A. Y., 2010, *Physical Review D*, 82, 043002
 Ai S., Zhang B., 2021, *Mon. Not. Roy. Astron. Soc.*, 507, 1788
 Ai S., Zhang B., Zhu Z., 2022, *Mon. Not. Roy. Astron. Soc.*, 516, 2614
 Alexander K. D., et al., 2017, *Astrophys. J.*, 848, L21
 Alexander K., et al., 2018, *Astrophys. J.*, 863, L18
 Arcavi I., et al., 2017, *Nature*, 551, 64
 Asano K., Murase K., Toma K., 2020, *Astrophys. J.*, 905, 105
 Ayache E. H., van Eerten H. J., Daigne F., 2020, *Mon. Not. Roy. Astron. Soc.*, 495, 2979
 Bai X.-N., Caprioli D., Sironi L., Spitkovsky A., 2015, *Astrophys. J.*, 809, 55
 Barniol Duran R., Kumar P., 2011, *Mon. Not. Roy. Astron. Soc.*, 417, 1584
 Becerra R. L., et al., 2019, *Astrophys. J.*, 881, 12
 Beckers B., Beckers P., 2012, *Computational Geometry*, 45, 275
 Beloborodov A. M., 2005, *Astrophys. J.*, 627, 346
 Beloborodov A. M., Uhm Z. L., 2006, *Astrophys. J. Lett.*, 651, L1
 Beniamini P., Nava L., Piran T., 2016, *Mon. Not. Roy. Astron. Soc.*, 461, 51
 Bernardini M. G., Margutti R., Chincarini G., Guidorzi C., Mao J., 2011, *Astronomy & Astrophysics*, 526, A27
 Bernardini M. G., Margutti R., Mao J., Zaninoni E., Chincarini G., 2012, *Astronomy & Astrophysics*, 539, A3
 Biehl D., Boncioli D., Fedynitch A., Winter W., 2018, *Astron. Astrophys.*, 611, A101
 Blandford R. D., McKee C. F., 1976, *Physics of Fluids*, 19, 1130
 Blumenthal G. R., Gould R. J., 1970, *Rev. Mod. Phys.*, 42, 237
 Bosnjak Z., Daigne F., Dubus G., 2009, *Astron. Astrophys.*, 498, 677
 Bulla M., Coughlin M. W., Dhawan S., Dietrich T., 2022, *Universe*, 8, 289
 Cao Z., et al., 2023, *Sci. Adv.*, 9, adj2778
 Cerdá-Durán P., Obergaulinger M., Aloy M. A., Font J. A., Müller E., 2011, in *Journal of Physics Conference Series*. p. 012079, doi:10.1088/1742-6596/314/1/012079
 Chandrasekhar S., 1943, *Rev. Mod. Phys.*, 15, 1
 Chang J. S., Cooper G., 1970, *Journal of Computational Physics*, 6, 1
 Chen Q., Liu X.-W., 2021, *Mon. Not. Roy. Astron. Soc.*, 504, 1759
 Chevalier R. A., Li Z. Y., 1999, *Astrophys. J. Lett.*, 520, L29
 Chiaberge M., Ghisellini G., 1999, *Mon. Not. Roy. Astron. Soc.*, 306, 551
 Chiang J., Dermer C. D., 1999, *Astrophys. J.*, 512, 699
 Chincarini G., et al., 2010, *Monthly Notices of the Royal Astronomical Society*, 406, 2113
 Coppi P. S., Blandford R. D., 1990, *Mon. Not. Roy. Astron. Soc.*, 245, 453
 Coulter D. A., et al., 2017, *Science*, 358, 1556
 Crusius A., Schlickeiser R., 1986, *Astronomy & Astrophysics*, 164, L16
 D'Avanzo P., et al., 2018, *Astron. Astrophys.*, 613, L1
 Daigne F., Mochkovitch R., 2000, *Astron. Astrophys.*, 358, 1157
 Dainotti M. G., Nagataki S., Maeda K., Postnikov S., Pian E., 2017, *Astron. Astrophys.*, 600, A98
 Das S., Razaque S., 2023, *Astron. Astrophys.*, 670, L12
 Derishev E., Piran T., 2021, *Astrophys. J.*, 923, 135
 Dermer C. D., Chiang J., 1998, *New Astron.*, 3, 157
 Dermer C. D., Humi M., 2001, *Astrophys. J.*, 556, 479
 Dermer C. D., Chiang J., Mitman K. E., 2000, *Astrophys. J.*, 537, 785
 Dietrich T., Coughlin M. W., Pang P. T. H., Bulla M., Heinzl J., Issa L., Tews I., Antier S., 2020, *Science*, 370, 1450
 Dobie D., et al., 2018, *Astrophys. J. Lett.*, 858, L15
 Domínguez A., et al., 2011, *Mon. Not. Roy. Astron. Soc.*, 410, 2556
 Drout M. R., et al., 2017, *Science*, 358, 1570
 Duffell P. C., MacFadyen A. I., 2013, *Astrophys. J.*, 775, 87
 Duffell P. C., Quataert E., Kasen D., Klion H., 2018, *Astrophys. J.*, 866, 3
 Duque R., Beniamini P., Daigne F., Mochkovitch R., 2022, *Mon. Not. Roy. Astron. Soc.*, 513, 951
 Eichler D., Waxman E., 2005, *Astrophys. J.*, 627, 861
 Evans P. A., et al., 2017, *Science*, 358, 1565
 Fan Y.-H., Piran T., 2006, *Mon. Not. Roy. Astron. Soc.*, 369, 197
 Fan Y. Z., Piran T., Narayan R., Wei D.-M., Piran T., Narayan R., Wei D. M., 2008a, *Mon. Not. Roy. Astron. Soc.*, 384, 1483
 Fan Y.-Z., Piran T., Narayan R., Wei D.-M., 2008b, *Mon. Not. Roy. Astron. Soc.*, 384, 1483
 Fernández J. J., Kobayashi S., Lamb G. P., 2021, *Mon. Not. Roy. Astron. Soc.*, 509, 395
 Fong W., et al., 2017, *Astrophys. J. Lett.*, 848, L23
 Fong W.-f., et al., 2019, *Astrophys. J. Lett.*, 883, L1
 Fraija N., Dainotti M. G., Levine D., Betancourt Kamenetskaia B., Galvan-Gamez A., 2023, *Astrophys. J.*, 958, 126
 Franceschini A., Rodighiero G., 2017, *Astron. Astrophys.*, 603, A34
 Gao H., Mészáros P., 2015, *Adv. Astron.*, 2015, 192383
 Gao H., Lei W.-H., Wu X.-F., Zhang B., 2013, *Monthly Notices of the Royal Astronomical Society*, 435, 2520
 Gao H.-X., Geng J.-J., Sun T.-R., Li L., Huang Y.-F., Wu X.-F., 2023
 Geng J.-J., Huang Y.-F., Wu X.-F., Zhang B., Zong H.-S., 2018, *Astrophys. J. Suppl.*, 234, 3
 Ghirlanda G., et al., 2019, *Science*, 363, 968
 Ghisellini G., Svensson R., 1991, *Mon. Not. Roy. Astron. Soc.*, 252, 313
 Ghisellini G., Guilbert P. W., Svensson R., 1988, *The Astrophysical Journal Letters*, 334, L5
 Ghisellini G., Haardt F., Svensson R., 1998, *Mon. Not. Roy. Astron. Soc.*, 297, 348
 Ghisellini G., Celotti A., Lazzati D., 2000, *Mon. Not. Roy. Astron. Soc.*, 313, 1
 Giannios D., Spruit H. C., 2005, *Astron. Astrophys.*, 430, 1
 Giannios D., Mimica P., Aloy M. A., 2008, *Astron. Astrophys.*, 478, 747
 Gill R., Granot J., 2018, *Mon. Not. Roy. Astron. Soc.*, 478, 4128
 Gilmore R. C., Somerville R. S., Primack J. R., Domínguez A., 2012, *Mon. Not. Roy. Astron. Soc.*, 422, 3189
 Gompertz B. P., O'Brien P. T., Wynn G. A., 2014, *Mon. Not. Roy. Astron. Soc.*, 438, 240
 Gompertz B. P., Fruchter A. S., Pe'er A., 2018, *Astrophys. J.*, 866, 162
 Granot J., Piran T., 2012, *Monthly Notices of the Royal Astronomical Society*, 421, 570
 Granot J., Sari R., 2002, *Astrophys. J.*, 568, 820
 Granot J., Piran T., Sari R., 1999, *Astrophys. J.*, 527, 236
 Granot J., Cohen-Tanugi J., do Couto e Silva E., 2008, *Astrophys. J.*, 677, 92
 Guarini E., Tamborra I., Bégué D., Pitik T., Greiner J., 2022, *JCAP*, 06, 034
 Hairer E., Norsett S., Wanner G., 1993, *Solving Ordinary Differential Equations I: Nonstiff Problems*. Vol. 8, doi:10.1007/978-3-540-78862-1,
 Hajela A., et al., 2019, *Astrophys. J. Lett.*, 886, L17
 Hajela A., et al., 2020, *GRB Coordinates Network*, 29055, 1
 Hallinan G., et al., 2017, *Science*, 358, 1579
 Harris C. R., et al., 2020, *Nature*, 585, 357
 He H.-N., Wang X.-Y., Yu Y.-W., Mészáros P., 2009, *Astrophys. J.*, 706, 1152
 He H.-N., Wu X.-F., Toma K., Wang X.-Y., Mészáros P., 2011, *Astrophys. J.*, 733, 22
 Huang Y., 2022, *Astrophys. J.*, 931, 150
 Huang Y., Dai Z., Lu T., 1999, *Mon. Not. Roy. Astron. Soc.*, 309, 513
 Huang Y., Dai Z., Lu T., 2000a, *Mon. Not. Roy. Astron. Soc.*, 316, 943
 Huang Y., Gou L., Dai Z., Lu T., 2000b, *Astrophys. J.*, 543, 90
 Huang X.-L., Wang Z.-R., Liu R.-Y., Wang X.-Y., Liang E.-W., 2021, *Astrophys. J.*, 908, 225
 Hunter J. D., 2007, *Computing in Science & Engineering*, 9, 90

- Jamil, O. and Böttcher, M. 2012, *Astrophys. J.*, 759, 45
- Johannesson G., Björnsson G., Gudmundsson E. H., 2006, *Astrophys. J.*, 647, 1238
- Jones F. C., 1968, *Phys. Rev.*, 167, 1159
- Joshi J. C., Razaque S., 2021, *Mon. Not. Roy. Astron. Soc.*, 505, 1718
- Kasliwal M. M., et al., 2017, *Science*, 358, 1559
- Kino M., Takahara F., Kusunose M., 2002, *Astrophys. J.*, 564, 97
- Kirk J. G., Duffy P., 1999, *J. Phys. G*, 25, R163
- Kobayashi S., Sari R., 2000, *Astrophys. J.*, 542, 819
- Kobayashi S., Zhang B., 2003, *Astrophys. J.*, 597, 455
- Kumar P., Barniol Duran R., 2009, *Monthly Notices of the Royal Astronomical Society*, 400, L75
- Kumar P., Barniol Duran R., 2010, *Mon. Not. Roy. Astron. Soc.*, 409, 226
- Kumar P., Granot J., 2003, *Astrophys. J.*, 591, 1075
- Kumar P., Zhang B., 2014, *Phys. Rept.*, 561, 1
- Kumar P., Hernández R. A., Bošnjak v., Barniol Duran R., 2012, *Monthly Notices of the Royal Astronomical Society*, 427, L40
- Kunert N., et al., 2024, *Mon. Not. Roy. Astron. Soc.*, 527, 3900
- Lamb G. P., Kobayashi S., 2017, *Mon. Not. Roy. Astron. Soc.*, 472, 4953
- Lamb G. P., Mandel I., Resmi L., 2018, *Mon. Not. Roy. Astron. Soc.*, 481, 2581
- Lamb G. P., et al., 2019a, *The Astrophysical Journal*
- Lamb G. P., et al., 2019b, *Astrophys. J. Lett.*, 870, L15
- Lamb G. P., Nativi L., Rosswog S., Kann D. A., Levan A., Lundman C., Tanvir N., 2022, *Universe*, 8, 612
- Laskar T., et al., 2019, *Astrophys. J.*, 884, 121
- Lazarian A., Zhang B., Xu S., 2019, *The Astrophysical Journal*, 882, 184
- Lazzati D., Ghisellini G., 1999, *Mon. Not. Roy. Astron. Soc.*, 309, 13
- Lemoine M., Pelletier G., 2010, *Mon. Not. Roy. Astron. Soc.*, 402, 321
- Li L., et al., 2015, *Astrophys. J.*, 805, 13
- Linal I., Sari R., 2019, *Mon. Not. Roy. Astron. Soc.*, 483, 624
- Lu W., Beniamini P., McDowell A., 2020
- Lyman J. D., et al., 2018, *Nat. Astron.*, 2, 751
- Lyutikov M., 2011, *Mon. Not. Roy. Astron. Soc.*, 411, 422
- Makhathini S., et al., 2021, *Astrophys. J.*, 922, 154
- Marcowith A., Ferrand G., Grech M., Meliani Z., Plotnikov I., Walder R., 2020, *Liv. Rev. Comput. Astrophys.*, 6, 1
- Margalit B., Piran T., 2020, *Mon. Not. Roy. Astron. Soc.*, 495, 4981
- Margutti R., Bernardini G., Barniol Duran R., Guidorzi C., Shen R. F., Chincarini G., 2011, *Monthly Notices of the Royal Astronomical Society*, 410, 1064
- Margutti R., et al., 2017, *Astrophys. J.*, 848, L20
- Margutti R., et al., 2018, *Astrophys. J.*, 856, L18
- McMahon E., Kumar P., Piran T., 2006, *Mon. Not. Roy. Astron. Soc.*, 366, 575
- Medvedev M. V., Loeb A., 1999, *Astrophys. J.*, 526, 697
- Melandri A., et al., 2022, *Astron. Astrophys.*, 659, A39
- Meszáros P., Rees M. J., 1993, *Astrophys. J.*, 405, 278
- Meszáros P., Rees M. J., 1997, *Astrophys. J.*, 476, 232
- Metzger B. D., et al., 2010, *Monthly Notices of the Royal Astronomical Society*, 406, 2650
- Metzger B. D., Giannios D., Thompson T. A., Bucciantini N., Quataert E., 2011, *Mon. Not. Roy. Astron. Soc.*, 413, 2031
- Miceli D., Nava L., 2022, *Galaxies*, 10, 66
- Mignone A., Plewa T., Bodo G., 2005, *Astrophys. J. Suppl.*, 160, 199
- Mignone A., Bodo G., Vaidya B., Mattia G., 2018, *Astrophys. J.*, 859, 13
- Mooley K. P., et al., 2018a, *Nature*, 554, 207
- Mooley K. P., et al., 2018b, *Nature*, 561, 355
- Mooley K. P., et al., 2018c, *Astrophys. J. Lett.*, 868, L11
- Mooley K. P., Anderson J., Lu W., 2022, *Nature*, 610, 273
- Moss M., Lien A., Guiriec S., Cenko S. B., Sakamoto T., 2022, *The Astrophysical Journal*, 927, 157
- Murase K., Toma K., Yamazaki R., Meszaros P., 2011, *Astrophys. J.*, 732, 77
- Nakar E., Ando S., Sari R., 2009, *Astrophys. J.*, 703, 675
- Nardini M., Ghisellini G., Ghirlanda G., Tavecchio F., Firmani C., Lazzati D., 2006, *Astron. Astrophys.*, 451, 821
- Nava L., 2021, *Universe*, 7, 503
- Nava L., Sironi L., Ghisellini G., Celotti A., Ghirlanda G., 2013, *Monthly Notices of the Royal Astronomical Society*, 433, 2107
- Nedora V., Dietrich T., Shibata M., Pohl M., Menegazzi L. C., 2022, *Mon. Not. Roy. Astron. Soc.*
- Nedora V., Dietrich T., Shibata M., 2023, *Mon. Not. Roy. Astron. Soc.*, 524, 5514
- Nicholl M., et al., 2017, *Astrophys. J.*, 848, L18
- Nousek J. A., et al., 2006, *Astrophys. J.*, 642, 389
- Nynka M., Ruan J. J., Haggard D., Evans P. A., 2018, *Astrophys. J. Lett.*, 862, L19
- O'Connor B., Troja E., 2022, GRB Coordinates Network, 32065, 1
- Oganesyan G., Nava L., Ghirlanda G., Celotti A., 2017, *Astrophys. J.*, 846, 137
- Oganesyan G., Nava L., Ghirlanda G., Celotti A., 2018, *Astron. Astrophys.*, 616, A138
- Paczynski B., 1998, *Astrophys. J. Lett.*, 494, L45
- Panaitecu A., Kumar P., 2000, *Astrophys. J.*, 543, 66
- Panaitecu A., Kumar P., 2003, *AIP Conf. Proc.*, 662, 305
- Pang P. T. H., et al., 2023, *Nature Commun.*, 14, 8352
- Park J., Caprioli D., Spitkovsky A., 2015, *Phys. Rev. Lett.*, 114, 085003
- Pe'er A., 2012, *The Astrophysical Journal Letters*, 752, L8
- Pellouin C., Daigne F., 2024
- Petropoulou M., Mastichiadis A., 2009, *Astronomy & Astrophysics*, 507, 599
- Petrosian V., 1981, *The Astrophysical Journal*, 251, 727
- Pilla R. P., Loeb A., 1998, *Astrophys. J. Lett.*, 494, L167
- Piran T., 1999, *Phys. Rept.*, 314, 575
- Piro L., et al., 2019, *Mon. Not. Roy. Astron. Soc.*, 483, 1912
- Preece R. D., Briggs M. S., Malozzi R. S., Pendleton G. N., Paciesas W. S., Band D. L., 1998, *Astrophys. J. Lett.*, 506, L23
- Prince P. J., Dormand J. R., 1981, *Journal of Computational and Applied Mathematics*, 7, 67
- Ravasio M. E., Oganesyan G., Ghirlanda G., Nava L., Ghisellini G., Pescalli A., Celotti A., 2018, *Astron. Astrophys.*, 613, A16
- Rees M. J., Meszaros P., 1992, *Mon. Not. Roy. Astron. Soc.*, 258, 41
- Rees M. J., Meszaros P., 1994, *Astrophys. J. Lett.*, 430, L93
- Ren J., Lin D.-B., Zhang L.-L., Li X.-Y., Liu T., Lu R.-J., Wang X.-G., Liang E.-W., 2019, *arXiv:1905.04670*
- Resmi L., et al., 2018, *Astrophys. J.*, 867, 57
- Reville B., Kirk J. G., Duffy P., 2006, *Plasma Phys. Control. Fusion*, 48, 1741
- Rezzolla L., Zanotti O., 2013, *Relativistic Hydrodynamics*, 1 edn. Mathematics, Oxford University Press, Oxford
- Rocha da Silva G., Falceta-Gonçalves D., Kowal G., de Gouveia Dal Pino E. M., 2015, *Mon. Not. Roy. Astron. Soc.*, 446, 104
- Rossi E. M., Lazzati D., Salmonson J. D., Ghisellini G., 2004, *Mon. Not. Roy. Astron. Soc.*, 354, 86
- Ruan J. J., Nynka M., Haggard D., Kalogera V., Evans P., 2018, *Astrophys. J.*, 853, L4
- Ryan G., van Eerten H., Piro L., Troja E., 2020, *Astrophys. J.*, 896, 166
- Ryan G., van Eerten H., Troja E., Piro L., O'Connor B., Ricci R., 2023
- Rybicki G. B., Lightman A. P., 1986, *Radiative Processes in Astrophysics*
- Salafia O. S., et al., 2022, *Astrophys. J. Lett.*, 931, L19
- Sari R., Esin A. A., 2001, *Astrophys. J.*, 548, 787
- Sari R., Piran T., 1995, *The Astrophysical Journal*, 455
- Sari R., Piran T., 1999, *The Astrophysical Journal*, 520, 641
- Sari R., Piran T., Narayan R., 1998, *Astrophys. J. Lett.*, 497, L17
- Sarin N., et al., 2023
- Savchenko V., et al., 2017, *Astrophys. J. Lett.*, 848, L15
- Schady P., 2017, *Roy. Soc. Open Sci.*, 4, 170304
- Schulze S., et al., 2011, *Astron. Astrophys.*, 526, A23
- Sironi L., Giannios D., 2013, *Astrophys. J.*, 778, 107
- Sironi L., Spitkovsky A., 2009, *The Astrophysical Journal*, 698, 1523
- Sironi L., Spitkovsky A., 2011, *The Astrophysical Journal*, 726, 75
- Sironi L., Spitkovsky A., Arons J., 2013, *Astrophys. J.*, 771, 54
- Sironi L., Keshet U., Lemoine M., 2015a, *Space Sci. Rev.*, 191, 519
- Sironi L., Petropoulou M., Giannios D., 2015b, *Mon. Not. Roy. Astron. Soc.*, 450, 183
- Smartt S. J., et al., 2017, *Nature*, 551, 75

- Soares-Santos M., et al., 2017, *Astrophys. J.*, 848, L16
- Spitkovsky A., 2008, *Astrophys. J. Lett.*, 682, L5
- Spruit H. C., Daigne F., Drenkhahn G., 2001, *Astron. Astrophys.*, 369, 694
- Suresh A., Huynh H., 1997, *Journal of Computational Physics*, 136, 83
- Tanvir N. R., et al., 2017, *Astrophys. J.*, 848, L27
- Thompson C., 1994, *Mon. Not. Roy. Astron. Soc.*, 270, 480
- Tomita S., Ohira Y., 2016, *Astrophys. J.*, 825, 103
- Troja E., et al., 2017, *Nature*, 551, 71
- Troja E., et al., 2018, *Nature Commun.*, 9, 4089
- Troja E., et al., 2020, *Mon. Not. Roy. Astron. Soc.*, 498, 5643
- Troja E., et al., 2022, *Mon. Not. Roy. Astron. Soc.*, 510, 1902
- Uhm Z., Beloborodov A. M., 2006, *AIP Conf. Proc.*, 836, 189
- Uhm Z. L., Zhang B., Hascoët R., Daigne F., Mochkovitch R., Park I. H., 2012, *The Astrophysical Journal*, 761, 147
- Vanthieghem A., Lemoine M., Plotnikov I., Grassi A., Grech M., Gremillet L., Pelletier G., 2020, *Galaxies*, 8, 33
- Vernetto S., Lipari P., 2016, *Phys. Rev. D*, 94, 063009
- Virtanen P., et al., 2020, *Nature Methods*, 17, 261
- Vurm I., Beloborodov A. M., 2017, *Astrophys. J.*, 846, 152
- Vurm I., Metzger B. D., 2021, *Astrophys. J.*, 917, 77
- Wang X.-Y., Mészáros P., 2006, *Astrophys. J. Lett.*, 643, L95
- Wang X.-Y., Dai Z. G., Lu T., 2001, *Astrophys. J.*, 556, 1010
- Wang X.-Y., Li Z., Meszaros P., 2006, *Astrophys. J. Lett.*, 641, L89
- Wang X.-Y., Liu R.-Y., Zhang H.-M., Xi S.-Q., Zhang B., 2019, *The Astrophysical Journal*, 884
- Wang H., Dastidar R. G., Giannios D., Duffell P. C., 2024
- Warren D. C., Ellison D. C., Bykov A. M., Lee S.-H., 2015, *Mon. Not. Roy. Astron. Soc.*, 452, 431
- Warren D. C., Barkov M. V., Ito H., Nagataki S., Laskar T., 2018, *Mon. Not. Roy. Astron. Soc.*, 480, 4060
- Warren D. C., Dainotti M., Barkov M. V., Ahlgren B., Ito H., Nagataki S., 2022, *Astrophys. J.*, 924, 40
- Wijers R., Galama T., 1999, *Astrophys. J.*, 523, 177
- Woosley S. E., 1993, *The Astrophysical Journal*, 405, 273
- Xie X., Zrake J., MacFadyen A., 2018, *Astrophys. J.*, 863, 58
- Yamasaki S., Piran T., 2022, *Mon. Not. Roy. Astron. Soc.*, 512, 2142
- Yi S.-X., Xi S.-Q., Yu H., Wang F. Y., Mu H.-J., Lü L.-Z., Liang E.-W., 2016, *Astrophys. J. Suppl.*, 224, 20
- Yi S.-X., Yu H., Wang F. Y., Dai Z. G., 2017, *Astrophys. J.*, 844, 79
- Zaninoni E., Bernardini M. G., Margutti R., Oates S., Chincarini G., 2013, *Astron. Astrophys.*, 557, A12
- Zhang B., 2018, *The Physics of Gamma-Ray Bursts*, doi:10.1017/9781139226530.
- Zhang B., Kobayashi S., 2005, *Astrophys. J.*, 628, 315
- Zhang B., Yan H., 2011, *The Astrophysical Journal*, 726, 90
- Zhang H., Christie I., Petropoulou M., Rueda-Becerril J. M., Giannios D., 2020, *Mon. Not. Roy. Astron. Soc.*, 496, 974
- Zhang Z.-L., Liu R.-Y., Geng J.-J., Wu X.-F., Wang X.-Y., 2022, *Mon. Not. Roy. Astron. Soc.*, 513, 4887
- Zhang B. T., Murase K., Ioka K., Zhang B., 2023
- Zirakashvili V. N., Aharonian F., 2007, *Astron. Astrophys.*, 465, 695
- van Eerten H., Leventis K., Meliani Z., Wijers R., Keppens R., 2010, *Mon. Not. Roy. Astron. Soc.*, 403, 300